

Structure-Property Relations in Nanostructured Materials: From Solar Cells to Gecko Adhesion



Zhuxia Rong

Supervisor: Prof. Ullrich Steiner
Jesus College
Department of Physics
University of Cambridge

This dissertation is submitted for the degree of Doctor of Philosophy
October 2013

Declaration

This dissertation is the result of my own work and includes nothing which is the outcome of work done in collaboration except where specifically indicated in the text. I declare that no part of this work has been submitted for a degree or other qualification at this or any other university. This thesis does not exceed the word limit of 60,000 words set by the Physics and Chemistry Degree Committee.

Zhuxia Rong

October 2013

Acknowledgements

First of all, I would really like to thank my PhD supervisor Prof. Ullrich Steiner for not only offering me the opportunity to study in his group, but also for giving me all the guidance and support over four years. He offered me with freedom in pursuit of various research projects and collaboration opportunities. I would not be able to finish my PhD without his encouragement especially during the most difficult times when all directions seemed lost.

The advice and assistance I have received from almost everybody from the Thin Film and Interfaces group have been crucial to my study and I am very grateful to have the opportunity to work with them: Sven Hüttner and Peter Kohn for their constant support and guidance through the polymer blends project, either in teaching me new experimental techniques or advising me through enlightening discussions; Alessandro Sepe and Kai Scherer for the productive collaboration; Pola Goldberg-Oppenheimer for her efforts on the gecko project; Stefan Guldin for the open discussions about things apart from research. Li Li for her accompany and mental support through my PhD. I am particularly grateful to Harry Beeson and Jonathan Lim for their effort spent on improving my English. Many thanks also go to the rest of the group, Alex Finnermore, Ellie Kim, Gen Kamita, Katherine Thomas, Maik Scherer, Mathias Kolle, Nataliya Yufa, Pedro Cunha, Silvia Vignolini, Stefano Salvatore, Sandeep Pathak and Xiaoyuan Sheng.

I would also like to acknowledge the people from the Optoelectronics group. Cheng Li and Jianpu Wang for the synthesis of ZnO nanocrystal and the help with device fabrication. Paul Hopkinson for his very generous help with the polymer thermal analysis. Richard Gymer for always available on numerous occasions and willing to help.

Special thanks to all the collaborators: Dr. Walter Federle and Yanmin Zhou from the De-

partment of Zoology for the insightful discussions and help with adhesion measurements, Dr. Stephan Hofmann from the Department of Engineering for his thoughtful feedback and invaluable advices on the gecko project.

I am also thankful to Cambridge Overseas Trust and China Scholarship Council for funding support.

Finally, I am deeply grateful to my parents for their support and patience and my husband Feng Tian for always being there when needed through the years.

Abstract

This thesis explores the structure-property relations in different nanostructured materials. Nanostructured polymer blends with interpenetrating network morphology of donor and acceptor materials have been considered ideal for organic bulk heterojunction photovoltaics. In this work we mainly investigate the self-organization of polymer blends via crystallization to generate functional nanostructures for organic electronics.

Controlling morphology of organic photovoltaic thin films is crucial for the optimization of the device performance as there is a fine balance of exciton generation and separation as well as charge transport. To better understand the bulk heterojunction morphology, we first investigated the structure formation of poly (3-hexylthiophene) (P3HT)/ phenyl-C61-butyric-acid methyl ester (PCBM) system. Crystallization-induced phase separation has been found to drive the formation of a nanostructure in the blends, the size of which is determined by the intrinsic 10 nm length scale of semicrystalline P3HT. The mixing of PCBM within amorphous P3HT interlayers does not disrupt the crystallinity of the P3HT. P3HT crystallization expels PCBM into the spherulitic interlamellar amorphous layers, where it enriches to its miscibility limit. Above the solubility limit, PCBM aggregates start to form. The results suggest that the crystallization of P3HT and the enrichment of PCBM in interlamellar regions give rise to interconnected donor and acceptor phases those are close to the optimal bulk heterojunction structure. This structure formation mechanism is manifested by the good photovoltaic performance of spherulitic P3HT/PCBM films.

Structural studies of P3HT/poly[(9,9-dioctylfluorene)-2,7-diyl-alt-(4,7-bis(3-hexylthien-5-yl)-2,1,3-benzothiadiazole)-2', 2''-diyl] (F8TBT) are presented. P3HT/F8TBT system exhibits a crystallization-driven structure formation similar to the P3HT/PCBM system despite

the existence of a miscibility gap. The lamellar crystallization of P3HT is not perturbed by the addition of F8TBT. X-ray scattering studies indicate that F8TBT is mixed in the inter-lamellar amorphous phase up to a solubility limit, while a bulk heterojunction framework is established by the crystalline lamellae of P3HT. The excess F8TBT is accommodated at amorphous grain boundaries as well as the film/substrate interface. The structural studies are correlated with the photovoltaic device performance of P3HT/F8TBT films which exhibit spherulitic morphology. Devices based on spherulitic films show moderate efficiencies with improved fill factors but decreased photocurrents in comparison to that of thermal annealing condition. The results suggest that the nanostructure formation in P3HT/F8TBT blends is determined by the crystallization of P3HT, resulting in a structural size that are beneficial for exciton dissociation, while the F8TBT segregation at the substrate interface impair the device performance.

The phase separation behavior in crystalline/crystalline blends consisting of P3HT and polyethylene oxide (PEO) is investigated. The self-assembly of P3HT in solution induces vertical segregation in blend films, in comparison to typical lateral polymer phase separation structures from non-aggregated solutions. Thin film transistors based on P3HT/PEO blends show show a nearly undegraded charge carrier mobility at low P3HT content due to the formation of a layered structure with P3HT nanowire networks segregated at the dielectric surface.

Finally, a diversion from morphology studies of polymer blends involves the biomimetic fabrication of hierarchical fibrillar structures to achieve gecko adhesion. The hierarchical structures were fabricated based on polymer pillars tipping with carbon nanotube forests. The adhesion performance of the polymer-carbon nanotube hierarchical structures was tested by shear force measurements.

Contents

1	Introduction	1
2	Background and Theory	3
2.1	Overview	3
2.2	Conjugated Polymers	4
2.2.1	Electronic Structure of Conjugated Polymers	4
2.2.2	Optical Transitions of Photoexcitations	6
2.2.3	Transport Mechanisms	8
2.3	Organic Photovoltaic Devices	8
2.3.1	The Bulk Heterojunction (BHJ)	8
2.3.2	Characterization of Organic Photovoltaic Devices	10
2.3.3	Morphology	12
2.4	Thermodynamics of Polymer Blends	16
2.4.1	Flory-Huggins Theory	16
2.4.2	Phase Diagrams	18
2.5	Surface Enrichment in Polymer Blends	20
2.6	Semicrystalline Polymers	23
2.6.1	The Crystal Lamellae	23
2.6.2	Supramolecular Structure	25
2.6.3	Semicrystalline Structure of Poly(3-hexylthiophene) (P3HT)	26
3	Materials and Experimental Techniques	29
3.1	Materials	29

Contents

3.2	Sample Preparation	30
3.2.1	Thin Film Deposition	30
3.2.2	Solvent Vapor Annealing	30
3.2.3	Device Fabrication	31
3.3	Characterization Techniques	32
3.3.1	Solar Cells Characterization	32
3.3.2	Optical Microscopy	33
3.3.3	Atomic Force Microscopy	33
3.3.4	Scanning Electron Microscopy	33
3.3.5	Transmission Electron Microscopy	34
3.3.6	Ultraviolet-Visible Absorption Spectroscopy	34
3.3.7	Photoluminescence Spectroscopy	35
3.3.8	X-ray Scattering	35
4	Crystallization-Induced 10 nm Structure Formation in P3HT/PCBM Blends	39
4.1	Introduction	39
4.2	Experimental Methods	41
4.3	Results and Discussion	42
4.3.1	Miscibility of P3HT/PCBM	42
4.3.2	UV-Vis Measurements of P3HT/PCBM	45
4.3.3	SAXS and WAXS of Bulk P3HT/PCBM	46
4.3.4	GISAXS and GIWAXS of P3HT/PCBM Thin Films	50
4.4	Conclusion	53
5	Spherulitic Crystallization of P3HT/PCBM and Its Effect on Device Performance	55
5.1	Introduction	55
5.2	Experimental Methods	57
5.3	Results and Discussion	57
5.3.1	Spherulitic Crystallization of P3HT/PCBM	57
5.3.2	Morphology Characterization of P3HT/PCBM	60
5.3.3	Device Characterization of Standard P3HT/PCBM Solar Cells	62

Contents

5.3.4	Device Characterization of Inverted P3HT/PCBM Solar Cells	64
5.4	Conclusion	66
6	Structure Formation in P3HT/F8TBT Blends	67
6.1	Introduction	67
6.2	Experimental Methods	69
6.3	Results and Discussion	70
6.3.1	Surface Morphology of P3HT/F8TBT	70
6.3.2	Melt Recrystallization of P3HT/F8TBT	72
6.3.3	Structural Study on P3HT/F8TBT Thin Films using X-ray Scattering	74
6.3.4	Spherulitic Crystallization of P3HT/F8TBT	79
6.3.5	Effects of Mesoscale Structure on Device Performance	81
6.4	Conclusion	84
7	Polymer Field-Effect Transistors Based on P3HT/PEO Blends	85
7.1	Introduction	85
7.2	Experimental Methods	87
7.2.1	Thin Film Preparation	87
7.2.2	Transistor Fabrication	87
7.2.3	Measuring Device Characteristics	88
7.3	Results and Discussion	90
7.3.1	Self-assembly of P3HT in Solution	90
7.3.2	Morphology of P3HT/PEO Blends	91
7.3.3	Field-Effect Transistor Performance	94
7.4	Conclusion	96
8	Biomimetic Hierarchical Structures to Mimic Gecko Adhesion	97
8.1	Introduction	97
8.1.1	Structural Features of a Gecko Foot	98
8.1.2	Properties of Gecko Adhesion	99
8.1.3	Physical Principles for Adhesion of Fibrillar Structures	101
8.1.4	Bioinspired Adhesive Structures	102

Contents

8.2	Experimental Methods	105
8.3	Fabrication of Hierarchical CNTs-based Pillar Arrays	109
8.4	Adhesion Characterization	110
8.4.1	Force Measurements on Smooth Surfaces	110
8.4.2	Force Measurements on Rough Surfaces	115
8.4.3	Oscillatory Shear Measurements	116
8.5	Conclusion	118
9	Summary	121
	List of Abbreviations	127
	Bibliography	129

Chapter 1 Introduction

The increasing demand for renewable energy sources has stimulated research interest in efficient and low cost solar energy conversion. Although conventional inorganic semiconductor solar cells are now the dominating photovoltaic technology, there has been a tremendous effort to replace this high-cost system. Since the discovery of conductive polymers, they became an alternative to traditional inorganic semiconductors in many electronic applications such as organic light emitting diodes, organic field effect transistors and organic photovoltaics (OPVs). The solution processability of polymer semiconductors provides a low cost and scalable route to replace the inorganic photovoltaics.

Even though OPVs are still limited by the lower efficiency and stability, rapid progress has been made in these aspects through both the synthesis of new polymers and the optimization of fabrication conditions. The physical properties of polymeric semiconductors can be chemically tuned to lower energy gaps in order to enhance their photo-absorption within the solar spectrum and thus to harvest more sunlight.

The OPV device efficiency is largely influenced by the film morphology, molecular order, and interfacial properties of all device components. The morphology in the active layer plays a crucial role in the device properties. For many polymer blend systems, especially those with poly(3-hexylthiophene) (P3HT), empirical optimization procedures, either during the film deposition or using post-fabrication annealing, significantly improve the device performance. While device performance benefits from such treatments, basic thermodynamic studies aiming towards solubility or demixing effects might be difficult as small variations in how the samples are prepared might strongly influence the observations. Therefore, in this study, we investigate the structure formation in blend systems under conditions

close to thermodynamic equilibrium.

The aim of this thesis is to investigate the structure development in semiconducting polymer blends and its correlation with the device performance. Chapter 2 presents the necessary background knowledge including an overview of semiconducting behavior in conjugated polymers, thermodynamics of polymer blends, and crystallization of polymers. A literature review of recent studies on bulk heterojunction morphology is also included. The experimental methods used in this thesis are described in Chapter 3.

Chapter 4 focuses on the blend system of P3HT and phenyl-C61-butyric-acid methyl ester (PCBM). This system is one of the most established polymer/fullerene blends, however, exact details on the structure formation and direct observation of crystallization were lacking. In this chapter we systematically investigate the structure evolution in P3HT/PCBM with varying PCBM contents. We confirm the crystallization-induced structure formation in P3HT/PCBM, and investigate the photovoltaic performance of devices based on spherulitic films in Chapter 5.

Chapter 6 presents the structural studies on a P3HT/polyfluorene (P3HT/F8TBT) blend system. This system exhibits different possible structure formation paths involving binodal or spinodal decomposition competing with crystallization. A detailed description of the crystallization of P3HT in the blends and its role in the morphology development is discussed. Device applications of spherulitic P3HT/F8TBT films are also presented.

In Chapter 7, the vertical segregation by self-assembly in the blends of P3HT and insulating polyethylene oxide (PEO) is investigated. Thin films of P3HT/PEO blends are used to make field-effect transistors (FET), and the effect of film morphology on electrical performance is discussed.

The thesis includes a separate project in Chapter 8 on the bioinspired fabrication of hierarchical structures based on polymer micro-pillars and carbon nanotubes. The performance of the hierarchical structures with different feature sizes was tested by force measurements. Finally, Chapter 9 briefly reviews the conclusions from the work and relates to the prospects for future work.

Chapter 2 Background and Theory

2.1 Overview

Organic photovoltaics based on thin polymer films have attracted widespread interest due to their mechanical flexibility, solution processability and potential low cost fabrication over the conventional inorganic photovoltaic technologies.¹ During the past years, organic solar cells have achieved great success with power conversion efficiencies approaching 10%.^{2,3}

The photocurrent generation mechanism in organic photovoltaic devices is fundamentally different from that in inorganic solar cells. In inorganic p-n junction solar cells, free electron-hole pairs are generated spontaneously upon light absorption. Photocurrent generation is facilitated by the high charge carrier mobilities in doped semiconductors.⁴ In organic photovoltaic devices, however, light absorption leads to the formation of excitons.⁵ A heterojunction of two different organic semiconductors with offset energy levels, the donor and the acceptor, is used to separate these coulombically bound excitons.^{6,7} The bulk heterojunction concept is introduced to create a large heterojunction interface through interpenetrating networks of separated donor and acceptor phases so as to improve the efficiency of exciton dissociation. The photocurrent generation is strongly affected by the bulk heterojunction morphology. It is therefore of great importance to understand the fundamental process by which a bulk heterojunction interface forms from the molecularly mixed donor/acceptor blend and how the morphology correlates with device performance.

2.2 Conjugated Polymers

The conductive properties of conjugated polymers were first discovered in 1977 in iodine-doped polyacetylene, which led to the Nobel Prize win for Shirakawa, Heeger and MacDiarmid in 2000. In the 1990s, the discovery of electroluminescence of phenyl-based polymers was another breakthrough for conjugated polymers and started its widespread application in electronic devices.^{8,9} This triggered intense research on the development of conjugated polymers such as polythiophene, poly(phenylene vinylene), polyfluorene and their copolymers, in order to meet the critical requirements for optoelectronic device application, for example, solution processability, light-harvesting ability, and high electron mobility.¹⁰⁻¹²

2.2.1 Electronic Structure of Conjugated Polymers

Conjugated polymers have the structure of alternating single and double bonds in the chain backbone, which is different to most commodity polymers such as polyethylene (PE) and polypropylene (PP) that have backbone carbons connected by single bonds. Carbon has the electronic configuration of $1s^2 2s^2 2p^2$ that enables carbon atoms to form four covalent bonds. In polymers like PE, the valence electrons in carbon atoms hybridize to form four sp^3 orbitals, which are σ -bonds. Conjugated polymers, however, have adjacent unsaturated carbon atoms that are sp^2 hybridized. Each of these carbon atoms forms three σ bonds and a remaining p_z atomic orbital which overlaps with that of a neighboring carbon atom to produce a π bond. Figure 2.1 presents a schematic of π binding in benzene, the same type of bonding as in conjugated polymers. The connected p_z orbitals with delocalized electrons along the polymer chain lower the overall energy of the molecules and have increased stability.

The resonance interaction between the π bonds results in delocalized π electron states. Hückel molecular orbital theory is applied to understand the band structures for an isolated conjugated molecule. This approach neglects the σ bonds, and approximates the molecular orbitals as linear combinations of the p_z orbitals of the constituent atoms. The illustration of molecular orbitals in the Hückel theory approximation with increasing monomer units is shown in Figure 2.2. The overlap of two atomic orbitals results in the formation of two molecular orbitals, one of which has lower energy than the original orbital (bonding) and the other is higher in energy (antibonding).

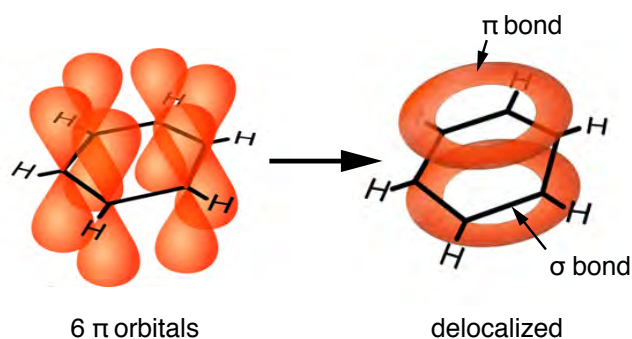


Figure 2.1 Schematic illustration of the benzene orbitals. The p_z orbitals are perpendicular to the plane of sp^2 orbitals, which overlap to form π bonds. The σ bonds are marked by black lines. Adapted from "Organic Chemistry".¹³

Hückel theory predicts a continuous distribution of electronic states in an infinitely long conjugation system. However, the conjugated chains have geometric restrictions that reduce the extent to which electronic states can be delocalized along the backbone. The energy levels are localized to the highest occupied molecular orbital (HOMO) and the lowest unoccupied molecular orbital (LUMO) levels. The term, conjugation length, describes the typical length scale over which p_z orbitals overlap. The distribution of conjugation lengths of a polymer gives rise to energetic disorder, and with increasing conjugation length, there is an increase in the distribution of π and π^* states and a decrease in the HOMO-LUMO gap.^{14,15}

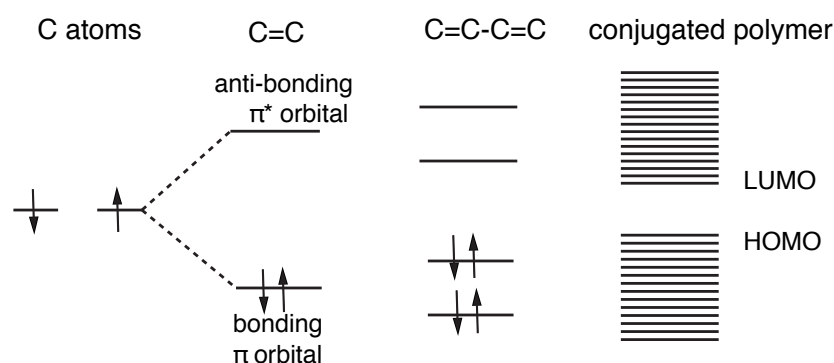


Figure 2.2 Molecular orbitals with increasing carbon atoms in the Hückel theory approximation.

The HOMO and LUMO states are, respectively, the analogues of valance band (VB) and conduction band (CB), which are usually presented in solid-state physics in a band theory of weak bonds. For semiconductors, the VB is full and separated from CB by an energy gap, thus energy is required to elevate the electrons from the VB to CB. The energy gap for con-

jugated polymers is in the range of 1.5 eV to 3 eV. The electronic conduction in conjugated polymers is different from inorganic semiconductors due to the fact that the intermolecular interactions between the covalently bonded polymer chains are rather weak, whereas inorganic semiconductors form covalent interatomic bonding through out the material.

Since most conjugated polymers do not have intrinsic charge carriers, the required charge carriers are provided through a doping process. Conjugated polymers can be made semi-conducting or conducting through doping. There are several types of doping that have been used: 1) chemical doping such as the treatment of polyacetylene with iodine yielding a high conductivity of about 10^{-2} S/cm; 2) electrochemical doping by oxidizing or reducing the material under an applied voltage; 3) optical doping associated with photogeneration of electron-hole pairs under light excitation; 4) charge-injection doping through an electrode as in field-effect transistors; 5) electrical doping by charge transfer from a donor to an acceptor-type material.¹⁶

2.2.2 Optical Transitions of Photoexcitations

Photo absorption promotes an excited electron to the LUMO and leaves a hole in the HOMO. The resulting positively charged molecule exerts an attractive Coulomb force so that the excitation energy falls below the band gap. The electron-hole pair is termed as exciton. Excitons are confined to a nanometer volume due to the localized nature of the electronic states and the low dielectric permittivity of organic materials. A singlet exciton is characterized by an anti-parallel orientation of the angular momentum of the electron and hole spins, whereas the parallel orientation of the angular momentum of spin is indicative of a triplet exciton. Hund's rule states that the triplet excited state has a lower energy than the corresponding singlet state.

Figure 2.3 shows a simplified scheme of the transitions that can occur in an organic molecule. Each energy level represents a different electron configuration in the molecular orbitals. Absorption of a photon promotes an electron from the ground state S_0 into any of the higher vibrational levels via an allowed electronic transition. Absorption typically occurs on a time scale of 10^{-15} s. Depending on the photon energy, the transition can end in the first excited singlet state S_1 or in higher excited states S_n . The absorption spectrum of

a conjugated molecule is a superposition of transitions from the ground state to each of the vibrational levels of the higher excited states.

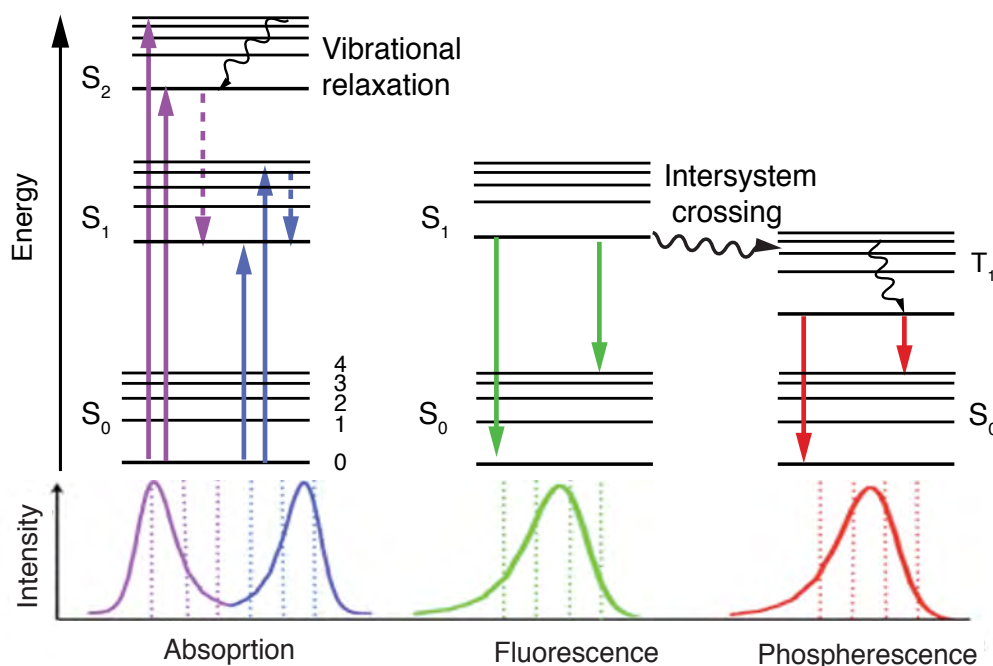


Figure 2.3 Schematic illustration of different transitions that may take place after photogeneration in a conjugated polymer. Absorption (purple and blue arrows) of photons promotes electrons from the ground state, S_0 , to various vibrational sub-levels associated with singlet electronic states, i.e., S_1 , S_2 . Radiation occurs as fluorescence (green arrows) and phosphorescence (red arrows). Singlet excitons convert to triplet states via intersystem crossing.¹⁷

Excitons at higher vibrational sub-levels undergo energetic relaxation to the vibrational ground state of S_n , while higher excitations in $S > 1$ levels generally relax to the S_1 level through internal conversion. The energy relaxation occurs on a time scale of 10^{-12} to 10^{-10} s. Photon emission is a consequence of the energy release from the ground level of S_1 to S_0 , known as fluorescence. Fluorescence exhibits a typical vibronic feature arising from transitions into the vibrational sub-levels of S_0 . The lifetime of fluorescence is typically of 10^{-10} to 10^{-7} s. Alternatively, intersystem crossing can happen by spin-conversion from singlet excitons to triplet excitons. Triplet excitons mostly decay to the ground state by emission of photons as phosphorescence. The triplet exciton typically has a much longer lifetime on a time scale of 10^{-6} to 1 s because the transition to the ground state is spin-forbidden by the spin selection rule.¹⁷

2.2.3 Transport Mechanisms

For a molecular excitation, the exciton is localized on a single chain, with an electron in the LUMO and a hole in the HOMO, both residing on the same chain. The photogenerated exciton propagates through dipole-dipole interactions, in which a simultaneous decay-excitation process takes place between two neighboring monomers. This mechanism is referred to as Förster transfer.¹⁸ The rates of the transfer depend on the overlap of the associated wave functions. Charge transport in polymer semiconductors is described as a diffusive hopping process. Many models attempt to provide an understanding of the charge transport mechanism.¹⁹ Irrespective of the model adopted, charge transport in conjugated polymers is determined by the degree of π orbital overlap. This can facilitate the intra-chain transport where excitons are delocalized along the polymer backbone. Also the interchain transport can be improved if polymers crystallize into a layered packing.

2.3 Organic Photovoltaic Devices

2.3.1 The Bulk Heterojunction (BHJ)

The first organic photovoltaic cell was developed by Kallmann and Pope in 1959.²⁰ The structure was based on a single layer of the conjugated molecule anthracene inserted between two metal electrodes with different work functions, which generates an electric field in the active layer. The photocurrent generation was very poor because the excitons are strongly bound and the electric field generated by the difference in work functions was too weak to dissociate the excitons into free charges. The heterojunction structure was later introduced by Tang in 1986, creating an interface between donor (D) and acceptor (A) materials in a bilayer structure.⁶ The major difference between a single layer and a heterojunction structure is that electrons and holes are separated and transported in donor and acceptor materials, respectively, in the heterojunction structure. Charge recombination is significantly reduced and mainly dependent on the trap densities. In this bilayer geometry, however, most excitons generated in the bulk decay to the ground state before they can reach the interface since the exciton diffusion length is less than 10 nm in most conjugated polymers. Only excitons generated within the proximity of a donor-acceptor interface can contribute

to the photocurrent. In order to harvest more excitons, a bulk heterojunction (BHJ) structure was adopted in which donor and acceptor are intimately mixed on the nanometer scale to form interpenetrating networks.^{21,22} Figure 2.4b shows a typical type II heterojunction in which the HOMO and LUMO energy levels of the donor are higher than those of the acceptor material. The energetic offset between the donor and acceptor provides the driving force for exciton dissociation at the interface. The charge pairs are separated by the internal electric field under short-circuit condition.²³

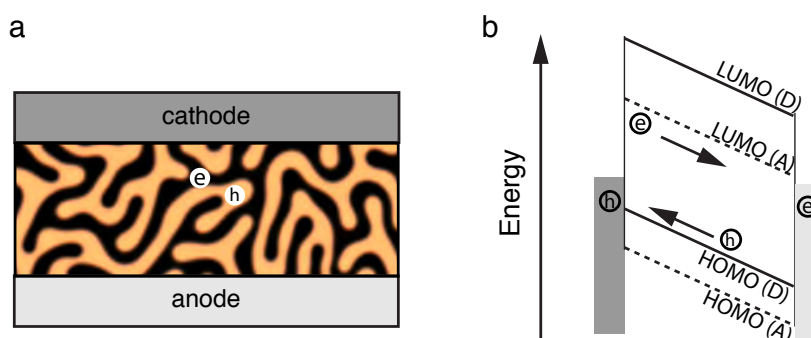


Figure 2.4 a) Schematic illustration of a BHJ morphology showing interpenetrating donor and acceptor networks. b) Type II interface in a heterojunction photovoltaic device.

The working principles of organic photovoltaics are illustrated in Figure 2.5. The photocurrent generation process consists of the following consecutive steps: 1) exciton generation and diffusion to the D-A interface; 2) charge transfer state at the interface; 3) exciton dissociation and charge transport; and 4) charge collection.

First, light absorption, either by the donor or the acceptor, creates excitons, bound electron-hole pairs. The exciton of a conjugated polymer is spatially localized and has a strong binding energy as a result of coulombic interaction between the oppositely charged carriers. The exciton is required to diffuse to a donor/acceptor interface so that exciton dissociation can occur. Exciton diffusion, described by Förster transfer, can be either intramolecular or intermolecular and generally lowers the energy of the exciton. Dissociation of excitons must occur before they decay to the ground state, therefore, the diffusion length is a critical parameter limiting the extent of charge separation in a BHJ.

If the excitons reach the donor-acceptor interface within the diffusion length, the electron transfer step generates an interfacial charge transfer (CT) state. This state, energetically favored for charge transfer from the donor to the acceptor phase, is driven by the offset

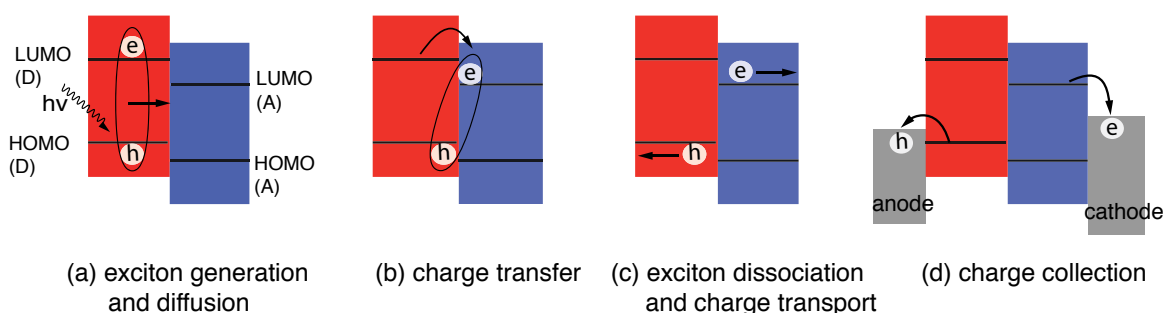


Figure 2.5 Schematic illustrations of working mechanisms of BHJ organic photovoltaics: a) light absorption leads to exciton generation followed by the exciton diffusion towards a donor/acceptor interface; b) charge transfer at the interface; c) exciton dissociation and free charge carriers transporting; d) charge extraction into the electrodes.

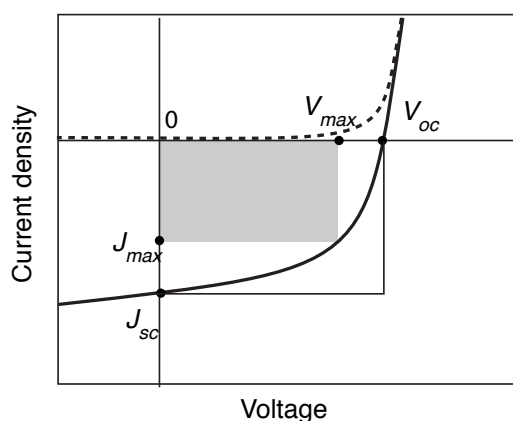
of the LUMO levels. The CT state can undergo geminate recombination or dissociate into separated charge carriers. Whether the charge separation happens depends mainly on the thermal energy of the transferred electron and the electric field which can reduce the Coulomb potential barrier. The separated charges then have to be transported in the respective phases to the electrodes for charge collection. The charge carrier mobility of donor or acceptor can be enhanced by macroscopic order and crystallinity. Also, the enrichment of the donor at the anode and the acceptor at the cathode can facilitate the charge collection.²³

2.3.2 Characterization of Organic Photovoltaic Devices

The performance of a solar cell is characterized by current-voltage (J - V) measurements under dark and illumination conditions. Figure 2.6 shows the typical current density-voltage curve for a solar cell. Without illumination, a solar cell behaves as a diode with negligible current flow until a large charge injection starts at a forward bias above a certain threshold. Under illumination, the solar cell generates current and the J - V curve is shifted in accordance to the amount of photocurrent.

The short circuit current, J_{sc} , refers to the current density that passes through the device without external applied voltage. The photocurrent in short circuit condition is a reverse current as the holes and electrons will go towards the anode and cathode respectively due to a built-in potential. When a voltage is applied in the reverse bias, where the anode is connected to the negative and the cathode to positive voltage, the electric field in the BHJ increases so that all photogenerated holes and electrons are extracted. On the other hand,

a forward bias compensates the reverse photocurrent until the open circuit voltage, V_{oc} , is achieved. Beyond V_{oc} , no current can be detected. The fill factor (FF) is calculated as the ratio of maximum obtainable power to the product of J_{sc} and V_{oc} . Therefore, the more square the J - V curve becomes the higher the FF . The power conversion efficiency (PCE) is derived as the ratio between the maximum power and the incident light power ($P_{incident}$).



fill factor (FF)

$$FF = \frac{V_{max} \cdot J_{max}}{V_{oc} \cdot J_{sc}}$$

power conversion efficiency (PCE):

$$\eta = \frac{P_{max}}{P_{incident}} = \frac{V_{oc} \cdot J_{sc} \cdot FF}{P_{incident}}$$

Figure 2.6 Typical J - V characteristics of an organic BHJ solar cell measured in dark (dotted line) and illumination (solid line) conditions. The short-circuit current (J_{sc}), open-circuit voltage (V_{oc}), fill factor (FF), and power conversion efficiency (PCE) are determined from the J - V curve, respectively.

The performance of an organic photovoltaic device is determined by the efficiencies of each step in the photocurrent generation process. Studies in the literature have shown that V_{oc} is limited by the energy difference between the donor HOMO and acceptor LUMO level, but the practically obtainable V_{oc} is often reduced by up to ~ 0.3 V due to the energy loss at electrode interface and recombination of charge carriers.²⁴ J_{sc} is determined by light absorption in the photoactive film and the ability to extract charges under its built-in electric field. It is therefore limited by the internal quantum efficiency of charge generation, transport and extraction.²⁵ A high fill factor requires high and balanced charge mobilities as well as low recombination rates. Unbalanced hole and electron mobilities will cause charge carriers with low mobility accumulate in the device which results in an additional electric field and blocks the extraction of the carriers. Therefore, improvement of these device parameters, J_{sc} , V_{oc} , and FF require not only optimization of the morphology of the active layer but also the interface properties and electrode materials.

2.3.3 Morphology

There has been extensive research on the selection of good donor and acceptor pairs in order to achieve a high efficiency of organic solar cells. In addition to the most commonly used poly-(hexylthiophene) (P3HT) and phenyl-C61-butyric acid methyl ester (PCBM), high performance conjugated polymers have been developed with designed bandgap and energy levels and enhanced molecular planarity to attain high carrier mobility.^{10,26,27} Figure 2.7 presents the chemical structures of those new donor and acceptor materials. Fullerene derivatives as the acceptor material have the advantage of strong electron selectivity and high electron mobility. In polymer/fullerene systems, the device efficiencies have been significantly improved from $\sim 5\%$ with P3HT^{28,29} to $\sim 7\%$ with PCDTBT,^{30,31} and to $\sim 9\%$ with PTB7.³²

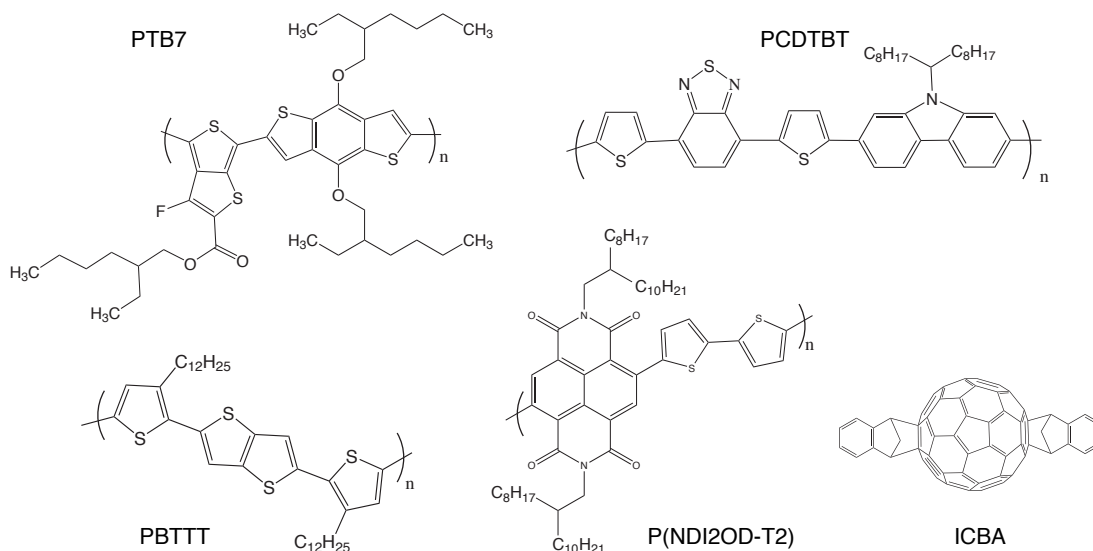


Figure 2.7 Chemical structures of electron donor and acceptor materials. PTB7 : poly[[4,8-bis[(2-ethylhexyl)oxy] benzo[1,2-b:4,5-b']dithiophene-2,6-diyl][3-fluoro-2-[(2-ethylhexyl)carbonyl]thieno[3,4-b]thiophenediyl]]; PCDTBT : poly [[9-(1-octylonyl)-9H-carbazole-2,7-diyl]-2,5-thiophenediyl-2,1,3-benzothiadiazole-4,7-diyl-2,5-thiophenediyl]; PBTBT : poly(2,5-bis(3-hexadecylthiophen-2-yl)thieno[3,2-b] thiophene); P(NDI2OD-T2) : poly [N,N'-bis(2-octyldodecyl)-naphthalene-1,4,5,8-bis(dicarboximide) -2,6-diyl]-alt-5,5'-(2,2'-bithiophene); ICBA :1',1'',4',4''-tetrahydro-di[1,4]methanonaphthaleno [5,6]fullerene-C60.

Morphology optimization is usually required to maximize the efficiency when a new donor/acceptor pair is used in organic solar cells because the photogeneration process is dependent on the nanostructure. The device must have an interpenetrating network with a large interfacial area. To reduce the geminate recombination, the electron and hole must

have separate transport pathways to their respective electrodes. Furthermore, the charge transport in conjugated polymers is strongly affected by the molecular order, and thus high crystallinity is desirable to achieve high charge carrier mobility. The degree of phase separation between donor and acceptor determines the size and interconnectivity of each phase and molecular order, which in turn influence the efficiency of charge generation, separation and transport.

The photoactive film is usually deposited from solution of the donor and acceptor blend, mainly by spin-coating or blade-coating. The solution composition (especially the donor/acceptor blend ratio) and film formation process are optimized in order to achieve high efficiencies. The film solidifies within several seconds, therefore, the morphology is affected by both thermodynamics of demixing and kinetics of film formation. The use of solvent mixtures or additives is primarily employed to modify the kinetics of film solidification. Post processing steps such as thermal and solvent annealing are used to further adjust the morphology and once an optimal morphology is achieved it is preserved by quenching to ambient conditions. With the enhancement of crystallization and diffusion of one or both donor and acceptor, the device performance can be effectively improved.

Polymer/Fullerene System

Polymer/fullerene systems have been investigated by different techniques in order to correlate the nanomorphology with device efficiency.³³⁻³⁵ Figure 2.8a shows atomic force microscopy (AFM) images of MDMO-PPV/PCBM blend prepared from chlorobenzene and toluene solvents.^{36,37} The use of chlorobenzene shows better device performance (1.6% efficiency) than toluene (0.7% efficiency) as a result of a smaller scale of phase separation. The difference in film morphology arises from higher solubility of PCBM in chlorobenzene, suppressing the formation of large fullerene agglomerates in the matrix.

The P3HT/PCBM system, where both components can crystallize, shows a different morphological organization compared to MDMO-PPV/PCBM. In the optimized P3HT/PCBM solar cell device, thermal annealing produces nanoscale crystalline P3HT nanowires with a width of 10-20 nm, dispersed in an amorphous phase of P3HT and PCBM (Figure 2.8b).³⁸ Similar results are also obtained by using high boiling point additives with slow evapora-

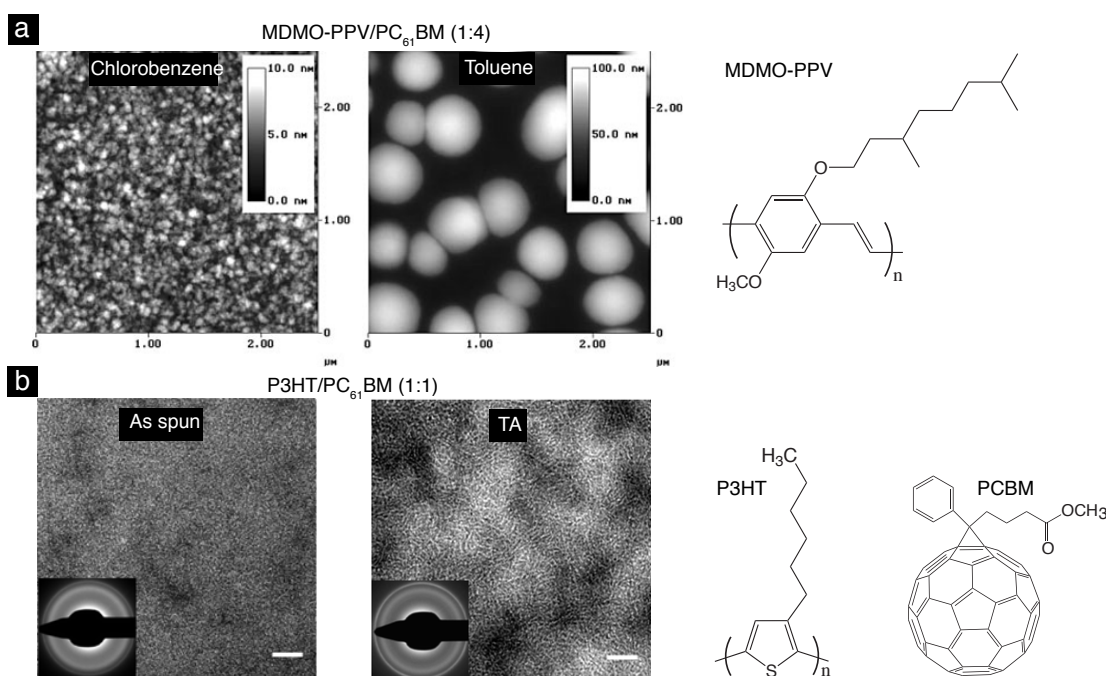


Figure 2.8 a) AFM images of MDMO-PPV/PCBM (1:4) films spin cast from chlorobenzene and toluene solutions. MDMO-PPV : poly[2-methoxy-5-(3,7-dimethyloctyloxy)-1,4-phenylene-vinylene]; PCBM : phenyl-C61-butyric-acid methyl ester. The toluene-cast film shows phase separated domains with a width of a few hundred nanometers.³⁶ b) Bright-field TEM images of 100 nm thick P3HT/PCBM (1:1) films. The as-spun film does not show P3HT crystals and the overall crystallinity of P3HT is low as indicated by electron diffraction (insets). After thermal annealing (TA), P3HT develops a nanowire morphology with increased crystallinity.³⁸

tion rates which have a similar effect as solvent annealing. The crystallization of PCBM is strongly suppressed in the presence of P3HT crystals and only form nano crystallites comprising a few molecules. These morphological changes account for a considerable increase in device efficiency.

The good miscibility between P3HT and PCBM was revealed in the inter-diffusion behavior in a P3HT/PCBM bilayer to form the BHJ structure within several seconds of annealing at 150 °C. PCBM can penetrate into the amorphous P3HT region without perturbing the

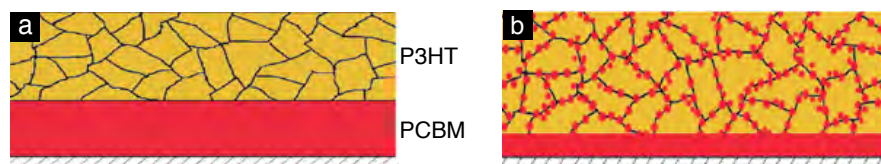


Figure 2.9 Inter-diffusion of the P3HT and PCBM bilayer. a) P3HT crystallizes after a short amount of time of thermal annealing; b) PCBM diffuses into the framework set by P3HT crystals driven by the high solubility of PCBM in amorphous P3HT.³⁹

crystallization of P3HT as illustrated in Figure 2.9. The structure formation is determined by the order of P3HT and the rejection of PCBM from the growth of the P3HT crystal.³⁹ To this end, it became clear that the miscibility of polymer/fullerene is one of the key factors that determine the optimal composition for device operation.

While the P3HT/PCBM blend benefits from post-deposition treatments, polymer/fullerene systems comprising amorphous polymers such as PTB7 and PCDTBT achieve an optimal morphology during film formation without annealing.⁴⁰⁻⁴⁴ The film morphology is largely improved by the optimization of the blend composition and choice of casting solvent. The miscibility between the components is the dominant factor for the overall morphology with the use of solvent affecting the dispersion of excess fullerene. Similar to the morphology mentioned earlier in MDMO-PPV/PCBM, the PTB7/PC₇₀BM (1/1.5) blend exhibits pure fullerene islands embedded in a ~30:70 wt% mixture of PC₇₀BM:PTB7.⁴² The optimized PCDTBT/PC₇₀BM system containing 80 wt% fullerene shows a greater miscibility than the PTB7 system so that more fullerene is required to saturate the polymer phase and still segregate-out to form pure acceptor domain. The ability of fullerene to form aggregation or crystallization in these amorphous matrices has been related to the formation of electron percolation pathways and enhanced charge separation.⁴⁵

Polymer/Polymer Systems

Even though polymer/fullerene blends currently dominate the high efficiency polymer solar cells, polymer/polymer systems offer a greater variation in chemical and electronic structures and thus have potential for high open-circuit voltages and improved absorption compared to poorly absorbing fullerene derivatives. However, the morphology control of polymer/polymer blends is more complex compared to polymer/fullerene blends because of a different demixing behavior. Moreover, polymers are still inferior to fullerene derivatives in electron mobility.

Early combinations of polymer/polymer blends often show large-scale phase separation such as in polyfluorene blends of poly(9,9'-dioctylfluorene-co-bis-N,N'-(4-butylphenyl)-bis-N,N'-phenyl-1,4-phenylene-diamine) (PFB)/poly(9,9'-dioctylfluorene-alt-benzothiadiazole) (F8BT).^{46,47} As the domain size is in the range of hundreds of nanometers, much larger

than the exciton diffusion length, it is more likely that the intermixing within these domains determine the device performance. The use of P3HT as the donor material in all polymer systems is beneficial in terms of the formation of pure donor domains by crystallization. The P3HT/F8TBT blend, one of the most efficient all-polymer solar cell systems, shows a broad domain size distribution with the majority structured around 10 nm. The P3HT/P(NDI2OD-T2) blend, on the other hand, exhibits a hierarchical morphology with small ~ 10 nm domains and larger ~ 100 nm domains. The ~ 10 nm domains were found to evolve during thermal annealing in both the P3HT/F8TBT and P3HT/P(NDI2OD-T2) blends, which is related to the crystallization of P3HT. For both systems, the optimization of device performance under annealing is correlated with phase coarsening and purification on the sub-10 nm length scale which generates a morphology that facilitates exciton dissociation and charge transport.

Morphology studies of different organic photovoltaic systems show nanostructures that deviate from the initial BHJ model of a sharp interface between donor and acceptor phase. The presence of mixing phase has been found in most polymer/fullerene and polymer/polymer blends. As such, it has been proposed that the BHJ morphology should be constructed as a three-phase microstructure comprising of pure donor, pure acceptor and an intimately mixed donor/acceptor phase.

2.4 Thermodynamics of Polymer Blends

2.4.1 Flory-Huggins Theory

The mixing properties of two components is generally described by considering the change in the Gibbs free energy. Complete miscibility of two polymers requires the condition

$$\Delta G_m = \Delta H_m - T\Delta S_m < 0, \quad (2.1)$$

where T is the mixing temperature, ΔH_m is the enthalpy of mixing, and ΔS_m is the entropy of mixing. Due to the increased disorder of a mixed system, an increase in entropy is obtained, $\Delta S_m > 0$. Therefore, the sign of ΔG_m always depends on the value of the enthalpy of mixing ΔH_m .

The thermodynamics of a polymer blend is most generally described by the Flory-Huggins lattice theory. It is a mean field theory which considers the conformational entropy of mixing due to the number of rearrangements during mixing, and the enthalpy of mixing depending on the monomer-monomer pair interactions. The lattice model assumes that the mixture of polymer A and polymer B have the same unit volume and occupy the cells of a regular lattice with coordination number z . Polymer chains are arranged randomly on the periodic lattice and each A or B unit has equal probability to occupy any lattice site.

The entropy of a system is related to the total number of states Ω of the system and is given by $S = k \ln \Omega$, where k is the Boltzmann constant. The entropy of mixing per lattice site can be expressed as

$$\Delta S_m = -k \left(\frac{\phi_A}{N_A} \ln \phi_A + \frac{\phi_B}{N_B} \ln \phi_B \right), \quad (2.2)$$

where $\phi_{A,B}$ is the volume fraction of polymer A or B. $N_{A,B}$ is the number of units. This shows the entropy of mixing is strongly influenced by N , which is proportional to molecular mass of the polymer.

The enthalpy of mixing ΔH_m describes the energy change of pair interactions

$$\Delta H_m = z\phi_A\phi_B \left(\varepsilon_{AB} - \frac{1}{2}(\varepsilon_{AA} + \varepsilon_{BB}) \right), \quad (2.3)$$

where $\varepsilon_{AA}, \varepsilon_{BB}, \varepsilon_{AB}$ are the energies of the AA, BB, and AB pairs, respectively. The Flory-Huggins interaction parameter is defined by

$$\chi = \frac{z}{kT} \left(\varepsilon_{AB} - \frac{1}{2}(\varepsilon_{AA} + \varepsilon_{BB}) \right). \quad (2.4)$$

ΔH_m can be written as

$$\Delta H_m = kT\chi\phi_A\phi_B. \quad (2.5)$$

The term χkT refers to the energy change when a neighboring unit is replaced by the unit of the other polymer species. In most cases, van der Waals interactions between the same monomers are stronger than between unlike pairs, which implies $\Delta H_m > 0$ and therefore opposes mixing. The Flory-Huggins model considers χ to be based purely on van der Waals

interactions, resulting in temperature dependence: $\chi \propto T^{-1}$. This implies that polymers can mix at high temperatures and phase separation occurs when the temperature is lowered. The critical temperature is called the upper critical solution temperature (UCST). However, it is also observed that many polymer mixtures that phase separate as the temperature is raised, which leads to a lower critical solution temperature (LCST). This means that χ must also have an entropic contribution arising from packing constraints on the level of the polymer units.

The Flory-Huggins free energy of mixing per lattice site can be expressed by applying Equation 2.2 and Equation 2.5 in Equation 2.1,

$$\frac{\Delta F_m}{kT} = \frac{\phi_A}{N_A} \ln \phi_A + \frac{\phi_B}{N_B} \ln \phi_B + \chi \phi_A \phi_B. \quad (2.6)$$

The first two terms of the right hand side in Equation 2.6 are related to the entropy of mixing and the third term is assigned to the enthalpy of mixing. For polymer-polymer blends, the entropic contribution is generally very small due to length and size of polymer chains, therefore, the miscibility of the system mainly depends on the value of ΔH_m , which must be equally small or negative.

2.4.2 Phase Diagrams

The Flory-Huggins theory is used to predict the mixing behavior of a system. The free energy of mixing is plotted as a function of composition at given temperatures (Figure 2.10a). If the free energy curve is concave ($\partial^2 F / \partial^2 \phi < 0$) with no inflection points, the system is not miscible for all compositions. If the curve is convex ($\partial^2 F / \partial^2 \phi > 0$), then the mixture is locally stable.

The phase diagram can be constructed using the common tangent rule. A line is drawn tangent to ΔF_m at two compositions ϕ_1 and ϕ_2 ,

$$\frac{F(\phi_1) - F(\phi_2)}{\phi_1 - \phi_2} = \left(\frac{\partial F}{\partial \phi} \right)_{\phi=\phi_1} = \left(\frac{\partial F}{\partial \phi} \right)_{\phi=\phi_2}. \quad (2.7)$$

The binodal line is formed by connecting ϕ_1 and ϕ_2 for different temperatures T . It separates the miscible one-phase region from the two-phase region, and determines the composition

of each separated phase.

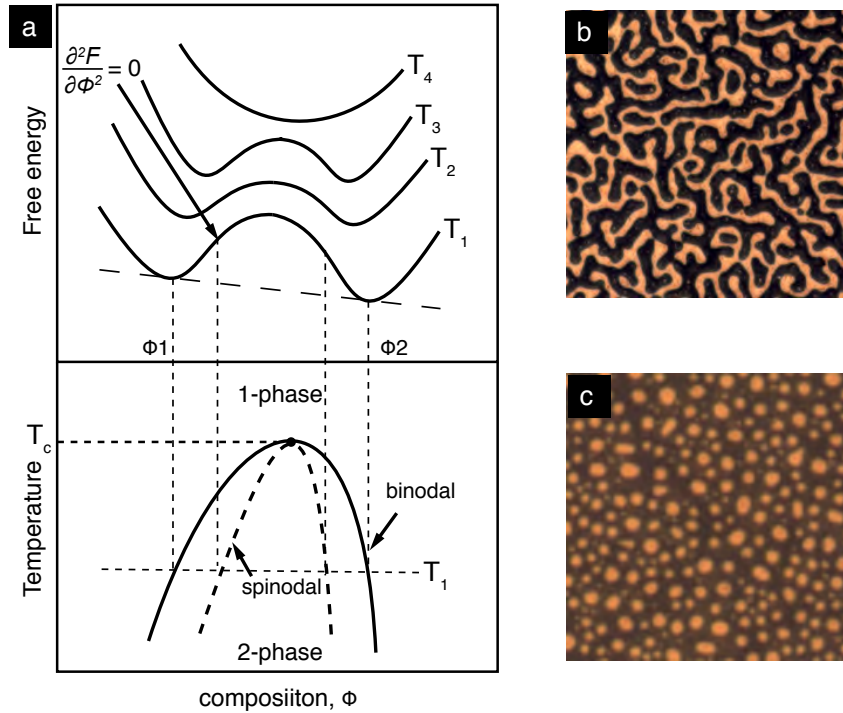


Figure 2.10 a) The free energy of mixing frame is described by Equation 2.6 for different temperatures T (upper frame) and corresponding phase diagram (lower frame). Examples of structure patterns emerging during phase separation by b) spinodal decomposition and c) nucleation and growth. Modified from "Polymers: Chemistry & Physics of Modern Materials".⁴⁸

The spinodal curve is the separative line between concave and convex parts of the free energy curve,

$$\frac{\partial^2 F}{\partial \phi^2} = 0. \quad (2.8)$$

The spinodal line is derived as

$$\chi_s = \frac{1}{2} \left(\frac{1}{N_A \phi} + \frac{1}{N_B (1 - \phi)} \right). \quad (2.9)$$

The mixed state in the spinodal region is unstable under thermal fluctuations, and phase separation occurs spontaneously without an energy barrier, which is known as spinodal decomposition. It typically produces bicontinuous structures with a characteristic length scale. (Figure 2.10b) predicted by the Cahn-Hilliard theory. The region between the binodal and spinodal line is metastable and a different mode of phase separation called "nucleation

and growth" occurs in this region, between the solid and dashed line in the phase diagram of Figure 2.10a. The binodal and spinodal intersect at the critical point where

$$\frac{\partial^3 F}{\partial \phi^3} = 0. \quad (2.10)$$

The value of ϕ_c and χ_c at critical point can be solved, yielding

$$\chi_c = \frac{1}{2} \left(\frac{1}{\sqrt{N_A}} + \frac{1}{\sqrt{N_B}} \right)^2, \quad (2.11)$$

$$\phi_c = \frac{\sqrt{N_B}}{\sqrt{N_A} + \sqrt{N_B}}. \quad (2.12)$$

For a symmetric polymer mixture, $N_A = N_B = N$, the phase diagram is symmetric with respect to the critical composition

$$\phi_c = \frac{1}{2} \quad (2.13)$$

and the critical interaction parameter

$$\chi_c = \frac{2}{N}. \quad (2.14)$$

This implies that χ_c decreases with increasing molecular weight of the polymers. Due to the large value of N_A and N_B , χ_c is usually very small, most polymers have $\chi > \chi_c$, and the systems are phase separated over the composition range within the miscibility gap. Only polymers with either weak repulsion, $0 < \chi < \chi_c$, or attraction, $\chi < 0$, between two components can form homogeneous one-phase mixtures at any composition. Regarding the Flory-Huggins theory, one may refer to the textbook "Polymer Physics".⁴⁹

2.5 Surface Enrichment in Polymer Blends

The thermodynamics of mixing discussed in the previous section considers bulk mixtures of polymer A and polymer B. However, there is a difference between the compositions in bulk and close to a surface in many polymer blends. This also occurs at the interface between a polymer blend and the substrate in thin films. Surface enrichment of one component in a mixture is related to the lowering of the system's free energy, which is achieved by having a

larger concentration of the component with lower surface energy at the surface. Therefore, the presence of two interfaces has an effect on the morphology which is in turn determined by the interplay of wetting kinetics and phase separation.⁵⁰

When the system is in the one phase regime of the phase diagram, the growth of a wetting layer is diffusion limited. The surface is enriched with the polymer of lower surface energy and the adjacent layer is depleted in this polymer. The kinetics of segregation is controlled by diffusion of this polymer from the bulk down the concentration gradient into the depleted region, which supplies the growth of the wetting layer (Figure 2.11). As the enriched wetting layer nears equilibrium, the diffusion gradient becomes smaller and smaller as the composition in the depleted layer approaches the bulk composition. The diffusion-limited surface layer growth is described by a mean-field square gradient model,^{51,52} which indicates that the size of the surface excess z^* scales with time t as $(Dt)^{1/2}$, where D is the diffusion coefficient of the polymer blend.⁵³

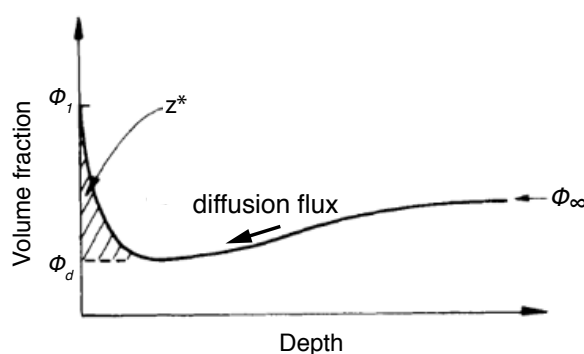


Figure 2.11 Schematic illustration of the diffusion limited model for the growth of a wetting layer.⁵²

As the system approaches either the critical point or the binodal line, the polymer of low surface energy is also attracted to the surface and leaves a depleted region similar to that in Figure 2.11. However, because the system is inside the spinodal line, the mutual diffusion coefficient is negative, i.e., the material diffuses from regions of lower concentration to regions of high concentration, the composition gradient becomes steeper and a secondary layer of high concentration is formed, eventually resulting in an oscillatory composition wave near the surface (Figure 2.12a). This phenomenon is called surface-directed spinodal decomposition.⁵²

Surface-directed spinodal decomposition was first observed in a polymer blend of

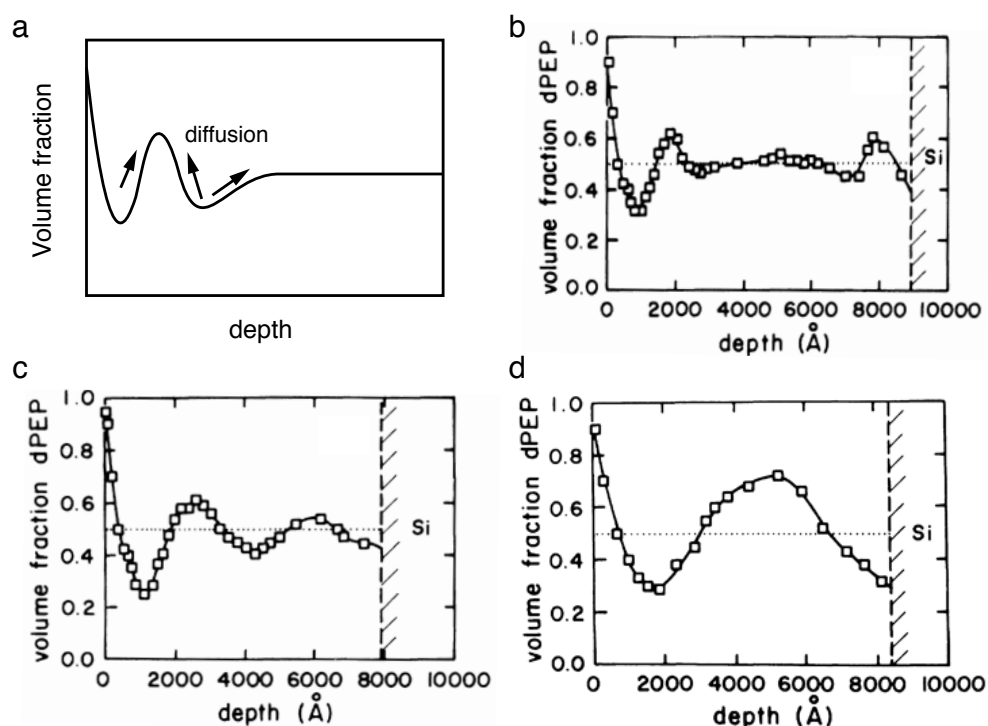


Figure 2.12 a) Schematic illustration of a surface-directed spinodal decomposition. Material has diffused from regions of low concentration to regions of high concentration (uphill diffusion), leading to a secondary maximum. Segregation depth profiles of the polymer blend of PEP/dPEP with a volume fraction of 0.5 after annealing at 35 °C for b) 19200 s, c) 64440 s, and d) 172800 s. The average composition of the blend is denoted by a dotted line.^{51,52}

poly(ethylene-propylene) (PEP) with its deuterated analogue (dPEP).⁵² Here, phase separation does not proceed isotropically as in the bulk, but is directed by the surface. A layered structure is observed with surface that is preferentially wetted by dPEP and with an adjacent sub-layer rich in PEP. The composition waves with wave vectors normal to the surface propagate into the bulk (Figure 2.12b, c, and d).

Similar composition waves have also been observed in other polymer blends such as deuterated polystyrene with brominated polystyrene,⁵⁴ polystyrene with poly(α -methyl styrene),⁵⁵ and polystyrene with tetramethylbisphenol-A-polycarbonate.⁵⁶ During the early stage of phase separation, the wavelength of the composition wave is essentially the same as that of the corresponding bulk process. At later stages of phase separation, a surface layer coexists with bulk isotropic phase separation, and the distance to the point where the composition resumes its average value varies with time as $t^{1/3}$.

2.6 Semicrystalline Polymers

2.6.1 The Crystal Lamellae

Polymers can crystallize by orienting the axes of chains with identical conformation parallel to each other and then packing laterally in a regular manner. It is identified that polymer crystals consist of stacked layers, each layer being an assembly of chains with identical conformation. These crystalline layers are separated by disordered regions with non-crystallizable parts consisting of chain entanglements, end-groups, short chain branches, stereo defects, etc. This results in the semicrystalline nature of polymers since only a fraction of polymer chains can participate in the crystal formation. The percentage of ordered chains in polymer is called crystallinity, and it typically ranges between 10% and 80%. The semicrystalline structure of polymers has been described by the following models.

The Fringed Micellar Model

The fringed micellar model is based on the fact that polymers consist of both crystalline and amorphous phases as evidenced by sharp diffraction patterns and a diffused circle observed in X-ray scattering. The crystalline parts are formed by bundles of aligned polymer chains. The bundles can grow along the chain axis, which is connected by intermediate amorphous regions. The growth of the crystalline bundles is hindered by the presence of the entangled chain segments and strained regions, which constitute the amorphous region (Figure 2.13a). The crystalline domain with random orientation is usually smaller than the length of polymer chain, and one polymer chain can traverse several crystalline domains.

The Chain Folded Lamellar Model

As first proposed by Keller in 1957, the chain folded lamellar model is based on his observation that polyethylene single crystals are comprised of very thin platelets with a thickness of ~ 10 nm, independent of molecular weight, and the chain axis is perpendicular to the thickness direction. The chains must be folded because the crystal thickness is much smaller than the chain extended length (10^2 - 10^3 nm). The model depicts a stack of polymer chains folded back on themselves to produce parallel chains perpendicular to the lamellar surface

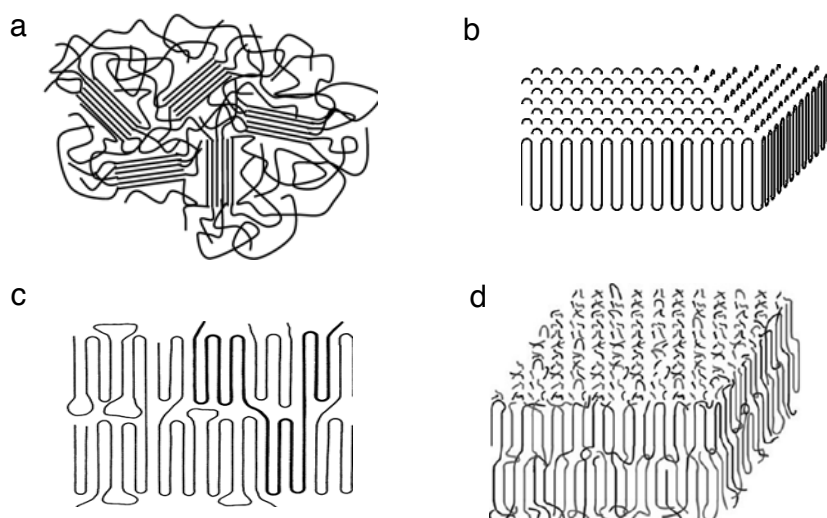


Figure 2.13 Schematic illustrations of a) the fringed micellar model; the chain folded lamellar model with adjacent re-entry b) with sharp folds, c) with loose folds. d) Random re-entry or switchboard model.

(Figure 2.13b). This lamellar crystal has indeed been demonstrated to be the predominant structure element in polymer crystallization. There are some other models such as adjacent re-entry with loose folds that have been modified from Keller's chain folding model (Figure 2.13c).

The Switchboard Model

In the switchboard model, the polymer chains randomly fold and participate in the same or neighboring lamellae, as shown in Figure 2.13d. Starting from polymer melts with chains in random coil conformations, it is impossible to meet the spatial requirements that approach the ideal adjacent re-entry chain folding model, but adjust locally to generate the crystalline phase. Therefore, large parts of the polymer chains remain in the disordered amorphous phase. The re-entry is proposed to occur via loops of varying length in the amorphous phase. The adjacent segments in lamellar crystals can be from the same or different polymer chains. After the polymer chain enters a lamellar crystal, it can traverse into another lamellae or re-enter the same lamellae at non-adjacent positions. It is also possible that some chains do not re-enter the lamellar crystals but remain in the amorphous region.

2.6.2 Supermolecular Structure

Polymer crystallization is governed by kinetical rules rather than by equilibrium thermodynamics, meaning that the structure that develops at a given temperature is determined by the maximum rate of development rather than the lowest free energy. Crystal formation in polymer melts starts with nucleation, both heterogeneous and homogeneous. Heterogeneous nucleation is generally initiated at defects, impurities or interfaces, whereas homogeneous nucleation forms by thermal fluctuations to overcome the nucleation barrier. After nucleation, polymer crystal growth occurs by attaching long chains to the growth front and subsequent chain folding, therefore the rate of crystallization is relatively low because of slow chain motion.¹⁵

Spherulites are most common in semicrystalline polymers when crystallized from the melt. As the structures often appear to be spherical in shape, they are called spherulites. Spherulites exhibit a multi-scale hierarchical structure. At the molecular level, the polymer chains adopt regular sequences to form periodic lattice structures with a unit cell on the length scale of ~ 1 nm and lamellar crystal sizes of ~ 10 nm. At the micrometer or larger length scale, the lamellar crystals further assemble into spherulites radiating from the center outwards. The structure is illustrated schematically in Figure 2.14a. It is shown that the individual lamellar crystals are separated by amorphous regions. Tie molecules connect the adjacent lamellae passing through the amorphous regions.⁵⁷

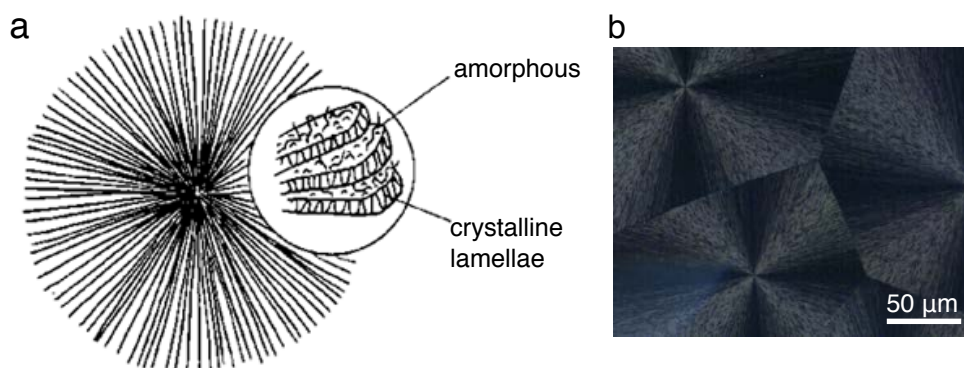


Figure 2.14 a) Schematic illustration of a spherulite composed of alternating crystalline lamellae and amorphous region.⁵⁸ b) Example of polyethylene oxide spherulites observed under polarized optical microscopy. Alignment of polymer chains within the lamellae results in birefringence producing the Maltese cross pattern.

The growth of polymer spherulites is described by the nucleation and growth process. Ini-

tially, the crystal nucleus form as a single lamellar crystal and growth continues as the polymer chains keep folding and crystal defects lead to lamellar branching and splaying. This creates a sheaf-like structure, and as more layers form, eventually a full spherical growth surface is established. Studies show that the spherulites grow at a constant rate in radial direction until they fill up the space and touch each other. The size of spherulites vary from $\sim 0.1 \mu\text{m}$ to several millimeters depending on the nucleation density.

Spherulites show a characteristic extinction cross, which is called Maltese cross, between crossed polarizers (Figure 2.14b). The Maltese cross is centered at the origin of the spherulite, and the extinction arms of the cross are oriented parallel to the direction of polarizer and analyzer. The optical anisotropy in the crystalline region arises from the perpendicular alignment of polymer chains to the radius direction. The appearance of this Maltese cross reflects the birefringence and structure symmetry of spherulites.

Polymers can also crystallize during solvent evaporation or mechanical stretching. Affected by the processing conditions, different forms of crystal structures are produced such as single crystals, dendrite, fibril and string crystals like the shish-kebab structure. Crystallization in turn affects optical, mechanical, thermal and chemical properties of the polymer.

2.6.3 Semicrystalline Structure of Poly(3-hexylthiophene) (P3HT)

P3HT is one of the most promising conjugated polymers for organic photovoltaics. P3HT is used as the donor polymer in combination with PCBM or F8TBT as acceptors in this thesis. P3HT has a structure of polythiophene backbones with flexible alkyl side groups (C_6H_{13}). Depending on the position at which the thiophene units are connected, either the 2- or 5-position, the polymer chain exists in three configurations, head-to-tail (HT), head-to-head (HH) and tail-to-tail (TT). Regioregular P3HT have ordered structures with the side groups HT arranged (Figure 2.15a), while regiorandom P3HT consists of HT, HH and TT side groups in random order (Figure 2.15b).

The regioregularity of P3HT affects the crystallinity of P3HT. Regioregular P3HT has strong tendency to crystallize as a result of its ordered structure and strong intermolecular π - π interactions. It shows charge carrier mobilities several orders of magnitude higher than regiorandom P3HT. Regioregular P3HT assembles into a lamellar structure with altern-

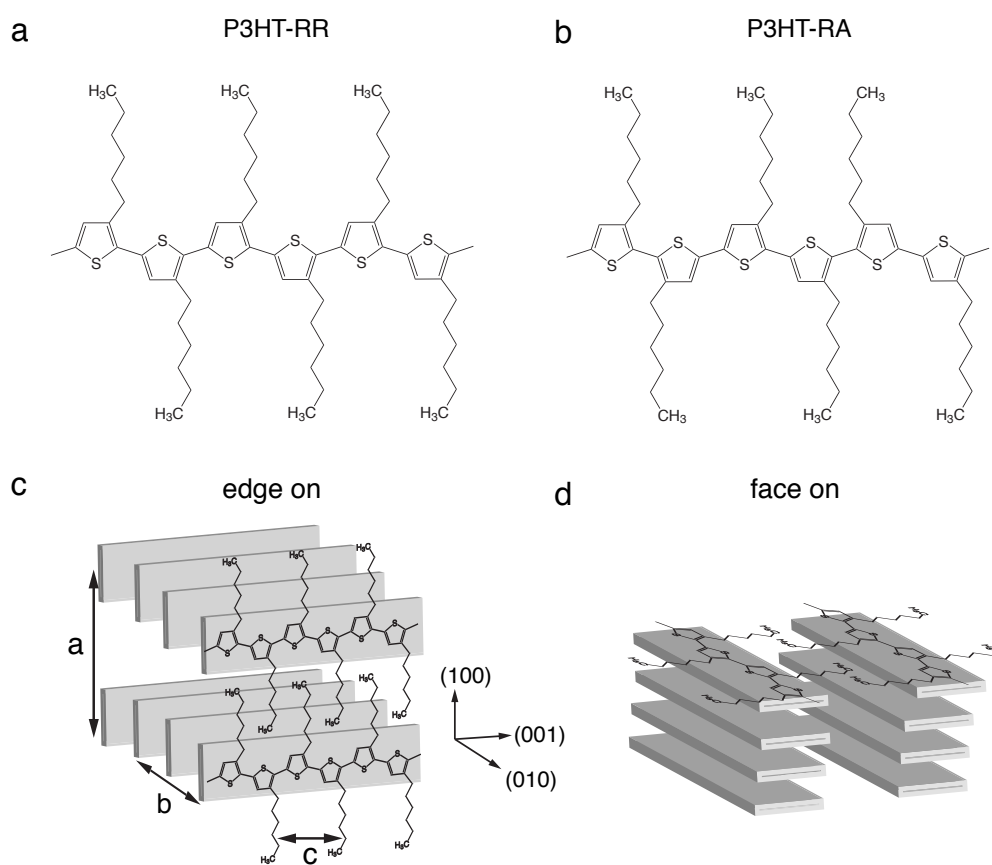


Figure 2.15 Chemical structures of a) regioregular P3HT (P3HT-RR) and b) regiorandom P3HT (P3HT-RA). Schematic models of P3HT crystals with c) edge-on and d) face-on orientation.

ating layers of polythiophene backbones with alkyl chains. As shown in Figure 2.15c and d, P3HT crystallites with their alkyl chains stacking out-of-plane is called "edge on" whereas an alkyl stacking direction in the plane of the substrate is called "face on" orientation. In solution cast P3HT thin films, edge on orientation of P3HT is mainly adopted. As the adjacent chains stack face-to-face allowing for the overlap of their π -orbitals, this leads to two directions for charge delocalization: 1) in the chain backbone direction; 2) along the π -stacking direction. The alkyl side chain between the backbone layer is insulating, resulting in poor charge transport in this direction. Thus the orientation of P3HT is important from the device point of view because of the anisotropic electronic properties of P3HT.

The crystalline structure of P3HT has been well characterized by X-ray diffraction.^{59,60} The crystal axes are defined in Figure 2.15c. The corresponding lattice parameters are $a = 16.0 \text{ \AA}$, $b = 7.8 \text{ \AA}$ and $c = 7.8 \text{ \AA}$.⁶¹ P3HT crystallizes with alternating crystalline lamellae separ-

ated by amorphous interlayers, and the lamellar thickness is dependent on the molecular weight. The lamellar periodicity increases with increasing the molecular weight of P3HT, and it saturates when chain folding occurs. In low molecular weight (MW) P3HT ($M_w = 7.3$ kDa), the thiophene backbone with all-*trans* conformation is fully extended, giving a lamellar periodicity of 11.5 nm, close to the chain contour length. On the other hand, for higher MW ($M_w = 18.8$ kDa) P3HT, the lamellar thickness reaches a value of 25-28 nm, and it remains constant regardless of the increase in MW.^{61,62} This implies that the chain conformation starts to change from fully extended to folded at a critical M_w , although the relatively rigid polythiophene backbone is thought to hamper chain folding.

P3HT thin films consist of crystalline domains with a thickness of approximately 10-20 nm, separated by amorphous grain boundaries. Since amorphous domains impair charge transport, efforts have been made to improve the film crystallinity. The crystallinity and crystal orientation of P3HT depends not only on the molecular properties that include regioregularity, MW and polydispersity, but also on processing conditions.⁶³⁻⁶⁵ Even though the low MW P3HT is more crystalline, the mobility increases by orders of magnitude with increasing MW.⁶⁶⁻⁶⁸ The dependence of mobility in P3HT on MW has been related to disordered grain boundaries and inherent effects of chain length on the electronic structure. Furthermore, in high MW P3HT, tie molecules that interconnect crystalline domains through the amorphous regions are thought to contribute to the charge transport.⁶¹

Different types of crystal morphologies have been observed in P3HT thin films. P3HT shows a strong tendency to form nanowires with an average width of ~ 20 nm, length of several microns and thickness of ~ 5 nm (corresponding to several layers of polymer chains). Chain folding occurs in P3HT nanowires because the width of nanowires is smaller than the contour length. Attempts have been made to control the P3HT crystal morphology by epitaxial growth methods. P3HT forms a shish-kebab fiber morphology on the surface of 1,3,5-trichlorobenzene (TCB) crystalline needles.⁶⁹ Spherulites of P3HT have also been obtained by epitaxial crystallization on TCB crystals during spin coating.⁷⁰ Moreover, uniaxial orientation of P3HT chains was realized by mechanical rubbing, leading to anisotropic optical properties.⁷¹ The development of methods for controlling crystal morphology would offer opportunities for the design of new optoelectronic devices.

Chapter 3 Materials and Experimental Techniques

3.1 Materials

The materials used in the study are listed in Table 3.1.

Table 3.1 Materials used in the experiments. PDI refers to the polydispersity of polymers, $PDI = M_w/M_n$, where M_w is the weight averaged molecular weight and M_n is the number averaged molecular weight.

Material	Abbreviation	M_n (g/mol)	PDI	Source
Poly(3-hexylthiophene), regioregularity > 95%	P3HT-RR1	20000-40000	~2.0	Sepiolid P200
Poly(3-hexylthiophene), regioregularity = 100%	P3HT-RR2	11822	1.1	synthesized ⁷²
Poly(3-hexylthiophene), regiorandom	P3HT-RA	20000-30000	~3.0	Rieke metals, 4007
Poly((9,9-dioctylfluorene)-2,7- diyl-alt-[4,7-bis(3-hexylthien- 5-yl)-2,1,3-benzothiadiazole]- 20,200-diyl)	F8TBT	49300	2.4	synthesized ⁷²
Phenyl-C61-butyric-acid methyl ester	PCBM	-	-	Nano-C
Polystyrene, atactic	PS	29000	1.1	Polymer source
Poly(ethylene oxide)	PEO	90000	2.2	Polymer source

The chemical structures of the main materials are shown in Figure 3.1

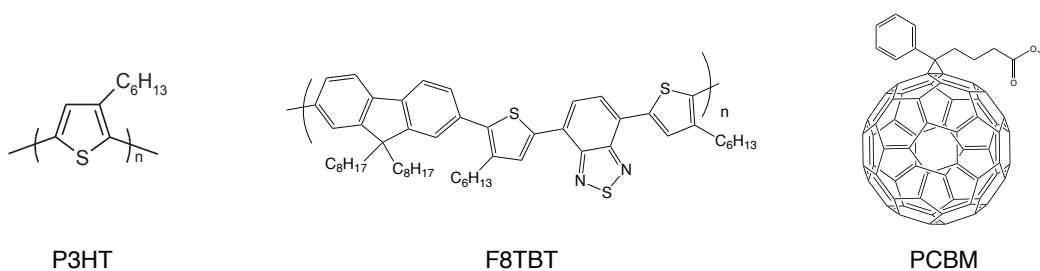


Figure 3.1 Chemical structures of P3HT, F8TBT, and PCBM.

3.2 Sample Preparation

3.2.1 Thin Film Deposition

Silicon or Spectrosil quartz glass substrates were cleaned by snowjet and oxygen plasma for 10 min to remove surface contaminations and organic particles before film deposition. Spin coating was used to deposit uniform thin films, which is described by the following steps: 1) applying a small amount of solution ($\sim 60 \mu\text{L}$) on the center of the substrate; 2) the substrate is accelerated to spread out the solution by the centrifugal force; 3) the substrate is rotated at a constant speed to thin the solution towards its final thickness. Evaporation of solvent during this stage leads to an increase in the viscosity of the solution, slowing the shear thinning of the film. The film thickness is determined by the competition between the centrifugal force and the solvent evaporation rate. Thus, the film thickness can be adjusted by the solution concentration, the evaporation rate of solvent, and the rotation speed.⁷³

3.2.2 Solvent Vapor Annealing

The polymer-solvent interaction has been studied by measuring the swelling isotherm of polymer films when exposed to different saturations of solvent vapor.^{74,75} The setup used to introduce a controlled solvent vapor is shown in Figure 3.2. Nitrogen was bubbled through the solvent container, combined with dry nitrogen at the volume fraction adjusted by flow controllers, and finally directed to the measurement chamber. The sample was fixed into a chamber with quartz windows on the top and bottom sides, allowing *in situ* absorption spectroscopy measurements. The gas flow was regulated by two MKS mass flow controllers with a typical rate of 50 sccm and the temperature of solvent container was maintained at 21 °C by a water thermostat. The relative vapor pressure p/p_{sat} was adjusted from 0.00 to

1.00, corresponding to the flow ratio of the two nitrogen streams.

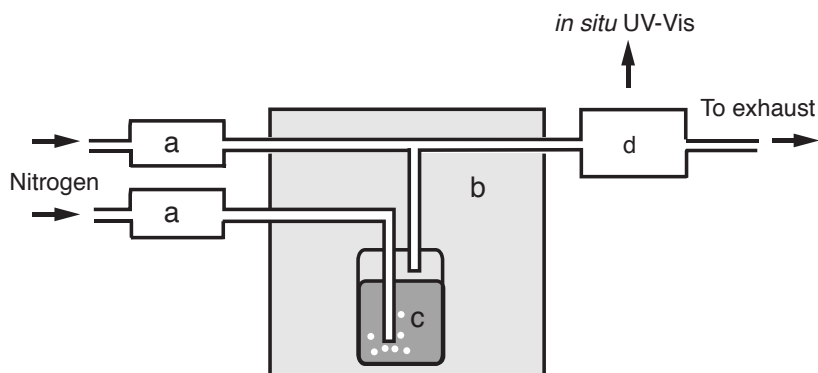


Figure 3.2 Solvent vapor annealing setup: a: flow controller; b: water thermostat; c: solvent container; d: sample chamber.

3.2.3 Device Fabrication

Polymer solar cells were fabricated with standard and inverted structures as shown in Figure 3.3.

Standard Solar Cell

Indium tin oxide (ITO) glass substrates were sonicated in acetone followed by isopropanol for 15 min each. The ITO substrates were further cleaned in oxygen plasma for 10 min. An anode buffer layer of PEDOT:PSS was spin coated onto the substrate at 5000 rpm followed by annealing under nitrogen flow on a hotplate at 150 °C for 30 min to remove residual water. The substrates were immediately transferred into a glovebox for the subsequent processing.

Device photoactive layers were spin-coated onto the PEDOT:PSS at various speeds to achieve desired thickness. The photoactive layer thickness was measured by a Dektak profilometer. The top electrode was thermally evaporated onto the photoactive layer through

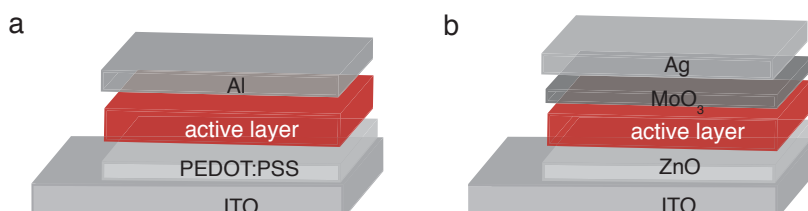


Figure 3.3 Schematic structures of a) standard and b) inverted photovoltaic devices.

a shadow mask at a pressure lower than 5×10^{-6} mBar. Standard devices were completed with 100 nm of the low work function Al as the cathode. Devices were treated either by thermal annealing on a hotplate in the glovebox at 140 °C for 10 min after Al deposition or by solvent vapor annealing before Al deposition. Devices were encapsulated prior to testing. The active area of each device was 4.5 mm².

Inverted Solar Cell

The inverted device architecture is illustrated in Figure 3.3b. A ZnO layer was deposited onto ITO substrates by spin coating from a 50 mg/mL chloroform solution at 5000 rpm followed by annealing at 150 °C for 30 min in a glovebox. The thickness of the ZnO layer was ~ 50 nm. The ZnO nanoparticle solution was synthesized by Cheng Li according to the literature.⁷⁶ The photoactive layers were prepared in the same way as in standard devices. Top electrodes were deposited by thermal evaporation of MoO₃ (8 nm) and Ag (100 nm) through a shadow mask.

3.3 Characterization Techniques

3.3.1 Solar Cells Characterization

External Quantum Efficiency

The external quantum efficiency (EQE) measures the charge carriers generated per incident photon. The EQE spectrum acquires the short circuit current and the incident photon flux as a function of wavelength, as actual device performance is strongly dependent on the spectral distribution of light source. In the EQE measurement, a 250W tungsten halogen lamp and an Oriel Cornerstone 130 monochromator were used as the light source and the current was recorded using a Keithley 237 source measurement unit. The monochromatic light was focused into an area smaller than the device area and the photon flux was determined using a silicon photodiode. The EQE was collected from 375 to 900 nm with a resolution of 5 nm.

Current-Voltage Characteristic

The power conversion efficiency of solar cells was measured under the standardized testing condition of Air Mass 1.5 (AM 1.5) illumination (100 mW/cm^2). The current-voltage (J - V) curves were measured in the dark and under illumination using an ABET Solar 2000 solar simulator. The light intensity was calibrated to a silicon reference cell, corrected for spectral mismatch. The J - V characteristics were measured using a Keithley 237 source measurement unit.

3.3.2 Optical Microscopy

Optical microscopy was used to study the film morphology. Images were taken using Olympus BX-51 microscope with UM-PlanFI 50 mm $f/0.95$ lens and a digital camera.

3.3.3 Atomic Force Microscopy

Atomic force microscopy (AFM) is based on the measurement of forces between the tip and the sample. When the tip approaches the sample, interatomic forces, i.e., van der Waals forces, dipole-dipole interactions and electrostatic forces, cause the bending of the cantilever. The deflection of the cantilever is detected by a reflected laser spot with a photodiode. The cantilever is driven by a piezoelectric actuator to oscillate near its resonant frequency while scanning over the sample surface. A feedback loop is used to maintain a constant oscillation amplitude of the cantilever by adjusting the height above the sample. AFM measurements were performed in the tapping mode using a Nanoscope IV Dimension 3100 (Veeco Instruments Inc.) microscope. In this study, topographic and phase images were used to study the phase separation morphology of polymer thin films.

3.3.4 Scanning Electron Microscopy

Scanning electron microscopy (SEM) is a type of electron microscopy that uses highly energetic electron beams to image the samples. The incident beam interact with electrons in the sample, producing various signals that can be used for surface topography and composition analysis. SEM produces images by detecting the secondary electrons (SE) and back-scattered electrons, which result from the interactions of the electron beam with atoms at or near the

sample surface. The low energy (<50 eV) secondary electrons are emitted from atomic orbitals by inelastic scattering interactions with incident electrons. Secondary electron imaging is the most common detection mode, which can produce very high resolution images of a sample surface. Backscattered electrons are high energy electrons that are reflected or back-scattered out of the sample by elastic scattering interactions with atoms. The detection of back-scattered electrons can be used for chemical composition as the scattering rate is predominately dependent on the atomic number of the material. The spatial resolution of SEM depends on the electron spot size and the interaction volume. The resolution can range from 1 nm to macroscopic scales. A Leo 1530 SEM was used in this project at 5 kV acceleration voltage, and detection was performed by an in-lens secondary electron detector.

3.3.5 Transmission Electron Microscopy

Transmission electron microscopy (TEM) is a microscopy technique that uses a high voltage electron beam to image samples in transmission. The thin film sample is irradiated with a beam of electrons which is focussed by electromagnetic lenses. The electrons interact with the sample as they pass through and the level of interaction depends on the electron density of the material. In the bright-field mode, the transmitted beam is used to form the image, thereby regions with larger thickness or higher atomic number appear with dark contrast. The resolution of TEM is higher than that of SEM and it can go down to 0.5 Å. A FEI Philips Tecnai 20 TEM system operating at 200 kV was used in this study. Thin films were floated off the substrate and transferred onto a copper mesh before imaging.

3.3.6 Ultraviolet-Visible Absorption Spectroscopy

Ultraviolet-visible (UV-Vis) absorption spectroscopy is widely used in analytical chemistry for the determination of materials such as conjugated organic chemicals, transition metal ions, and biological macromolecules. These materials can absorb energy in the form of light in the UV and visible wavelengths and undergo electronic transitions. Samples for UV-Vis spectroscopy are most often in solution, although the absorption in the thin film form can also be measured. The intensity of light is measured before (I_0) and after (I) passing through a sample. The ratio of I/I_0 is defined as the transmittance (T) and the absorbance (A) is

calculated by the Beer-Lamber law:

$$A = -\log T = -\log I/I_0. \quad (3.1)$$

The absorption is directly proportional to the concentration of the absorbing chemicals in the solution and the path length. However, at sufficiently high concentrations, the absorption peak will saturate and show absorption flattening. A Hewlett Packard 8453 UV-Vis spectrometer was used to obtain the absorbance spectra in this study. 100 nm thick Polymer films were spin coated on spectroil quartz glass. Polymer solutions with a concentration of 2 mg/mL were placed in a Helma quartz cuvette with a 1 cm path length.

3.3.7 Photoluminescence Spectroscopy

Photoluminescence (PL) is a process of photo excitation followed by the re-emission of photons. Upon photo excitation, photons are absorbed and electrons are moved from the ground state to excited states. After internal energy transitions, the electrons eventually fall back to the ground state accompanied by the emission of photons. The PL technique can be used to study the photo-induced electron transfer that occurs in conjugated polymers. A Varian fluorimeter was used in this study. Thin film samples were excited with a monochromatic light at 470 nm, and the PL signal was collected at a fixed angle relative to incidence using a monochromator for wavelengths from 550 to 850 nm. PL was used to characterize the changes in charge separation between donor and acceptor phases in photovoltaic blends in the study.

3.3.8 X-ray Scattering

Small and Wide Angle X-ray Scattering

X-ray scattering techniques measure the scattering intensity of X-rays as a function of the scattering angle, which provides structural information by imaging in reciprocal space.⁷⁷ The constructive interference of X-rays after interacting with a periodic structure occurs when the Bragg's Law is satisfied,

$$n\lambda = 2d \sin \theta, \quad (3.2)$$

where $n=1, 2, 3\dots$ is the integer diffraction order, and λ is the X-ray wavelength, θ is the scattering angle, and d is the periodic lattice spacing. The scattering vector q is defined by the scattering angle θ according to

$$q = \frac{4\pi \sin \theta}{\lambda}, \quad (3.3)$$

where

$$q = \frac{2\pi}{d}. \quad (3.4)$$

The small and wide angle X-ray scattering (SAXS and WAXS) experimental geometries are shown in Figure 3.4a. An incident beam of X-ray penetrates through the sample and the scattered intensity is recorded by a detector. The non-scattered beam is blocked. SAXS measurements are typically recorded at angles from $2\theta = 0.1^\circ \sim 10^\circ$. It is mostly used to study the mesoscale structures with $d \gg \lambda$ in the 5 ~ 100 nm range. The peaks in SAXS are typically broadened in comparison to crystalline diffraction peaks due to the diminished degree of long range order. In contrast, WAXS detects at wide angles from $2\theta = 10^\circ \sim 80^\circ$, which is used for probing the atomic lattices of solid state materials.

In this study, SAXS and WAXS measurements were performed to investigate the structural and morphological changes of semicrystalline P3HT. The evolution of a distinct scattering maximum in SAXS was used to determine the long period, i.e., the sum of the average crystal and amorphous layer thickness (Figure 3.4b).

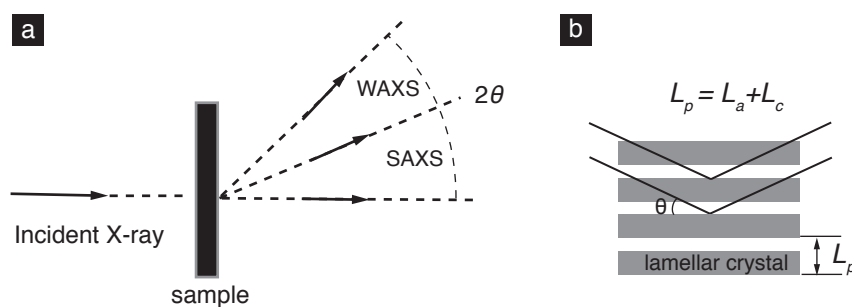


Figure 3.4 a) Schematic illustration of SAXS and WAXS measurements. b) Scattering from a stack of lamellar crystals (grey) with repeating long period (L_p). The long period is the sum of lamellar crystal thickness (L_c) and the amorphous layer thickness (L_a). The constructive interference condition is expressed by the Bragg equation.

Grazing-Incident X-ray Scattering

Grazing-incident X-ray scattering (GIXS) uses a reflection geometry instead of transmission in SAXS. This technique is particularly useful for studying nanostructures in thin films. GIXS has been widely used to study morphology evolution of photoactive layers in organic photovoltaics. The GIXS scattering geometry is shown in Figure 3.5. The X-ray beam impinges on the film at a low incident angle, α_i , to maximize the signal from the thin film. This geometry increases the diffracting volume and the scattering from the substrate can be avoided if α_i is below the critical angle of the substrate. Two dimensional scattering signals are recorded for a range of exit angles.

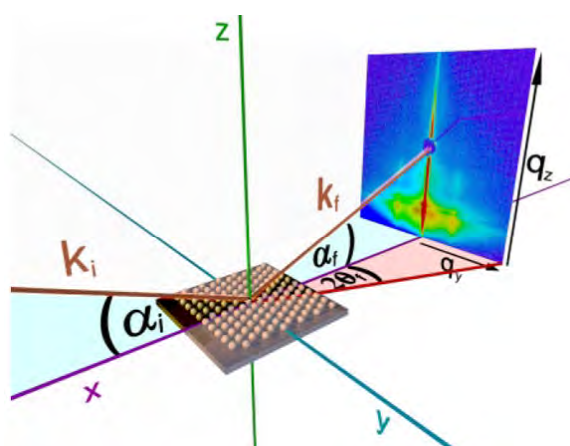


Figure 3.5 Schematic illustration of grazing-incident X-ray scattering measurements.⁷⁸

GIXS can be used to identify the nanostructure orientation along the vertical and lateral directions in thin film. For example, lamellar structures parallel and perpendicular to the surface in diblock copolymer films can be distinguished by GIXS.⁷⁹ More complex phases such as cylinders⁸⁰ and gyroid⁸¹ have been characterized by the technique. GIXS has also been used to determine the crystal thickness and orientation in semicrystalline polymer films.⁸²

X-ray Reflectivity

X-ray reflectivity (XR) is an important thin-film measurement technique. In difference to previous mentioned scattering technique, XR is not based on the diffraction phenomenon of crystalline structures. It is used to analyze X-ray reflection intensity curves from grazing

incident X-ray beam to determine thin-film parameters including thickness, density profile and surface or interface roughness. When X-rays are incident onto a sample surface, they undergo total external reflection when incident angle is smaller than the critical angle for total reflection (θ_c). Thus the X-ray reflectivity is related to the values of the refractive index and X-ray wavelength. Figure 3.6 shows the X-ray optics for the case of incident angles (θ) smaller, equal to and greater than θ_c . The intensity of X-rays specularly reflected from the surface is recorded as a function of θ . Interference of the reflected beams from the film surface and the bottom interface gives rise to the oscillations in reflectivity profiles. Electron density profiles can be obtained from the measured reflectivity data by using a parametric fit to assumed models.⁸³

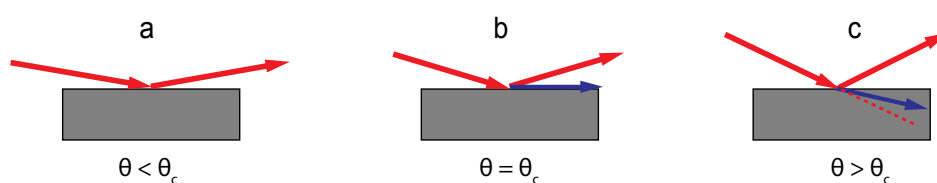


Figure 3.6 Reflection and refraction of X-rays at film surface at different incident angles. a) When $\theta < \theta_c$, all incident X-ray are reflected; b) when $\theta = \theta_c$, incident X-rays propagate along the film surface; c) when $\theta > \theta_c$, incident X-rays penetrate into the film by refraction.⁸³

Chapter 4 Crystallization-Induced 10 nm Structure Formation in P3HT/PCBM Blends

The solubility and aggregation of PCBM within a polymer matrix is of great interest for the further development of fullerene based organic photovoltaic cells. In this chapter, we have systematically investigated the morphology evolution in P3HT and PCBM blends. The segregation process of PCBM from the P3HT matrix via thermal annealing was investigated by optical microscopy. The relative crystallinity of P3HT directly relates to the nucleation density of PCBM for aggregation. The dissolution of PCBM into the inter-lamellar regions of P3HT was confirmed by X-ray scattering analysis using mono-dispersed regioregular P3HT. PCBM segregates out of the amorphous P3HT interlayers above a solubility limit. Our results show that the crystallization of P3HT with 10-nm lamellar domains determines the main length scale in P3HT/PCBM blends.

4.1 Introduction

The performance of organic photovoltaic cells (OPV) is dependent on the morphological organization of the donor and acceptor materials within the bulk heterojunction (BHJ) active layer.⁸⁴ Since separate charge carriers are formed only at the donor-acceptor interface, it is commonly assumed that excitons formed only within the diffusion length of such an interface contribute to the photocurrent. This defines the morphology of the conceptually optimal BHJ consisting of a bicontinuous donor-acceptor interface on a 10-nm length scale,

which led to the mostly empirical development of different ways for controlling the active layer morphology. While this model has guided device optimization for the past 10 years, little progress has been made in the understanding of the interplay of structures in BHJ and their device performance.

P3HT/PCBM blends are one of the most studied systems for understanding the correlation between structure and performance. The morphology of P3HT/PCBM thin films has been investigated by various methods, including X-ray⁸⁵⁻⁸⁷ and neutron scattering techniques,⁸⁸⁻⁹⁰ dynamic secondary ion mass spectrometry (DSIMS),⁹¹ X-ray photoemission spectroscopy (XPS),⁹² and transmission electron microscopy (TEM).^{38,93} It became clear that there is a certain miscibility of PCBM in amorphous P3HT which was confirmed by diffusion experiments.⁹⁴ P3HT/PCBM blends indeed consist of pure crystalline P3HT and PCBM phases as well as a molecularly mixed phase of amorphous P3HT and PCBM.^{95,96} The competition between P3HT crystallization and fullerene aggregation plays a crucial role in determining morphology and various experiments have been carried out to understand the processing and annealing procedures.^{39,97-100}

The research so far, mostly empirical, has determined optimum compositions of PCBM in polymers with processing conditions that presumably produce a nanostructure with carefully balanced donor and acceptor phases. Spinodal decomposition of donor-acceptor blends is the most often invoked model to describe phase separation in OPV blends. This has been thought to lead to a bicontinuous spinodal morphology. However, there are some fundamental limitations that question the suitability of this spinodal model to guide OPV device fabrication. Spinodal lengths are typically in micrometer range, and 10-nm patterns by spinodal decomposition have not been observed in binary polymer blends. The demixed phases are typically mixtures of two materials at different concentrations, while efficient charge transport requires pure domains of each material. Most conjugated polymers can crystallize, which leads to an interplay of crystallization and phase separation. Understanding the phase separation process in P3HT/PCBM blends, and how it is affected by P3HT crystallization, would provide a basis for provide a basis for designing organic solar cells based on other polymer blends.

In this study, we have investigated the structure formation process in P3HT/PCBM

blends. The macroscopic morphology of P3HT/PCBM thin films was investigated by optical microscopy and also compared to PS/PCBM blends. X-ray scattering was employed to reveal the nanostructure in bulk mixtures of P3HT/PCBM, and compared to thin film samples by using grazing-incident small and wide angle X-ray scattering (GISAXS and GIWAXS) measurements. A well-defined low molecular weight P3HT with high regio-regularity was used in the present work, and this P3HT arranges in a periodic superstructure separating amorphous and crystalline domains, which serves as an ideal model polymer to study structure formation by X-ray scattering. The results show that P3HT/PCBM structure formation is determined by the crystallization of P3HT followed by the enrichment, segregation, and crystallization of PCBM, which provides a nanostructure with ideal phase dimensions for excitonic solar cells.

4.2 Experimental Methods

Three P3HT batches were used: P3HT-RR1, P3HT-RR2, and P3HT-RA. Details of these materials can be found in Chapter 2. Solutions were prepared at a concentration of 30 mg/mL by dissolving polymers in chlorobenzene and heated to 75°C for 2 hrs. Thin film samples were spin coated from hot solutions at 1500 rpm at an acceleration of 500 rpm/s. Films were either thermally annealed (TA) at 175 °C for 2 hrs or melt annealed by first melting at 240 °C for 3 min followed by cooling to room temperature at 5 °C/min. Thin film samples were investigated by optical microscopy (OM), AFM in tapping mode and UV-Vis spectroscopy.

Bulk samples for SAXS and WAXS were prepared by scratching off spin coated films from Si substrates and filling into a hole (0.8 mm in diameter) in a small aluminium plate (1.5 mm in depth) for measurements. SAXS and WAXS measurements were performed on Beamline I22 at the Diamond Light Source, UK using a Pilatus 2M and a HOTWAXS 1D gas microstrip quadrant detector. GISAXS and GIWAXS measurements were performed at Beamlines BW4 (DORIS), HASYLAB at DESY in Hamburg, Germany. The wavelength of X-rays used was 0.138 nm, and the incident angle was 0.18° for GIWAXS and 0.38° for GISAXS. The scattered intensity was detected using a two-dimensional CCD camera. All the X-ray scattering measurements and data analysis were performed by Dr. Peter Kohn, Kai Hermann Scherer and Dr. Alessandro Sepe.

4.3 Results and Discussion

4.3.1 Miscibility of P3HT/PCBM

We first investigated the spin coated films of P3HT/PCBM blends as compared to PS/PCBM blends. The polymers were mixed with PCBM at weight ratios f ($m_{\text{PCBM}}/m_{\text{polymer}}$) from 0.5 to 4. In Figure 4.1a-d, no distinct feature can be discerned in the P3HT/PCBM films, irrespective of the PCBM mixing ratios. Using PS as the polymer matrix, PCBM separates into circular islands, which clearly shows phase separation directed morphology. The domain size ranges in diameter from approximately 50 nm for the $f = 0.5$ blend to 200-800 nm for the $f = 4$ blend. The difference between these two sample series indicates better compatibility in P3HT/PCBM blends. The lack of surface features in P3HT/PCBM may result from a vertically stratified structure of two separated phases, or an arrested phase coarsening by rapid solidification of the film, e.g. by crystallization of one of the components.

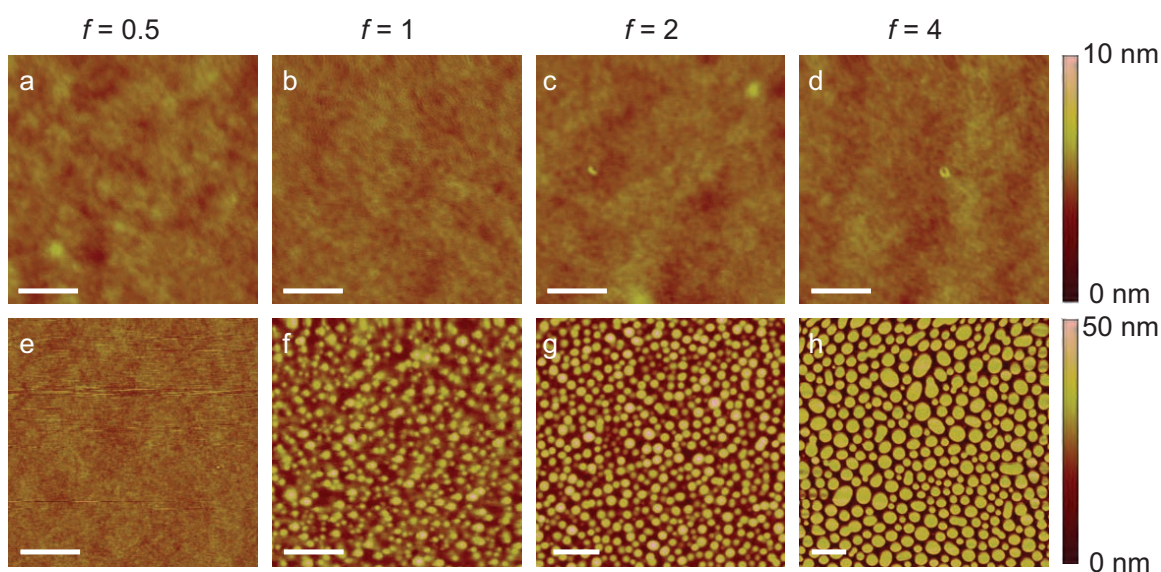


Figure 4.1 AFM images of (a-d) P3HT-RR1/PCBM thin films (scale bar: 500 nm) and (e-f) PS/PCBM thin films (scale bar: 1 μm). The PCBM to polymer weight fraction was varied from $f = 0.5$ to $f = 4$.

Three series of P3HT/PCBM blends were further investigated upon thermal annealing as shown in Figure 4.2. Two regioregular batches of P3HT (P3HT-RR1 and -RR2) and one regiorandom P3HT (P3HT-RA) were used as the matrix polymers. P3HT-RR2 has a low molecular weight ($M_n = 11800$ g/mol) with regioregularity (RR) of 100%, which forms a periodic superstructure of alternating crystalline and amorphous layers, whereas the P3HT-

4.3 Results and Discussion

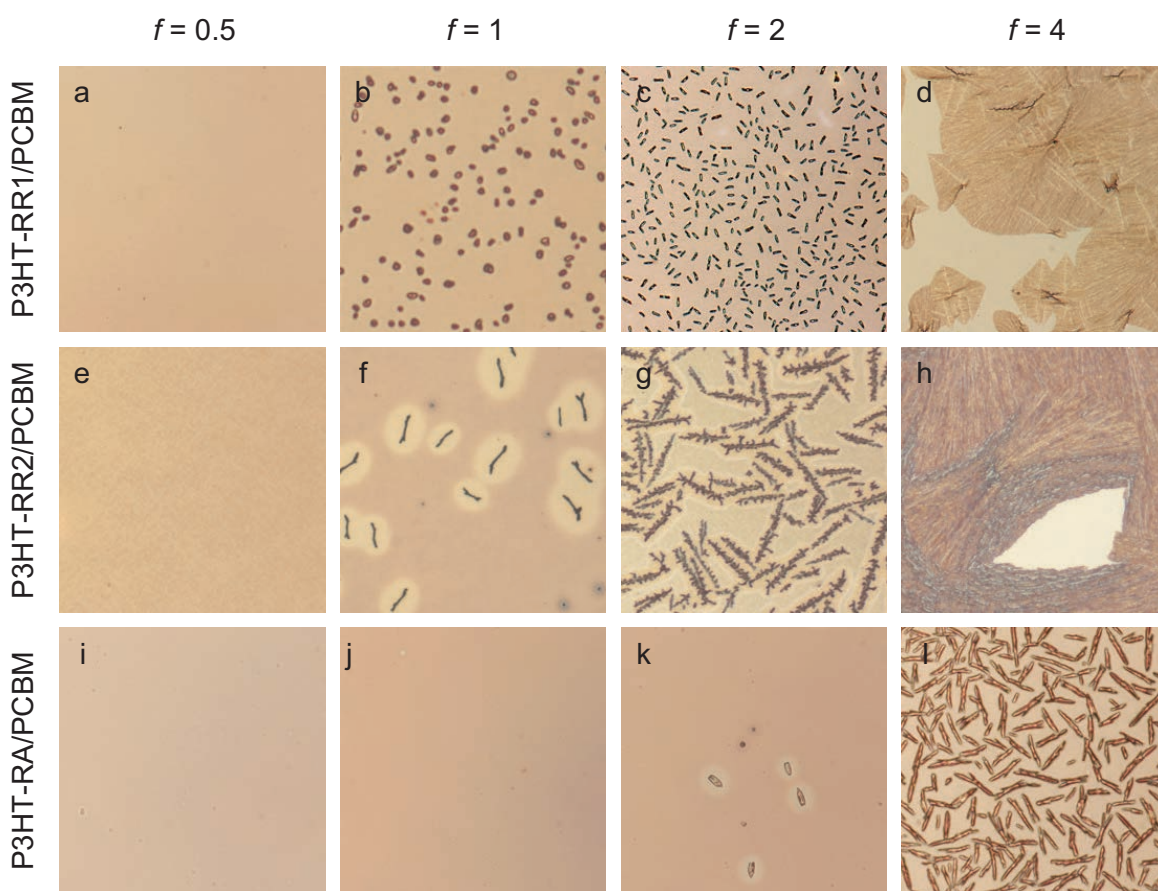


Figure 4.2 Optical microscopy images of (a-d) P3HT-RR1/PCBM, (e-h) P3HT-RR2/PCBM, and (i-l) P3HT-RA/PCBM films. The PCBM to polymer weight fraction was varied from $f = 0.5$ to $f = 4$. Image size = $500 \times 500 \mu\text{m}^2$.

RA is amorphous. P3HT-RR1 and -RR2/PCBM systems show similar morphology with irregular domains attributed to the formation of PCBM aggregates at mixing ratios f from 1 to 4. With PCBM mixing ratios $f < 1$, the films are homogeneous on the micrometer length scale, whereas large PCBM aggregates are observed at $f \geq 1$. The PCBM aggregates have a greater average length and broader length distribution for $f = 2$ compared to $f = 1$, and develop to numerous 'fans' for $f = 4$. On the other hand, PCBM aggregates appear in P3HT-RA/PCBM blends at double the PCBM loading ($f = 2$) compared to the semi-crystalline P3HT-RR1 and -RR2. The composition series of P3HT-RA (Figure 4.2 i-l) clearly indicates a partial miscibility of P3HT and PCBM, with an approximate solubility limit of 2 for PCBM in amorphous P3HT. With a typical crystal volume fraction of 50%-70% in semicrystalline P3HT, the PCBM solubility in these materials (P3HT-RR1 and -RR2) is reduced by a factor of ~ 2 .

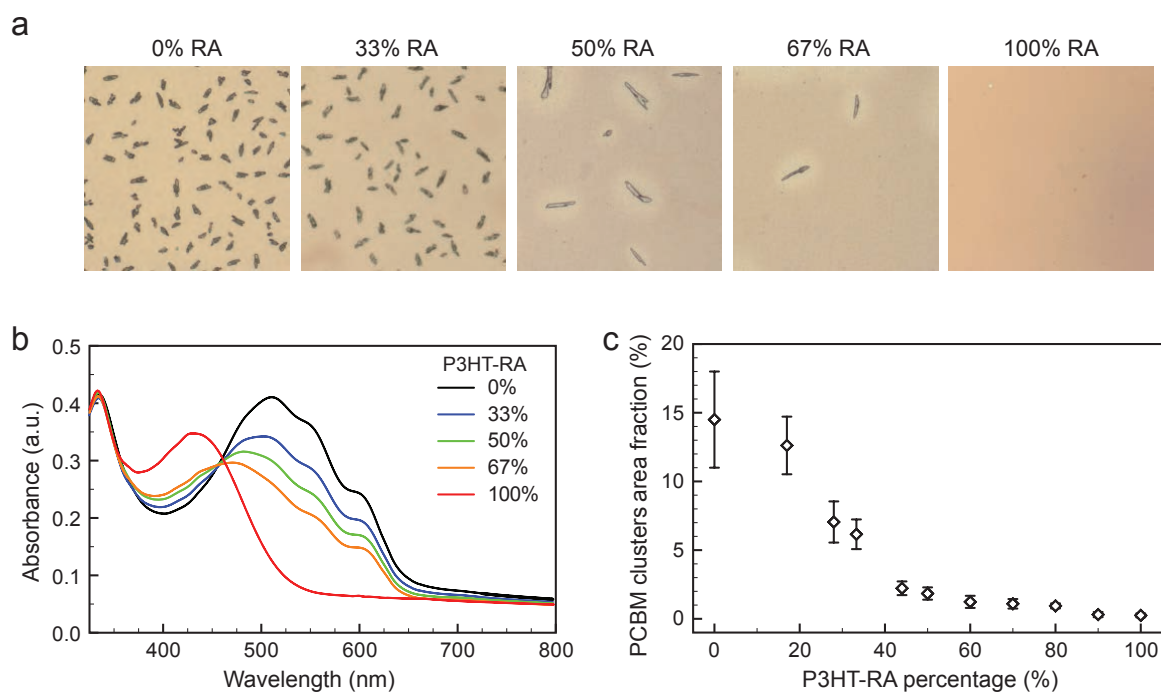


Figure 4.3 a) Optical microscopy images of P3HT/PCBM thin films ($f = 1$, Image size = $250 \times 250 \mu\text{m}^2$). b) UV/Vis spectra and c) Area fraction of PCBM aggregates as a function of weight percentage of P3HT-RA in the P3HT-RR1/RA mixtures. All films were annealed for 2 hrs at 175°C .

We have further used ternary blends of P3HT-RR1:RA/PCBM to investigate the dependence of PCBM solubility on P3HT crystallinity. The mixing ratios between P3HT-RR1 and -RA were varied, while the PCBM concentration was fixed to $f=1$ with respect to total P3HT. Figure 4.3 shows PCBM clusters for films with varying P3HT-RR1:RA. We find that for P3HT-RA higher than 50%, few or no PCBM clusters are observed, while below this value, the area fraction of PCBM clusters increases significantly. The continuous variation of P3HT-RR1:RA from pure P3HT-RR1 to pure P3HT-RA shows a reduction in area fraction of PCBM aggregates, indicating an increase in PCBM miscibility. The enhanced and red shifted UV-Vis absorbance spectra (Figure 4.3b) implies that the overall P3HT crystallinity increases with decreasing percentage of P3HT-RA. Comparing the UV-Vis absorbance with the area fraction of PCBM clusters (Figure 4.3c), these results confirm the PCBM miscibility dependence on overall P3HT crystallinity, which suggests that the structure formation in the system may be driven by P3HT crystallization.

The PCBM aggregates in Figure 4.2 and Figure 4.3 have elongated and in some case branched morphologies, which suggests PCBM crystallization. It is most likely that the

formation of PCBM clusters is determined by a combination of P3HT crystallization and the solubility limit of PCBM in amorphous P3HT. However, a quantitative solubility limit is difficult to deduce from the above macroscopic study, and in the following section we use X-ray scattering techniques to make more accurate estimations of the PCBM solubility in the P3HT/PCBM system.

4.3.2 UV-Vis Measurements of P3HT/PCBM

In order to perform a well defined study of the interplay between crystallization and demixing, the blend film was first heated above the melting point and then cooled at a slow rate. This enables crystallization from a homogeneously mixed blend. The crystallization of P3HT/PCBM blends upon cooling from the amorphous phase at high temperatures was detected by UV-Vis spectroscopy. Films with PCBM weight ratios f between 0 and 2 were cast onto quartz substrates. Upon heating to 240 °C, the characteristic vibronic UV-Vis peak structure is lost, indicating that this temperature lies above the P3HT melting point for all samples. The spectra of as-cast films cooled from 240 °C to 40 °C are shown in Fig. 4.4. An isosbestic point was found at ~ 400 nm for all samples.

To confirm the existence of an isosbestic point, the spectra were integrated in wavelength ranges in which the signal is dominated by PCBM or P3HT absorption, respectively. For this analysis the P3HT/PCBM mixing ratio is calculated in terms of the PCBM volume fraction $\phi = (1 + \Delta\rho/f)^{-1}$, with $\Delta\rho$ the PCBM:P3HT density ratio ($\Delta\rho \approx 1.13$ using $\rho_{\text{PCBM}} = 1.3 \text{ g/cm}^3$, $\rho_{\text{P3HT}} = 1.15 \text{ g/cm}^3$).¹⁰¹ The PCBM intensity was normalized at $\phi = 0.3$.

$$I_{\text{PCBM}}(\phi) = 0.30 \frac{\int_{\lambda_1}^{\lambda_2} d\lambda [I(\lambda, \phi) - (1 - \phi) \cdot I(\lambda, 0)]}{\int_{\lambda_1}^{\lambda_2} d\lambda [I(\lambda, 0.30) - (1 - 0.30) \cdot I(\lambda, 0)]} \quad (4.1)$$

for PCBM with $\lambda_1 = 260$ nm and $\lambda_2 = 335$ nm and

$$I_{\text{P3HT}}(\phi) = \frac{\int_{\lambda_1}^{\lambda_2} d\lambda I(\lambda, \phi)}{\int_{\lambda_1}^{\lambda_2} d\lambda I(\lambda, 0)} \quad (4.2)$$

for P3HT (normalized at $\phi = 0$) with $\lambda_1 = 500$ nm and $\lambda_2 = 625$ nm.

The fact that all data points lie on straight lines in Fig. 4.4b and d which intersect at $\phi = 0.5$ indicates that the signals stemming from the P3HT and PCBM spectral regions are additive

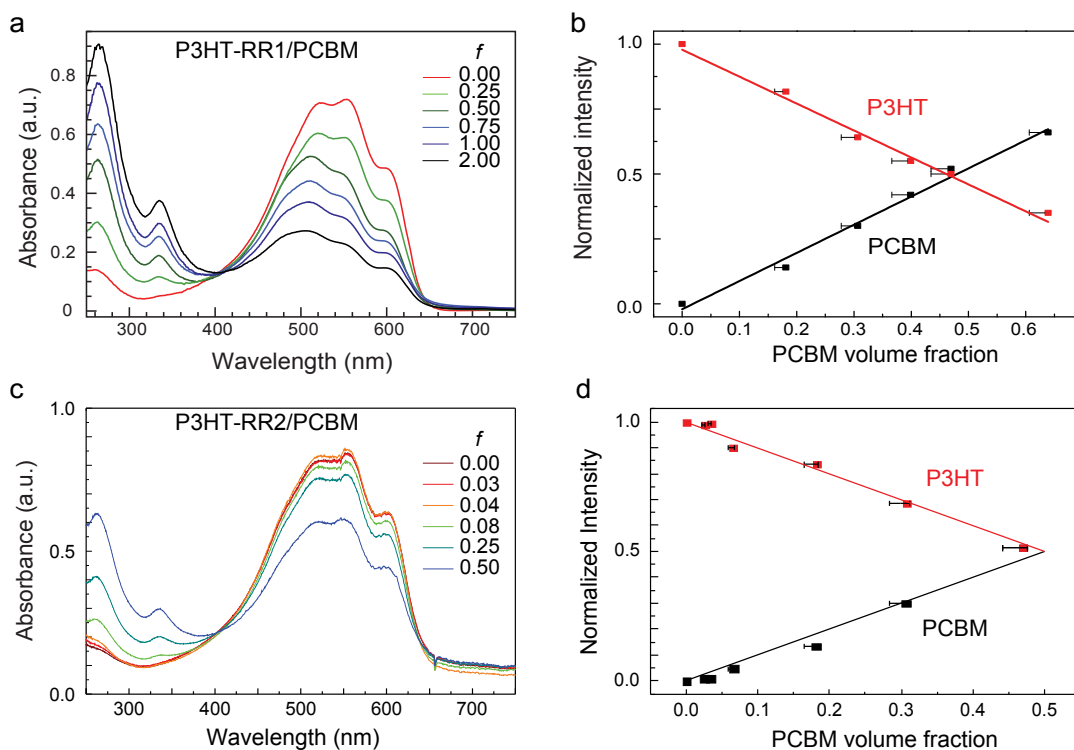


Figure 4.4 UV-Vis spectra of a) P3HT-RR1/PCBM and c) P3HT-RR2/PCBM films as a function of PCBM weight fraction f . Films were melted at 240 °C followed by cooling to 40 °C. b) and d) Corresponding integrated intensities versus PCBM volume fraction from a) and c) respectively. The error bars correspond to uncertainties in $\Delta\rho$ which arise from different published values of the PCBM density.^{101,102}

and proportional to their volume fractions, thus leading to an isosbestic point in the UV-Vis spectra. This is a clear indication that, in terms of their spectral response, they consist of separate crystalline P3HT and amorphous P3HT/PCBM phases. Since crystalline and amorphous P3HT have very different absorption properties an isosbestic point is only expected if the ratio of ordered to disordered P3HT does not change dramatically upon PCBM addition. This observation is therefore further evidence that the addition of PCBM does not strongly influence P3HT crystallinity, i.e. the addition of PCBM neither substantially hinders nor enhances P3HT crystallinity although crystallization temperatures may shift slightly.

4.3.3 SAXS and WAXS of Bulk P3HT/PCBM

The macroscopic studies show partial miscibility of P3HT with PCBM, but in order to understand the microscopic distribution and conformation of these two materials, X-ray scattering measurements were performed on bulk P3HT/PCBM mixtures. Here, the well defined

P3HT-RR2 was used as the model material. The microstructure of regioregular P3HT crystal is schematically illustrated in Figure 4.5a. P3HT forms lamellar crystals driven by π - π stacking of thiophene rings and additional alignment of alkane chains leading to side-chain crystallization. Lamellar crystalline layers are separated by amorphous layers and form a superstructure with periodicity $L_p = d_c + d_a$ (d_c and d_a : thickness of the crystalline lamellae and amorphous layers, respectively). The thiophene backbone and hexyl side chains of P3HT stack alternately along the b -axis, and the π - π stacking of the planarized backbone is along the b -axis. Figure 4.5b shows a combined SAXS and WAXS signals for the studied P3HT-RR2. The superstructure of alternating lamellar and amorphous layers give rise to a SAXS signal (L_p reflection), resulting from the electron density difference between these two regions, while the crystal lattice of P3HT can be resolved by WAXS.

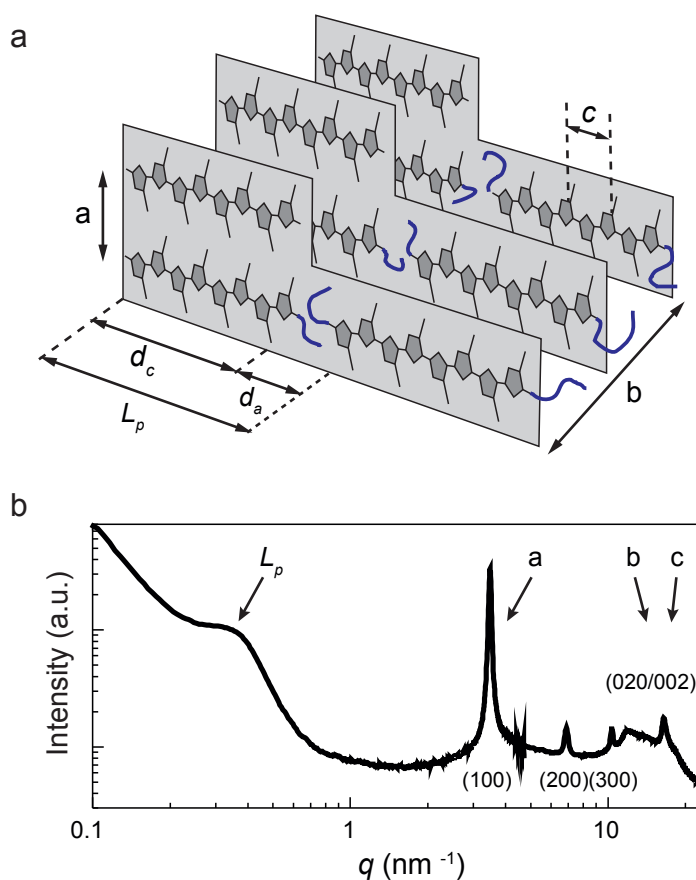


Figure 4.5 (a) Schematic illustration of the semi-crystalline structure of P3HT: a , b , and c represent the crystal lattice constants; $L_p = d_c + d_a$ is the long period. (b) Combined SAXS and WAXS patterns of P3HT-RR2.

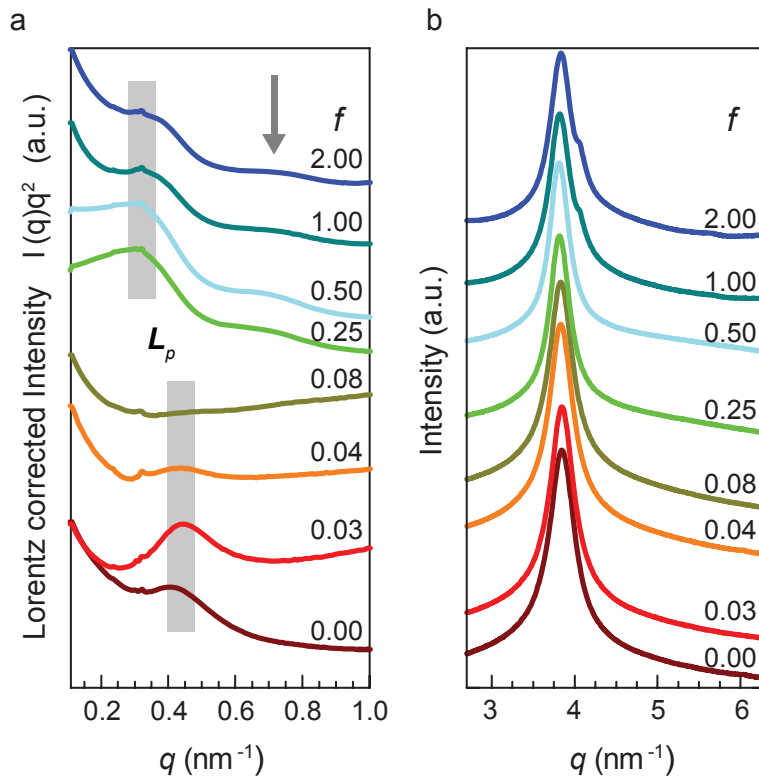


Figure 4.6 Bulk SAXS of P3HT-RR2/PCBM blend. a) Lorentz corrected SAXS patterns. The scattering vector q is constant for the L_p peak with decrease in intensity with increasing PCBM mixing ratio from $f = 0.00$ to $f = 0.08$. The L_p peak shifted to smaller q at higher PCBM concentrations and remained constant from $f = 0.25$ to $f = 2.00$. b) The (100)-P3HT peak does not shift with increasing PCBM concentrations.

PCBM was added to P3HT-RR2 at different weight fractions ($f = 0 - f = 2$). We specifically investigated the system from very low concentrations of PCBM, which represent a small perturbation to P3HT crystallization, so as to get information on the solubility of PCBM in semi-crystalline P3HT. Moreover, samples were heated above the melting temperature followed by slow cooling in order to remove the non-equilibrium characteristics present from spin coating. Bulk SAXS patterns of the melt annealed blend are given in Figure 4.6. Pure P3HT-RR2 shows a long period of $L_p = 14.8$ nm, as indicated by the SAXS signal at $q = 0.425$ nm⁻¹, which is close to the mean contour length of P3HT chains of 16.3 nm. With increasing PCBM concentration, the peak position remains constant but its intensity decreases and eventually disappears at $f = 0.08$. Meanwhile, in contrast to the change in L_p , the (100)-P3HT peak in Figure 4.6b remains unaltered upon increasing PCBM. Therefore, the disappearance of the peak in Figure 4.6a is not due to a decrease in crystallinity with increasing PCBM concentration.

It is known that PCBM has higher electron density compared to P3HT, so the electron density contrast between crystalline and amorphous layers is reduced by the dissolution of PCBM in the amorphous P3HT layers. The absence of a diffuse scattering peak in WAXS (Figure 4.7) for $f = 0.08$ suggests that the PCBM molecules are well dissolved in the amorphous P3HT layers.

Using the melting enthalpy of fully crystalline P3HT, $\Delta H_m^\infty = 37 \text{ J/g}$,¹⁰³ and measured melting enthalpy for P3HT-RR2, 24 J/g , results in a crystallinity of $\phi_c = 65\%$. Thus, an overall PCBM concentration of 8 wt% corresponds to a PCBM concentration of 23 wt% within the amorphous interlayer of semi-crystalline P3HT, where PCBM is fully miscible with amorphous P3HT.

Increasing PCBM concentration to $f = 0.25$, the L_p peak reappears and shifts to a lower q value. The peak position was approximately independent of PCBM content and corresponds to $L_p \approx 17\text{-}18 \text{ nm}$. The swelling of the P3HT amorphous layer by PCBM gives a 2-3 nm increase in the layer thickness, and the reappearance of the scattering peak is attributed to the increase in electron density with further uptake of PCBM into the amorphous layer. The constant values for L_p for $f \geq 0.25$ suggest that the solubility limit of PCBM in the amorphous layer was reached below $f = 0.25$.

The WAXS patterns of P3HT-RR2/PCBM blends, shown in Figure 4.7, remain unaltered in the low concentration range of $f \leq 0.08$. For higher PCBM concentrations at $f = 0.25$ and $f = 0.5$, the appearance of diffuse scattering can be observed in the $12\text{-}15 \text{ nm}^{-1}$ and $19.5\text{-}21.5 \text{ nm}^{-1}$ q range (gray region), indicating PCBM aggregation. For $f = 1$ and $f = 2$, the crystalline Bragg-peaks of PCBM crystals are visible. It is evident that for the higher PCBM concentrations of $f \geq 0.25$, a large amount of PCBM has been rejected from the amorphous P3HT layers, as the L_p values are constant.

In this section, we have demonstrated that the bulk P3HT/PCBM blend morphology was determined by P3HT crystallization forming lamellar structures with alternating crystalline P3HT and amorphous P3HT/PCBM interlayers. PCBM addition above the solubility limit does not result in a further change in the meso-morphology but causes PCBM segregation.

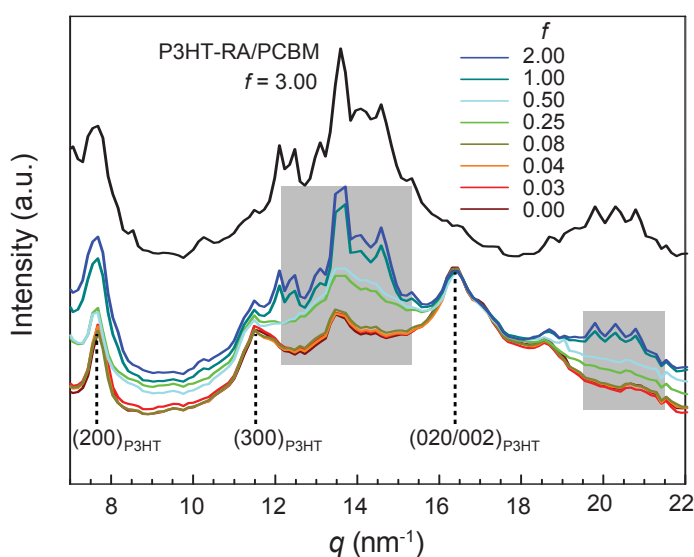


Figure 4.7 Bulk WAXS patterns of P3HT-RR2/PCBM blends normalized to the (020/002)-P3HT peak. The patterns are invariant for PCBM concentrations of $f = 0.00$ to $f = 0.08$. At higher concentrations, additional broad maxima corresponding to PCBM aggregation become visible (grey regions). The WAXS pattern of P3HT-RA/PCBM is given for the high PCBM concentration of $f = 3$ (black line, offset for clarity).

4.3.4 GISAXS and GIWAXS of P3HT/PCBM Thin Films

While bulk X-ray scattering is advantageous for structure verification, it is more of interest to study the thin film behavior as it is more relevant to photovoltaic devices. GISAXS and GIWAXS measurements were performed on thin films of P3HT-RR2/PCBM with thicknesses of ~ 100 nm. Similar to previous bulk samples, thin films were heated above the P3HT-RR2 melting point followed by slow cooling to room temperature. The GISAXS and GIWAXS patterns are shown in Figure 4.8. The GISAXS results clearly show lateral signals corresponding to $L_p \approx 17$ nm, which is consistent with the values found in bulk samples at the same concentrations. A comparison of the long period obtained from SAXS and GISAXS is given in Table 4.1. The 1D GISAXS intensity profiles in Figure 4.8b show the re-appearance of the L_p peak at $f = 0.185$. Using the previous assumption of $\phi_c = 65\%$ crystallinity in P3HT-RR2, a ratio of $f = 0.185$ gives a PCBM concentration of ~ 52 wt% in the amorphous P3HT region.

GIWAXS patterns in Figure 4.8c show similar results to the bulk WAXS. For PCBM concentrations of $f = 0.25$ and $f = 0.50$, a diffuse scattering ring can be discerned in the range of $q \approx 15$ nm $^{-1}$ corresponding to the aggregation of PCBM, and for $f = 2.00$, bright spots

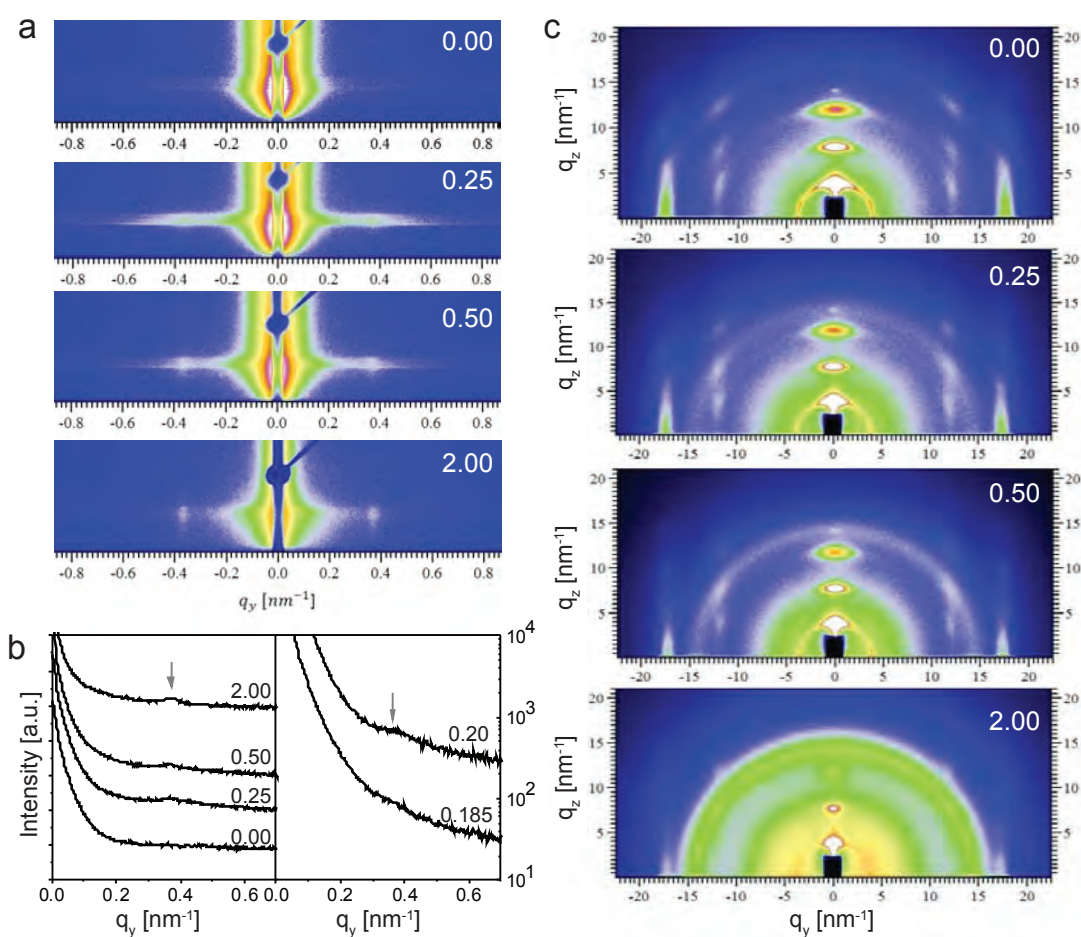


Figure 4.8 a) GISAXS patterns of P3HT-RR2/PCBM blend with increasing PCBM concentrations from $f = 0.00$ to $f = 2.00$, showing the peak corresponding to long period L_p . b) The corresponding 1D GISAXS intensity profiles along q_y for increasing PCBM concentrations. The curves are vertically shifted for clarity. (c) GIWAXS patterns of the P3HT-RR2/PCBM blend. A diffuse scattering ring is visible at $q \approx 15 \text{ nm}^{-1}$ for $f = 0.25$ and $f = 0.50$. For $f = 2.00$, bright spots are visible, indicating the presence of PCBM crystals.

are visible which indicates PCBM crystallization. The sample series all show P3HT ($h00$) reflections along q_z , which indicate a predominant perpendicular alignment of the a -axis with respect to the substrate. The edge-on orientation of P3HT on the substrate is not influenced by the addition of PCBM over the concentration range. The overall findings from the X-ray scattering experiments indicate that the crystallization of P3HT is the driving force for phase separation in blend of P3HT and PCBM. The results are consistent with the previous optical microscopy experiments.

The GISAXS and GIWAXS results are consistent with previous bulk measurements, showing that P3HT crystallization expels PCBM into the amorphous interlayers. A maximum

Table 4.1 Comparison of L_p values obtained from bulk SAXS and film GISAXS.

	$f = 0.00$	$f = 0.04$	$f = 0.08$	$f = 0.25$	$f = 0.50$	$f = 1.00$	$f = 2.00$
SAXS	14.8	14.2	14.6	18.0	17.8	17.2	17.6
GISAXS	N/A	N/A	N/A	17.0	17.5	17.2	17.2

incorporation of 52 wt% of PCBM within amorphous P3HT was detected. In addition, these results further confirm that the edge-on orientation of P3HT crystals in thin films is maintained in the presence of PCBM.

The studies of macroscopic morphologies and X-ray scattering show that P3HT and PCBM are miscible over a wide range of concentrations. Optical microscopy images of P3HT/PCBM films after thermal annealing show a solubility limit of PCBM in amorphous P3HT for a weight ratio of about $f = 2$, while for regioregular P3HT it is at around $f = 1$. The decrease in PCBM solubility is in qualitative agreement with the fact that crystallinity in semi-crystalline polymers is typically in the range of 50%-70%. The existence of an isosbestic point in the UV-Vis spectra is further evidence that the addition of PCBM does not interfere with the P3HT crystal formation, and PCBM is mixed in the amorphous phase. The shift in the long period peak for PCBM concentrations between $f = 0.08$ and $f = 0.185$ suggests a maximal PCBM concentration between 20 wt% and 52 wt% within the amorphous phase. A more quantitative analysis is limited by the lack of knowledge of the actual fraction of P3HT crystallinity.

It is worth noting that the optimized P3HT/PCBM device has a composition ratio of $f = 1$, which is close to the solubility limit of PCBM in regioregular P3HT. With PCBM weight fractions above this limit, micron-sized PCBM aggregates were observed which is unfavorable for photovoltaic device operation. The scattering peak originating from the lamellar crystal of P3HT is consistently observed over the concentration range of PCBM from $f = 0$ to $f = 4$. The lack of a further SAXS signal in P3HT/PCBM blends rules out the formation of a 10-nm spinodal morphology.

The results allow to construct a picture of the structure formation process in this photovoltaic blend. Structure formation in P3HT/PCBM blends is initiated by P3HT crystallization, which is invariant to the presence of PCBM regarding the amorphous-crystalline superstructure, the crystallinity of P3HT and orientation. PCBM is firstly mixed into the interlamellar

layer until it reaches its solubility limit. Excess PCBM is expelled from the P3HT lamellar structure, presumably to the interspherulitic grain boundaries, into macroscopic PCBM aggregates, and to the interfaces of these films.

4.4 Conclusion

In this chapter, we have demonstrated that structure formation in P3HT/PCBM blends is initiated by the crystallization of P3HT, segregating PCBM to the amorphous P3HT phase. The crystallization-induced structure formation is beneficial for photovoltaic device operation in that the lamellar crystal has an intrinsic size at the 10-nm length scale. It therefore provides a feature size that is required for exciton dissociation.

While PCBM aggregation and crystallization could facilitate electron transport, the present study can not determine where the PCBM aggregation takes place. It may occur in the interlamellar amorphous layer, or at the interspherulitic grain boundaries. It is therefore proposed that a hierarchical PCBM structure is formed in the blend connecting the 10-nm lamellae to the inter-spherulitic network. In combination to the edge-on orientation of P3HT crystals, this self-assembly morphology closely approximates the optimal BHJ. It should be noted that P3HT/PCBM films in optimal devices usually have a deeply quenched morphology due to rapid solvent evaporation, while in this study they are melted to remove the non-equilibrium structures. To verify this structure formation mechanism in P3HT/PCBM blends, device studies were carried out, as reported in Chapter 5. Furthermore, polymer/polymer blends of P3HT/F8TBT are investigated in Chapter 6 to generalize the conclusion we find in the P3HT/PCBM system.

Chapter 5 Spherulitic Crystallization of P3HT/PCBM and Its Effect on Device Performance

In this chapter, P3HT with a spherulitic superstructure was produced from P3HT/PCBM blends by controlled solvent vapor annealing. The spherulitic arrangement of P3HT gives rise to its improved molecular order and the P3HT/PCBM devices exhibit good photovoltaic performance. These results confirm that the structure formation in P3HT/PCBM blends is driven by the crystallization of P3HT that constructs a nanostructure beneficial for device operation.

5.1 Introduction

Bulk heterojunction solar cells based on polymer/fullerene systems have led to great progress in their photovoltaic device performance with improving understanding of its morphology organization.^{104,105} The device efficiency of P3HT/PCBM blends is now approaching 5% at optimized processing conditions.¹⁰⁶

BHJ active layers are mostly produced by spin coating, thus films are usually frozen in a non equilibrium state due to the rapid quenching from solutions. The morphology is determined by the interplay between the thermodynamics of the blends and the kinetics of the film formation.^{107,108} Efforts for improving P3HT/PCBM photovoltaic performance have focused on the optimization of preparation conditions, including controlling the rate of solvent evaporation during film formation,⁹⁸ adding additives,^{109–114} adjusting the volume

fractions of P3HT/PCBM and applying thermal^{86,99,115} or solvent annealing.^{100,116,117} These approaches have been proven to improve the crystallinity of P3HT and the level of phase separation between donor and acceptor materials so as to improve device performance. The previous chapter showed that crystallization of P3HT into lamellae forms a nanostructure on the length scale close to the optimal BHJ morphology.

P3HT/PCBM device performance is strongly influenced by the 10-nm-length-scale nano-morphology because exciton dissociation, recombination and charge transport are all affected by the size and purity of each phase, the nature of the interface and molecular packing.¹¹⁸ The molecular order in the donor and acceptor domains is the key factor for efficient charge transport. The crystalline lamellae provide charge transport through intra-chain and inter-chain π - π stacking, whereas the charge carrier mobility is found to drop significantly when passing from the crystalline phase to the isotropic amorphous phase.

P3HT thin films usually show low crystallinity with a high degree of local defects. The large number of grain boundaries tend to reduce charge mobility.^{63,119} Although theoretical calculations suggest that intra-chain charge transport is significantly faster than between π - π stacking (by 2-3 orders), the presence of disordered interlamellar regions containing chain folds and ends inevitably reduces the transport rate.¹²⁰ Thus, a variety of approaches have been developed to control P3HT crystallization. Apart from thermal and solvent annealing, new approaches include the assembly of P3HT nanowires,¹²¹ epitaxial crystallization,^{70,122} and mechanical rubbing.^{123,124}

As an alternative, a method based on controlled solvent swelling and de-swelling allows control of the nucleation density and produces micron scale spherulitic structures of P3HT.^{125,126} Crystallization of P3HT is commonly observed to form stacks of lamellae and give rise to spherulites if the nucleation density is small enough. The structure of spherulites consists of a radical assembly of crystalline lamellae and amorphous layers, which shows well-defined local packing as well as long range ordering. There are two types of grain boundaries: 1) the amorphous phase between crystalline lamellae on the nanometer length scale and 2) the mesoscopic barriers between spherulites or lamellar stacks nucleated from different sites.¹²⁷ The spherulitic morphology of P3HT provides a good platform to study the effect of its crystallization on electronic performance.

In the previous chapter, we studied the structure evolution in P3HT/PCBM blends. It is proposed that the structure in P3HT/PCBM blends is defined by the P3HT crystallization and the rejection of PCBM from P3HT lamellae. Herein we used the solvent swelling and de-swelling method to structure spherulitic P3HT in P3HT/PCBM blends by controlling the nucleation density. Devices were fabricated based on films with well-defined P3HT spherulitic superstructure and photovoltaic performance was found to be comparable to that of optimized devices. These results confirm that a bulk heterojunction morphology is constructed by the crystallization of P3HT and segregation of PCBM, which is beneficial for electronic device applications.

5.2 Experimental Methods

Only one batch of P3HT, namely P3HT-RR1, was used, so we refer to it here simply as P3HT. P3HT/PCBM solutions in chlorobenzene (36 mg/mL) were prepared by dissolution at 75 °C with a weight ratio of $m_{\text{P3HT}} : m_{\text{PCBM}} = 5 : 4$ in a glovebox. P3HT/PCBM films were spin coated at 3000 rpm onto either PEDOT:PSS-coated or ZnO coated ITO substrates. This produced 80 nm thick films as determined by a Dektak profilometer. The films with spherulitic morphology were prepared by exposing the as spun films to a controlled vapor pressure of a good solvent, carbon disulfide (CS_2), using the solvent vapor annealing (SVA) setup as shown in the Experimental Techniques. Devices were fabricated with the standard structure of ITO | PEDOT:PSS | P3HT/PCBM | Al, and the inverted structure of ITO | ZnO | P3HT/PCBM | MoO_3 | Ag.

5.3 Results and Discussion

5.3.1 Spherulitic Crystallization of P3HT/PCBM

Solvent annealing enhances chain mobility in crystalline polymers at room temperature. This is often used for improving the self-organization of conjugated polymers and the performance of their electronic devices.⁷⁵ SVA has recently been used for P3HT to control its nucleation density and microscale spheruliticities of P3HT were obtained in thin films.¹²⁶ Here we extend this approach to P3HT/PCBM ($f = 1$) blends. CS_2 is chosen because of its abil-

ity to dissolve crystalline P3HT in its vapor phase, which is not possible with other good solvents for P3HT, such as chloroform and chlorobenzene. It is also important that the solvent should have similar interactions with P3HT and PCBM, otherwise the solubility difference could lead to segregation of the less soluble component. The swelling behavior of P3HT and PCBM was investigated and results confirmed their similar solubility in CS₂.¹²⁸

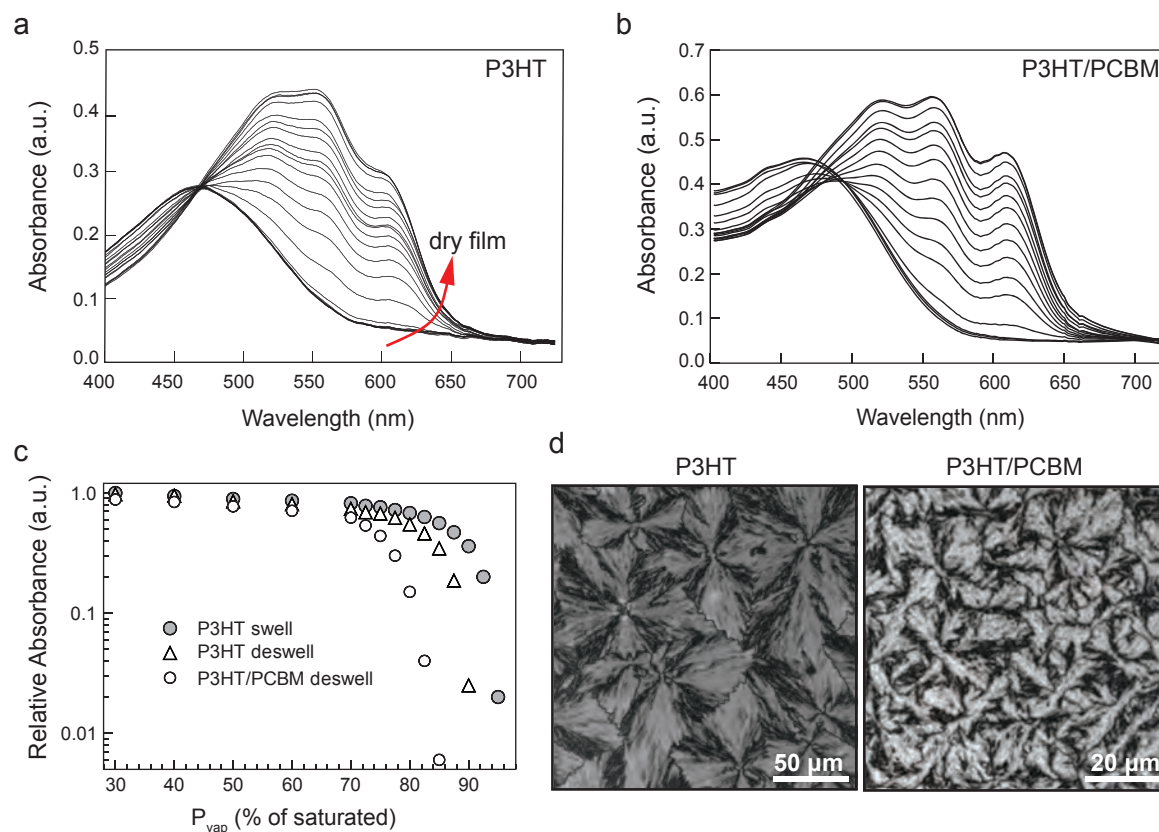


Figure 5.1 UV-Vis spectra of a) P3HT and b) P3HT/PCBM films deswell in the controlled CS₂ solvent vapor P_{vap} from 95% to 0% at 0.5% min⁻¹. c) The crystalline phase absorption at 610 nm relative to the initial dry film during de-swelling. d) POM images of P3HT and P3HT/PCBM films recrystallize for 30 min by controlled CS₂ vapor annealing.

In situ UV-Vis absorbance spectroscopy was used to trace the dissolution and recrystallization of P3HT, as shown in Figure 5.1. Pure P3HT and P3HT /PCBM ($f = 1$) blends were exposed to atmospheres in which the CS₂ partial vapor pressure (P_{vap}) was varied between 0% and 100%. The initial dry film is dominated by P3HT aggregation absorption at 555 nm and 610 nm (Figure 5.1a). The intensity of these peaks diminishes and an absorption peak at 453 nm grows correspondingly as the P_{vap} increases. Above P_{vap} of 95%, the vibronic absorption intensity at 610 nm is undetectable and P3HT crystals have fully dissolved in

the solvent-swollen film. This behavior is mirrored by the UV-Vis absorption spectra of the P3HT/PCBM blend in Figure 5.1b. Starting from a fully dissolved film, P_{vap} was lowered at $0.5\% \text{ min}^{-1}$ and the 610 nm peak intensity was monitored to detect the onset of P3HT crystallization.

Upon lowering P_{vap} , the film gradually dries with increasing polymer concentration until a critical super saturation reaches, which subsequently induces nucleation of P3HT. The pure P3HT film and the P3HT/PCBM film showed considerable dissolution-recrystallization hysteresis which is common for crystal forming systems, with P3HT crystallinity reappearing at a vapor pressure of 90% in the pure P3HT film, and 82.5% in the blend film, as shown in Figure 5.1c. There is a noticeable hysteresis in the onset of the 610 nm peak since a significant undercooling is needed for the nucleation and growth of the crystalline phase.

The well-control annealing afforded by varying P_{vap} allows P3HT to crystallize into spherulitic morphology. Figure 5.1d shows the polarized optical microscopy (POM) images of the resulting films, where starting from 95%, the CS_2 P_{vap} was lowered to 85% and 82% for the P3HT and P3HT/PCBM films respectively. When viewed between crossed polarizers, both films show the characteristic Maltese-cross pattern of polymer spherulites, with spherulite sizes of several tens of micrometers. However, such P3HT/PCBM spherulitic films de-wet from the ITO substrate due to the low viscosity at extensive swelling, thus we did not manage to fabricate photovoltaic devices with blend films of large spherulites. We decreased the dissolution P_{vap} and films were obtained with good integrity but higher nucleation density (Figure 5.2).

The results of the controlled P3HT crystallization experiments confirm the PCBM miscibility in amorphous P3HT. When crystallized from swollen amorphous blends, P3HT spherulite formation evolves very similarly in both pure and blend films, clearly showing that PCBM segregation in the blends does not interfere with P3HT crystal formation. Indeed, the fact that P3HT crystallization sets in at deeper super-cooling P_{vap} compared to the pure P3HT film is indicative of the good P3HT/PCBM miscibility. Rather than acting as a nucleation agent which is typical for an immiscible contaminant, PCBM dilutes the P3HT chains in the amorphous blend, requiring a deeper quench to induce nucleation of P3HT.

5.3.2 Morphology Characterization of P3HT/PCBM

In order to test the photovoltaic performance of spherulitic P3HT/PCBM active layers, we compare it with optimized thermal annealing (TA) as well as as spun films. The surface morphology of P3HT/PCBM active layers after SVA and TA were examined by OM, SEM and AFM, as shown in Figure 5.2. The SVA films show polymer spherulitic morphology as evident by the Maltese-cross pattern in POM image, while the TA film is optically isotropic. Both films were exposed to oxygen plasma for 30 s to enhance the contrast for SEM imaging. Polymer chains can be attacked by energetic atomic oxygen through different mechanisms, and chain scissions can occur, eventually leading to volatile products. Film thickness decreased from 80 nm to 50 nm due to this degradation. The TA film displays some irregular wormlike patterns in Figure 5.2a. In comparison, the SVA film exhibits a highly ordered nanostructure similar to a crystalline lamellar morphology. The preferential etching of the amorphous phase by an oxygen plasma¹²⁹ allows to reveal the semicrystalline structure of P3HT.

The difference in the surface texture between TA and SVA films arises from their different crystalline morphology. Spin coated P3HT/PCBM films have a large number of stacking defects. Although the crystallinity of P3HT increases significantly after TA, the size of P3HT crystals is relatively small due to the high nucleation density. In the SVA case, however, the nucleation density is well controlled such that the P3HT grows into micron-size spherulites. It is most likely that the lamellar-like structure shown in Figure 5.2b reflects the long-range order of crystalline lamellae in P3HT spherulites. Figure 5.2c and d compare the AFM height images of P3HT/PCBM films. The surface roughness was measured from topography images of $5\ \mu\text{m} \times 5\ \mu\text{m}$ regions from each film. The TA film surface appears smooth with a low roughness of 1.5 nm, but the SVA film shows a much higher roughness of 5.0 nm.

Figure 5.3 shows the UV-Vis and PL spectra for the P3HT/PCBM series with different treatments for photovoltaic devices. The as spun refers to samples measured right after spin-coating onto PEDOT:PSS layers with no further treatment. In comparison to the as spun film, TA and SVA films show enhanced absorption intensity and the absorption maximum is red-shifted. P3HT characteristic peaks are clearly observed at 500 nm with shoulders at 550 nm and 610 nm. The red-shift of peak position is attributed to an increase of conjugation

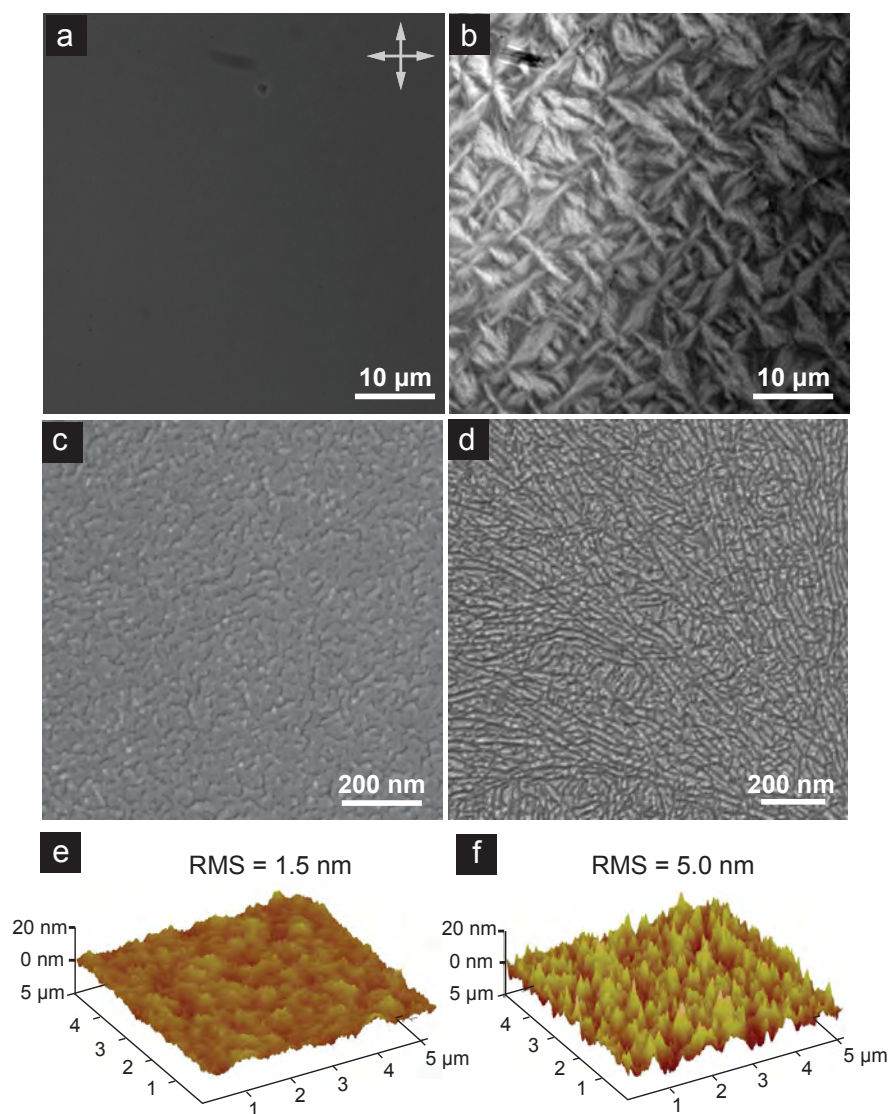


Figure 5.2 POM, SEM and AFM images of P3HT/PCBM with (a, c, e) TA and (b, d, f) SVA treatments.

length and more delocalized excitons. The intensities of the 0-0 transition (610 nm) and 0-1 transition (550 nm) are higher in the SVA film than in the TA film, suggesting that P3HT in spherulitic films has a longer conjugation length and better molecular order.

Figure 5.3b shows the PL intensity of P3HT/PCBM films increases after TA and SVA. The degree of PL quenching is a measure for the efficiency of charge separation in BHJ blends. The as spun film shows significant PL quenching due to the nanoscale mixing of P3HT with PCBM such that excitons dissociate efficiently at the interface between P3HT and fullerene. If the P3HT/PCBM mixture becomes more segregated or phase purity is improved, a rise in the PL is expected because of a reduced interfacial area and less efficient charge transfer

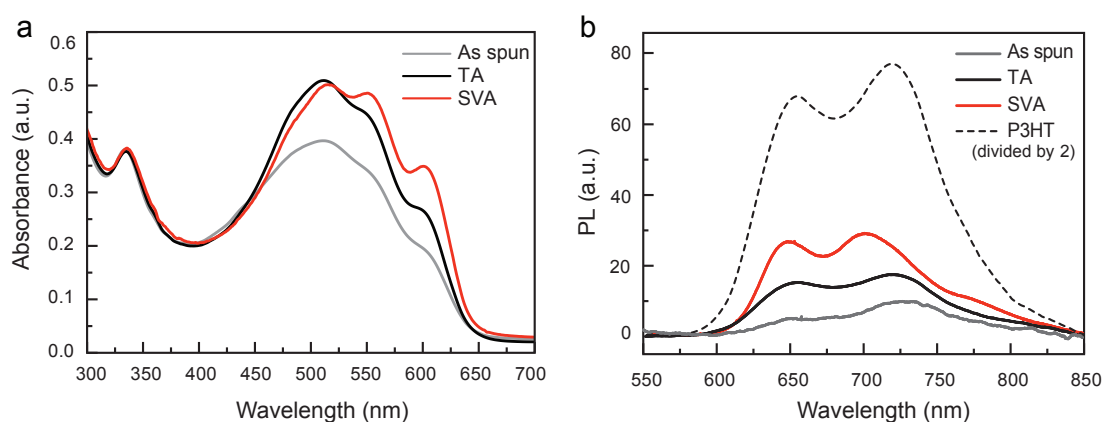


Figure 5.3 a) UV-Vis and b) PL spectra with 470 nm excitation for P3HT/PCBM films with different annealing protocols.

between P3HT and PCBM. Therefore, the TA film (black line) shows increased PL yield compared to the as spun film (grey line), and the SVA film (red line) exhibits a significantly higher PL intensity due to coarsening of P3HT and PCBM domains introduced by the slow solvent drying process.

5.3.3 Device Characterization of Standard P3HT/PCBM Solar Cells

Figure 5.4 presents the device characteristics of P3HT/PCBM blends made using different annealing protocols. All devices were prepared on PEDOT:PSS-coated ITO substrates with Al as cathode (Figure 5.4a inset). The P3HT/PCBM active layer has a film thickness of 80 nm and weight ratio of 5:4. The TA device was made using the optimized processing parameters according to the literature, which was used as reference for the study. Devices were fabricated with as spun, TA, SVA, and SVA+TA preparation conditions. The sample prepared via TA was annealed after the deposition of the Al cathode. The sample prepared via SVA had the active layer treated with SVA after spin coating but before deposition of the Al cathode. This is because the SVA treatment can cause deterioration of the contact between Al and the active layer when it is dissolved at high P_{vap} . The SVA+TA treatment involved additional thermal annealing at 140 °C for 10 min of SVA devices.

It is clear that device performance is enhanced by annealing. As shown in Figure 5.4a, for the as spun device, the maximum external quantum efficiency (EQE) is 45%. In contrast, devices fabricated with SVA and SVA+TA yield a maximum EQE of 55%. Here, the TA devices show the highest EQE of 62%. The same trend exists in the current-voltage

(J - V) characteristics in Figure 5.4b. As summarized in Table 5.1, devices fabricated by SVA give power conversion efficiencies (PCE) of 2.6% compared to only 1.5% for as-spun devices. This improvement is attributed to an increase in short-circuit current (J_{sc}) from 6.5 to 9.7 mA cm^{-2} , and fill factor (FF) from 37.2% to 53.1%. The additional thermal annealing step improves the PCE to 3.0% with a clear increase in FF to 64%, higher than the TA reference cell. However, the highest J_{sc} of 11.7 mA cm^{-2} is achieved in the TA device, which leads to its highest PCE among devices using different annealing protocols.

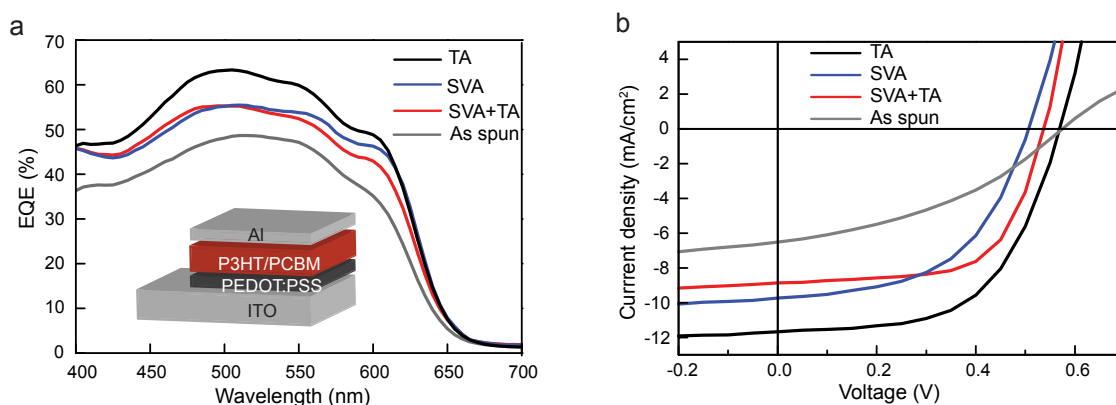


Figure 5.4 Device characteristics of P3HT/PCBM solar cells. a) EQE spectra. Inset showing a schematic structure of a typical standard device. b) J - V curves measured under a solar simulator.

Table 5.1 Device parameters of P3HT/PCBM standard solar cells presented in Figure 5.4.

	J_{sc} (mA cm^{-2})	V_{oc} (V)	FF(%)	PCE (%)
As spun	6.5	0.57	37.2	1.5
TA	11.7	0.57	57.6	3.8
SVA	9.7	0.51	53.1	2.6
SVA+TA	8.9	0.54	64.0	3.0

The P3HT/PCBM active layers in SVA and SVA+TA devices have a spherulitic morphology which improves long-range order of thiophene chains compared with that of TA devices. A better charge transport is expected from the enhanced chain packing. However, it could also be that the phases segregate more during the slow drying process such that excitons cannot diffuse to the interface and dissociate to form free charges. The higher PL yield in SVA films discussed above confirmed a reduction in efficient exciton dissociation. Due to the lack of direct evidence showing donor and acceptor domain size, it is difficult to ascribe the lower J_{sc} in spherulitic devices to over coarsening of the phases. Moreover, the

high surface roughness in SVA films observed from the AFM images may create trapping of charges at the cathode interface.

Another consideration is the surface segregation of P3HT which is usually found at the free surface for P3HT/PCBM films.⁹² For standard solar cells, the enrichment of P3HT at the cathode interface is a disadvantage for charge collection as P3HT is a hole conducting material. P3HT/PCBM active layers annealed without the Al top electrode yield an enrichment of P3HT at the free surface. In the SVA experiment, the P3HT/PCBM active layer was exposed to CS₂ vapor and the surface wetting of P3HT is inevitable. Therefore, we fabricated inverted solar cells where the surface enrichment of P3HT is favored for hole collection from the top electrode.

5.3.4 Device Characterization of Inverted P3HT/PCBM Solar Cells

We examined the photovoltaic performance of P3HT/PCBM devices in an inverted architecture. The device is based on ZnO as the electron selective layer and MoO₃/Ag as hole selective layers, as shown in the inset of Figure 5.5a. The thin layer of MoO₃ layer (6 nm) is essential for hole extraction.¹³⁰ P3HT/PCBM photoactive layers were spin-coated on top of ZnO and the resulting films were annealed by different protocols. In contrast to the devices with standard layer sequence, all the annealing processes were conducted without top electrode.

Figure 5.5 shows the EQE and J - V characteristics for the inverted P3HT/PCBM devices. Consistent with results from the series of standard devices, the TA device, as the reference cell, shows the highest EQE with a maximum of 65%. The EQE for both SVA and SVA+TA show no appreciable difference with maxima of 55%. From the J - V curves for these devices, it is clear that J_{sc} follows the trend expected from the EQE spectra. As summarized in Table 5.2, the J_{sc} for the TA device is 10.0 mA cm⁻², and decreased to 9.1 mA cm⁻² for the SVA device and to 8.6 for the SVA+TA device. On the other hand, V_{oc} also decreased from 0.56 V to 0.46 V. In principle, the V_{oc} is determined by: 1) the energy offsets between the donor and acceptor materials and 2) the energy-level alignment at the electrode-organic layer interface.²⁴ The decrease in V_{oc} after SVA may be due to the high charge carrier losses at the organic/electrode interface. Films after SVA show a much coarser texture with hill-like

5.3 Results and Discussion

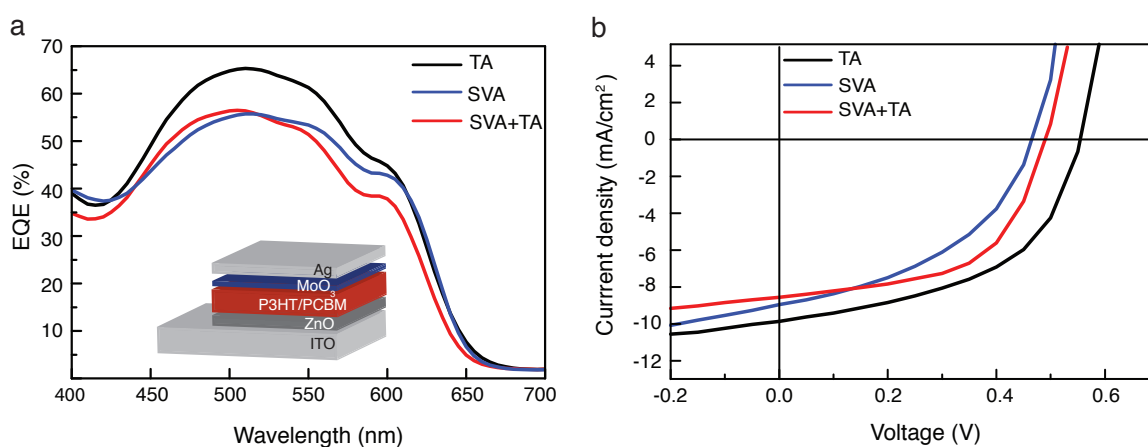


Figure 5.5 Device characteristics for P3HT/PCBM solar cells with inverted structure. a) EQE spectra. Inset showing a schematic drawing of a typical inverted structure device. b) J - V curves measured under a solar simulator.

features compared to the TA film, which may form current leakage pathways and result in a low shunt resistance. The performance of SVA devices can be improved using additional thermal annealing (SVA+TA), with a significant increase in FF from 44.6% to 55.6%, and PCE from 1.9% to 2.4%.

Table 5.2 Device parameters of P3HT/PCBM inverted solar cells presented in Figure 5.5.

	J_{sc} (mA cm ⁻²)	V_{oc} (V)	FF	PCE (%)
TA	10.0	0.56	50.5	2.8
SVA	9.1	0.46	44.6	1.9
SVA+TA	8.6	0.49	55.9	2.4

The performance of the inverted devices follow the same trend as the results in the previous section. The reference device showed the best efficiency, but the highest fill factor was achieved in the SVA+TA device. It should be mentioned that an optimized morphology for the photovoltaic layer has a requirement on the size of PCBM aggregates, which was found to be in the range of 3-20 nm.^{87,89,131} The annealing methods could influence the development of PCBM domains and affect the device performance. The good fill factor can be related to the improved molecular order of P3HT in spherulitic structure as observed in Figure 5.3, since the charge carrier mobility in crystalline P3HT is higher than in amorphous P3HT. Higher mobility can improve the charge transport and reduce space-charge effects. Furthermore, the improved local charge mobility together with good percolation pathways to electrodes facilitates the dissociation of geminate excitons at the interface.

These device results imply that a BHJ nanomorphology is formed when P3HT forms spherulitic superstructures. The intrinsic 10-nm length scale of spherulitic lamellae provides the structural size that is needed for exciton dissociation. In the absence of macroscopic phase separation, a PCBM percolation pathway is formed at the same time for electron transport.

5.4 Conclusion

This chapter has presented the control of P3HT crystallization to form microscale spherulitic structures and its influence on the resulting device performance. The spherulitic P3HT/PCBM films show a significantly improved chain ordering as proven by enhanced light absorption. Spherulitic solar cells exhibit good device performance, and efficiencies of 3.0% and 2.4% were achieved for standard and inverted structures, respectively. The device results indicate a favorable morphological development upon spherulitic crystallization of P3HT: 1) a large interface between P3HT/PCBM phases; 2) good percolation pathways to the electrodes; 3) improved mobility of charge carriers due to high crystallinity. Despite their lower efficiencies (mainly caused by decreased photocurrent), spherulitic devices achieve a high fill factor due to the improvement of charge transport from the ordered P3HT. These results can be related to the findings from the miscibility study of P3HT/PCBM in Chapter 4, and demonstrate that the P3HT-crystallization-driven structure formation produce a nanomorphology that is beneficial for BHJ device operation.

Chapter 6 Structure Formation in P3HT/F8TBT Blends

This chapter studies the structure evolution of P3HT/F8TBT blends. The surface morphology of semicrystalline P3HT blended with F8TBT is compared with blends with amorphous P3HT over a wide composition range. The phase separation patterns observed in amorphous mixtures of regiorandom P3HT/F8TBT indicate that the blend is immiscible. Regioregular P3HT/F8TBT blends in contrast show a morphology dominated by crystallization despite the presence of a miscibility gap. X-ray scattering studies reveal that the lamellar crystallization of P3HT is not perturbed by the addition of F8TBT. The long period of P3HT increases with F8TBT composition suggesting that a certain amount of F8TBT is mixed in the interlamellar amorphous region. Surface segregation of F8TBT at the bottom interface is confirmed by an X-ray reflectivity analysis. To correlate the blend morphology with device operation, spherulitic P3HT/F8TBT films were prepared by solvent vapor annealing, and the performance of solar cells based on these layers was investigated.

6.1 Introduction

Organic solar cells based on conjugated polymers as electron donor and fullerene derivatives as electron acceptor have attracted considerable interest over the past years. Since the initial demonstration of polymer/fullerene systems, device efficiencies have substantially improved through optimization in film morphology. While polymer/fullerene systems show better device performance, polymer/polymer blends offer some potential advantages. The variation in chemical structures enables the tuning of semiconducting properties such as

the bandgap and energy levels, and thus more light can be absorbed and high open circuit voltages can be generated.^{11,12,132,133}

The recent performance of polymer/polymer solar cells, with PCE of $\sim 6\%$,¹³⁴ is still relatively poor compared to polymer/fullerene devices. Polymer/polymer systems often suffer from geminate recombination of electron-hole pairs that can trap at the donor-acceptor interface, whereas fullerene acceptors show enhanced electron delocalization limiting recombination. Many polymer/polymer pairs are immiscible because of their high molecular weight and the resulting entropy constraints.¹³⁵⁻¹³⁸ Therefore, the understanding and control of phase separation in these polymer blends is crucial for the optimization of device performance.

Presently, device optimization is carried out empirically by varying film processing. The morphology is often optimized by using selective solvents for one polymer or by adding solvent additives in spin coating solutions.^{139,140} The use of post fabrication thermal annealing further alter the film morphology.¹⁴¹⁻¹⁴⁴ For the P3HT/F8TBT blend system, a five-fold increase in photocurrent and efficiency has been achieved by thermal annealing.¹⁴⁵ The improvement of device performance is correlated with the growth and purification of the ~ 10 nm domains as well as enhanced P3HT crystallization.¹⁴⁶ A bulk heterojunction donor and acceptor interface must have formed with length scales matched to the exciton diffusion length, but the processes by which the structure develops in P3HT/F8TBT are still not fully understood.

The morphology evolution is rather complex when the system consists of two competing pathways including polymer-polymer phase separation and crystallization. For many polymer/fullerene blends, structure formation has proven to be driven either by the crystallization of polymer or the aggregation/crystallization of fullerene.^{25,45} The non-polymeric nature of fullerene offers good miscibility in amorphous polymers, and also reduces kinetic trapping during demixing, which is different to polymer/polymer systems.

In this work, we have investigated the structure formation of P3HT/F8TBT blends, which shows competitive interactions between decomposition and crystallization. In contrast to previously studied P3HT/PCBM blends, amorphous P3HT and F8TBT show large-scale demixing above a composition ratio of ~ 10 wt% when equilibrated from the melt. While

the lateral phase-separated patterns are observed in amorphous mixtures, regioregular P3HT/F8TBT blends exhibit a crystallization determined morphology over the entire composition range. An X-ray scattering study was performed to investigate the change in P3HT morphology and crystal structure. The results indicate a structure framework established by P3HT lamellae, with F8TBT partially mixing within amorphous interlamellar regions. To examine the relevance of this P3HT crystallization-induced structure to a BHJ morphology, we fabricated solar cell devices with spherulitic P3HT/F8TBT films, which were equilibrated using solvent vapor annealing. P3HT/F8TBT photovoltaic devices with different spherulitic sizes were compared to the optimized thermal annealing condition, showing only moderate device efficiencies.

6.2 Experimental Methods

Blend solutions of P3HT/F8TBT were prepared with a total concentration of 15 mg/mL in chlorobenzene. The weight ratios of F8TBT to P3HT ($f = m_{\text{PCBM}}/m_{\text{polymer}}$) were varied from $f = 0$ to $f = 2$. Films were prepared by spin coating either on quartz glass for AFM and UV-Vis, on silicon substrates for X-ray scattering measurements, or on PEDOT:PSS-coated ITO substrates for photovoltaic device fabrication. Melt annealing was carried out on spin coated films by first heating on a hotplate at 230 °C for 3 min, and then cooling down to room temperature at a rate of 5 °C/min.

P3HT-RR2/F8TBT films were used for the X-ray structural study. GISAXS and GIWAXS were performed at beamline D1, at the Cornell High Energy Synchrotron Source (CHESS) at Cornell University, U.S.A. The wavelength was $\lambda = 1.15 \text{ \AA}$. A beam stop for the primary beam and the GISAXS signal was employed. A CCD detector with a pixel size of $46.9 \times 46.9 \mu\text{m}^2$ was used with a sample-detector distance of 1.81 m (GISAXS) and 0.25 m (GIWAXS). Images were then taken at an incident angle of 0.13° for GISAXS and 0.15° for GIWAXS, which are slightly higher than the critical angle of the polymer film and lower than that of the substrate. Therefore the entire film was penetrated, and internal film structures could be detected with the beam fully reflected from the sample/substrate interface. The q -space calibration was performed by fitting the characteristic scattering signal arising from silver behenate.

X-ray reflectivity (XR) measurements were performed *in-situ* using the collimating slits, goniometer and sample environment of the GISAXS experiments. The detector was an ion chamber with an aperture of 50 mm in height and 13 mm in width. A blade placed in front of the ion chamber screened the detector at low angles from the direct beam. The measuring time was 1 s per point. The electronic background was measured and subtracted from the data. Model fitting was carried out using the Parratt algorithm (HMI, Berlin). All the scattering measurements and data analysis in this chapter were performed by Dr. Alessandro Sepe.

Photovoltaic devices were fabricated in standard PEDOT:PSS|ITO|P3H/F8TBT|Al layer sequence. Here, the commercially available P3HT-RR1 was used with F8TBT at $f = 1$. P3HT/F8TBT photoactive layers were processed with different annealing protocols. Solvent vapor annealing (SVA) was used to produce spherulitic P3HT/F8TBT films. Thermal annealing (TA) was performed at 140 °C for 10 min after Al deposition. Devices were characterized by external quantum efficiency (EQE) and current-voltage (J - V) measurements.

6.3 Results and Discussion

6.3.1 Surface Morphology of P3HT/F8TBT

To investigate the miscibility of P3HT and F8TBT, we examined the surface morphology of blend films after melt annealing. Three sample series, P3HT-RA/F8TBT, -RR1/F8TBT and -RR2/F8TBT were studied with blend ratios varying from $f = 0.25$ to $f = 2$. Initially, as spun films showed a homogeneous surface morphology for all the three sample series (not shown) as a result of a fast quench from solution to non-equilibrium blends, which suppressed phase separation and crystallization. Melt annealing involving a slow cool down process (rate: 5 °C/min) helped to reach thermodynamic equilibrium.

Figure 6.1 shows AFM height images of 80~100 nm thick films after cooling from the melt. P3HT-RA/F8TBT blends are amorphous/amorphous mixtures, in which typical lateral phase separation morphology is observed indicating poor miscibility between the two polymers. The concentration of F8TBT affects the phase-separated structure, which develops from isolated circular domains (Figure 6.1a) to elongated stripes (Figure 6.1b). The intercon-

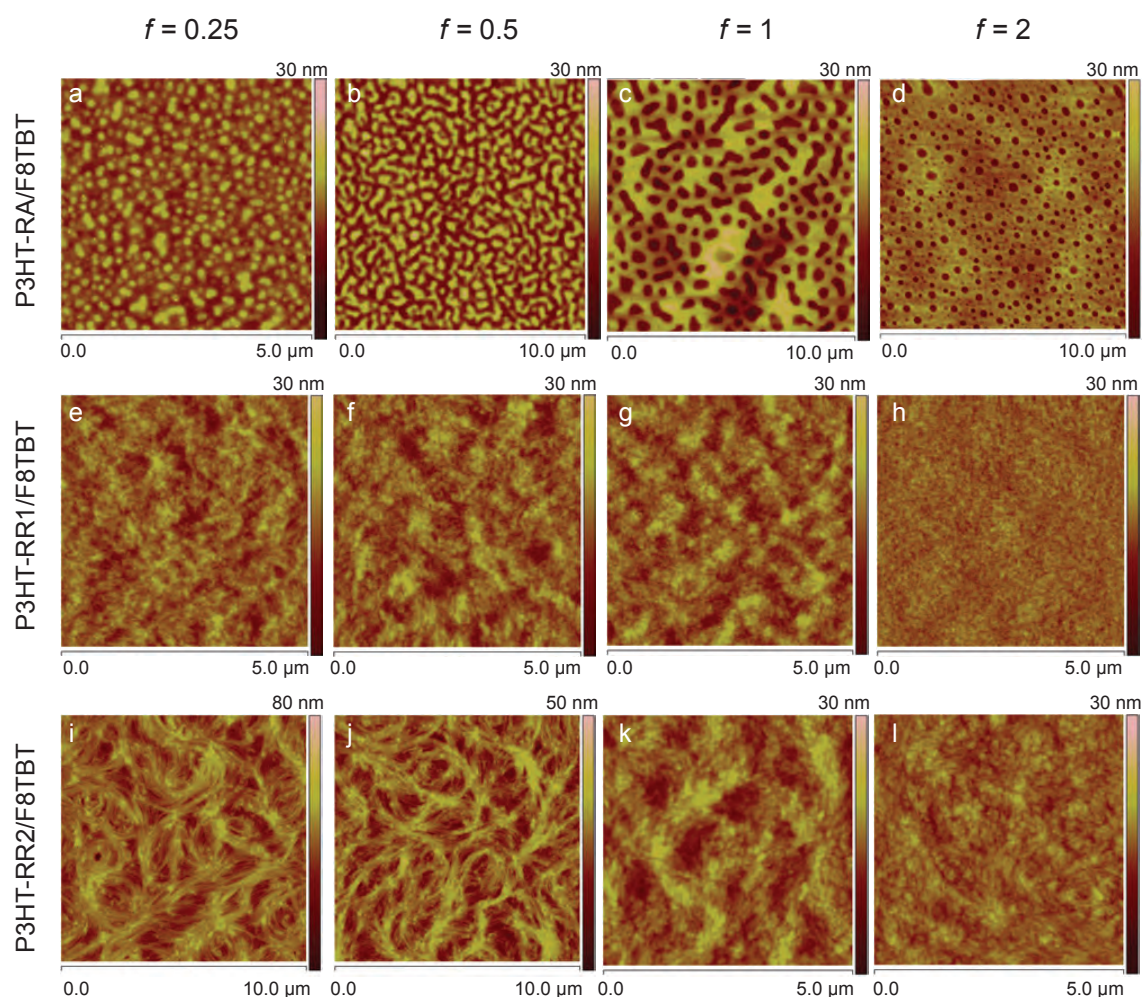


Figure 6.1 AFM images of (a-d) P3HT-RA/F8TBT, (e-h)P3HT-RR1/F8TBT, (i-l) P3HT-RR2/F8TBT thin films after melt annealing. The F8TBT to P3HT weight fraction was varied from $f = 0$ to $f = 2$.

nected matrix break up to form holes (Figure 6.1c, d) as f is increased from 0.25 to 2. Films with lower f were also investigated (Figure 6.2). Homogeneous surfaces were obtained once the F8TBT content was reduced to $f = 0.1$, indicating a miscibility much lower than that of P3HT/PCBM blends.

The surfaces of blends using semicrystalline P3HT-RR1 (Figure 6.1e-h) and P3HT-RR2 (Figure 6.1i-l) did not show phase separation over the $f = 0.25$ to $f = 2$ range. For P3HT-RR2/F8TBT blends, it is interesting to note that the film surfaces exhibit distinctive spherulite features at $f = 0.25$ and $f = 0.5$. As the F8TBT concentration increases to $f = 1$ and $f = 2$, the surfaces became smoother accompanied by the loss of distinct P3HT spherulites.

A comparison of the surface morphology suggests that there is a strong interference between phase separation and crystallization in P3HT/F8TBT blends. The competition

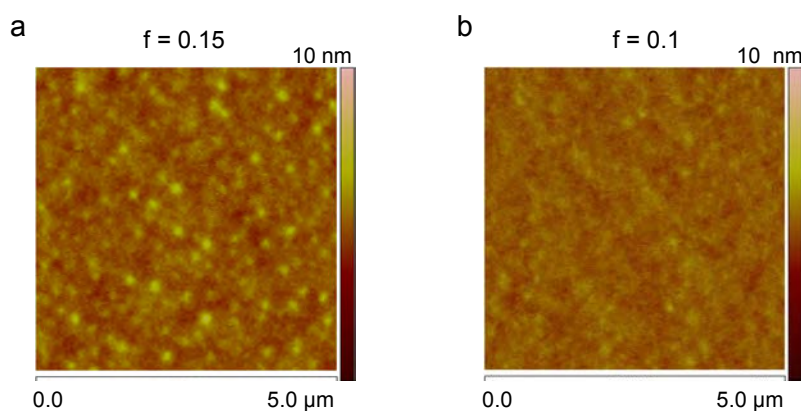


Figure 6.2 AFM images of P3HT-RA/F8TBT after melt annealing with a) $f = 0.15$ and b) $f = 0.1$.

between crystallization and phase separation is complex as several scenarios are possible when cooling from melt to the solid state: 1) simultaneous phase separation and crystallization. 2) crystallization-induced phase separation; 3) phase separation-induced crystallization. Case 2 is excluded as macroscopic phase separation is observed between amorphous P3HT and F8TBT. Case 3 is also unlikely due to the fact that P3HT can form a spherulitic superstructure in blends, indicating that crystallization of P3HT is the dominating driving force. Herein we explain the lack of phase-separated structure with crystallization-directed structure formation in P3HT-RR1 and -RR2/F8TBT. However, it is possible that vertical phase separation can take place within the crystalline/amorphous blend films, which may conceal structures beneath the surface.

6.3.2 Melt Recrystallization of P3HT/F8TBT

In addition to AFM surface morphology investigation, the crystallization of P3HT/F8TBT blends was studied by UV-Vis spectroscopy on the P3HT-RR1/F8TBT films. The spectra of as spun films as well as after melt annealing are shown in Figure 6.3. The annealed films show enhanced absorbance in the range of 500~625 nm, accompanied by a strengthening P3HT vibronic peak near 610 nm. These changes indicate the increased crystalline order of P3HT. An isosbestic point is observed at ~415 nm in both as spun and annealed films. In order to verify the existence of the isosbestic point in annealed films, the UV-Vis spectra in Figure 6.3b were integrated in wavelength ranges in which the signal is dominated by P3HT (between $\lambda_1 = 550$ nm and $\lambda_2 = 625$ nm) or F8TBT (between $\lambda_3 = 265$ nm and $\lambda_4 = 375$ nm)

absorbance.

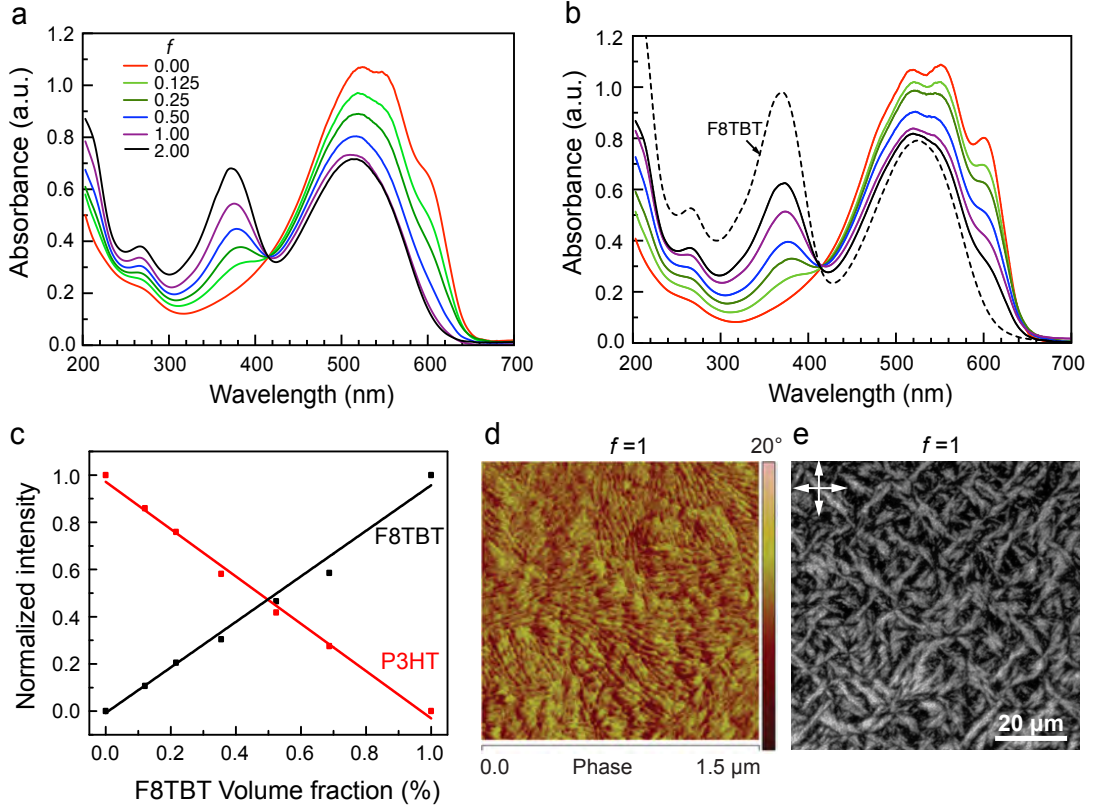


Figure 6.3 UV-Vis spectra of P3HT-RR1/F8TBT blend films with F8TBT compositions ranging from $f = 0$ to $f = 2$ a) as spun and b) after melt annealing. c) Integrated intensities versus F8TBT volume fractions. d) AFM phase image and e) POM image of P3HT-RR1/F8TBT ($f = 1$) after melt annealing.

The integrated intensities are given as a function of the volume fraction of F8TBT, according to $\phi = (1 + (\rho_{\text{F8TBT}}/\rho_{\text{P3HT}})/f)^{-1}$. The densities of P3HT and F8TBT used for the analysis are $\rho_{\text{F8TBT}} = 1 \text{ g/cm}^3$ and $\rho_{\text{P3HT}} = 1.15 \text{ g/cm}^3$.^{101,147}

The absorbance intensity of P3HT was normalized to pure P3HT ($\phi = 0$) after subtracting the F8TBT absorbance.

$$I_{\text{P3HT}}(\phi) = \frac{\int_{\lambda_1}^{\lambda_2} d\lambda [I(\lambda, \phi) - \phi \cdot I(\lambda, 1)]}{\int_{\lambda_1}^{\lambda_2} d\lambda I(\lambda, 0)} \quad (6.1)$$

For F8TBT, the absorbance signal was normalized to pure F8TBT ($\phi = 1$) after subtracting the absorbance originating from P3HT.

$$I_{\text{F8TBT}}(\phi) = \frac{\int_{\lambda_3}^{\lambda_4} d\lambda [I(\lambda, \phi) - (1 - \phi) \cdot I(\lambda, 0)]}{\int_{\lambda_3}^{\lambda_4} d\lambda I(\lambda, 1)} \quad (6.2)$$

The integrated intensities of P3HT and F8TBT show a linear correlation of absorbance with volume fraction (Figure 6.3c). The lines of P3HT and F8TBT intersect at $\phi = 0.5$, which implies that the absorbance signals from these two components are additive. Since P3HT shows a very different absorbance in the amorphous P3HT (450 nm) and crystalline state, the isosbestic point can only occur when the amorphous/crystalline ratio in P3HT is not strongly affected by the addition of F8TBT. Moreover, the morphology of a blend with $f = 1$ was investigated to show P3HT lamellar stacks on the film surface (Figure 6.3d). The formation of spherulites can be seen in the POM image (Figure 6.3e). This also supports that crystallization of P3HT is not strongly affected upon mixing with F8TBT.

6.3.3 Structural Study on P3HT/F8TBT Thin Films using X-ray Scattering

In order to investigate the effects of F8TBT addition on the crystallization of P3HT, P3HT-RR2/F8TBT films were studied using GISAXS and GIWAXS in the range of $f = 0$ to $f = 1.5$. P3HT-RR2 was chosen because of its low polydispersity and nearly 100% regioregularity which allows us to resolve the long period of P3HT from GISAXS. The detailed lamellar crystal structure of P3HT is introduced in Chapter 4. Figure 6.4 shows the GISAXS patterns of P3HT-RR2/F8TBT films after cooling from the melt. The integrated profiles are shown in Figure 6.5.

The pure P3HT film shows a lateral scattering signal at $q_y = 0.045 \text{ \AA}^{-1}$, corresponding to a long period of $L_p = 14 \text{ nm}$. P3HT/F8TBT blend films show similar scattering patterns but the peak shifts to lower q with increasing F8TBT concentration. This stems from an increase in the long period to 15 nm at $f = 0.6$ and to 16 nm at $f = 1$. GIWAXS was performed on the same samples to investigate the crystalline structure of P3HT/F8TBT blends, as shown in Figure 6.6. In contrast to the change in L_p , the (100) and (200) P3HT Bragg peaks at $q_z = 0.39 \text{ \AA}^{-1}$ and $q_z = 0.78 \text{ \AA}^{-1}$ remain constant upon increasing F8TBT content. The intensity variation of higher order peaks is caused by a relative decrease of the P3HT content. In addition, there is a (010) reflection from the π - π stacking at $q_y = 1.72 \text{ \AA}^{-1}$. This implies that P3HT mainly adopts an edge-on orientation.

The well-defined P3HT-RR2 forms chain-extended lamellae and the increase in L_p is directly correlated with the incorporation of F8TBT into amorphous interlayers. Un-

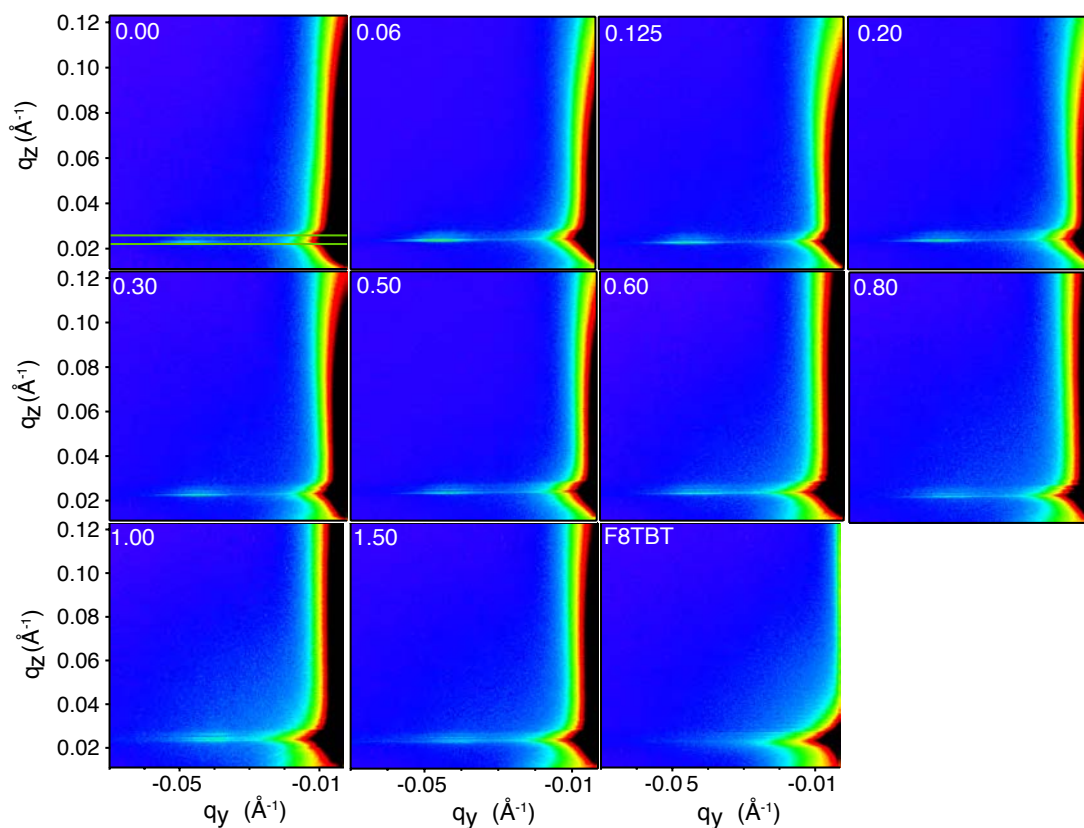


Figure 6.4 GISAXS patterns of P3HT-RR2/F8TBT films showing a scattering signal at $q_y \approx 0.045 \text{ \AA}^{-1}$ arising from lateral structures corresponding to the long period L_p in P3HT. The GISAXS image of F8TBT is shown for reference. The horizontal lines in the top-left GISAXS image show the region used to construct the 1D intensity profiles along q_y . The F8TBT weight fraction, f , is given in the images.

like P3HT/PCBM in which swelling of amorphous regions saturates around $f = 0.185$, P3HT/F8TBT shows a continuous increase in L_p up to a F8TBT loading of $f = 1$. In a first rough estimation, this 2 nm increase in L_p corresponds to a volume fraction of 14% in P3HT. Assuming similar densities, it seems clear that not all the F8TBT is accommodated within the amorphous P3HT regions. It is most likely that a large amount of F8TBT is segregated out of the interlamellar regions.

Due to the existence of a miscibility gap of amorphous P3HT/F8TBT, phase separation is expected at a F8TBT blend ratio above $f = 0.1$. However, we observe neither macroscopic demixing nor other structural signals from GISAXS. This implies that the amorphous regions do not phase separate immediately upon passing the binodal composition; instead, supersaturation of the composition may occur due to kinetic limitations.

It is difficult to determine the spatial distribution of F8TBT in the blend films based on

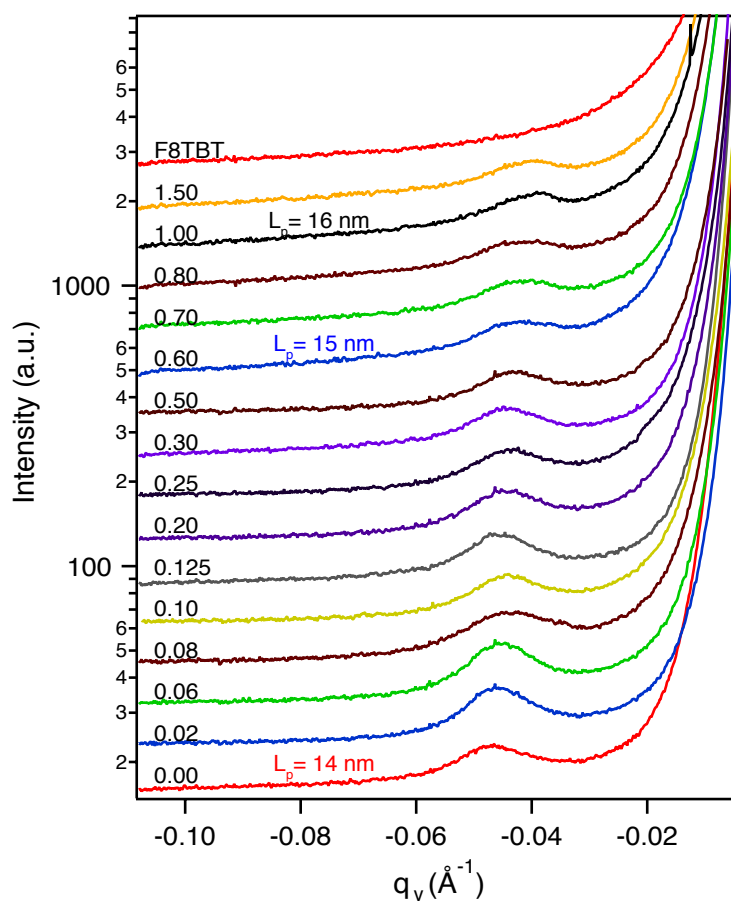


Figure 6.5 a) Integrated GISAXS intensity profiles along q_y of P3HT-RR2/F8TBT films with increasing F8TBT from $f = 0.0$ to $f = 1.5$. The curves are vertically shifted for clarity.

GISAXS and GIWAXS results. In addition to the F8TBT segregation within interlamellar regions, it must also be segregated to other amorphous grain boundaries, including inter-fibrillar (between the fibrils or lamellar bundles in spherulites) and inter-spherulitic regions, as well as the film interfaces.

In order to discriminate these possibilities, XR was used to investigate the vertical composition of the P3HT/F8TBT film with $f = 1$, as shown in Figure 6.7a. The XR data was simulated using a multilayer model that incorporates several variable parameters including film thickness, densities, and roughness at interfaces. From the scattering length densities (SLDs) of pure P3HT ($1 \times 10^{-5} \text{ \AA}^{-2}$) and F8TBT ($0.92 \times 10^{-5} \text{ \AA}^{-2}$), the SLD of the P3HT/F8TBT blend with $f = 1$ is expected to be $0.96 \times 10^{-5} \text{ \AA}^{-2}$. In fitting, the SLD of both the polymer film and the substrate were left as free fitting parameters, as well as the SLD and the thickness of the SiO_x layer. For Si and SiO_x , the SLD values were $2.2 \times 10^{-5} \text{ \AA}^{-2}$ and $2.3 \times 10^{-5} \text{ \AA}^{-2}$, respectively and a thickness of 2 \AA was obtained for SiO_x . The

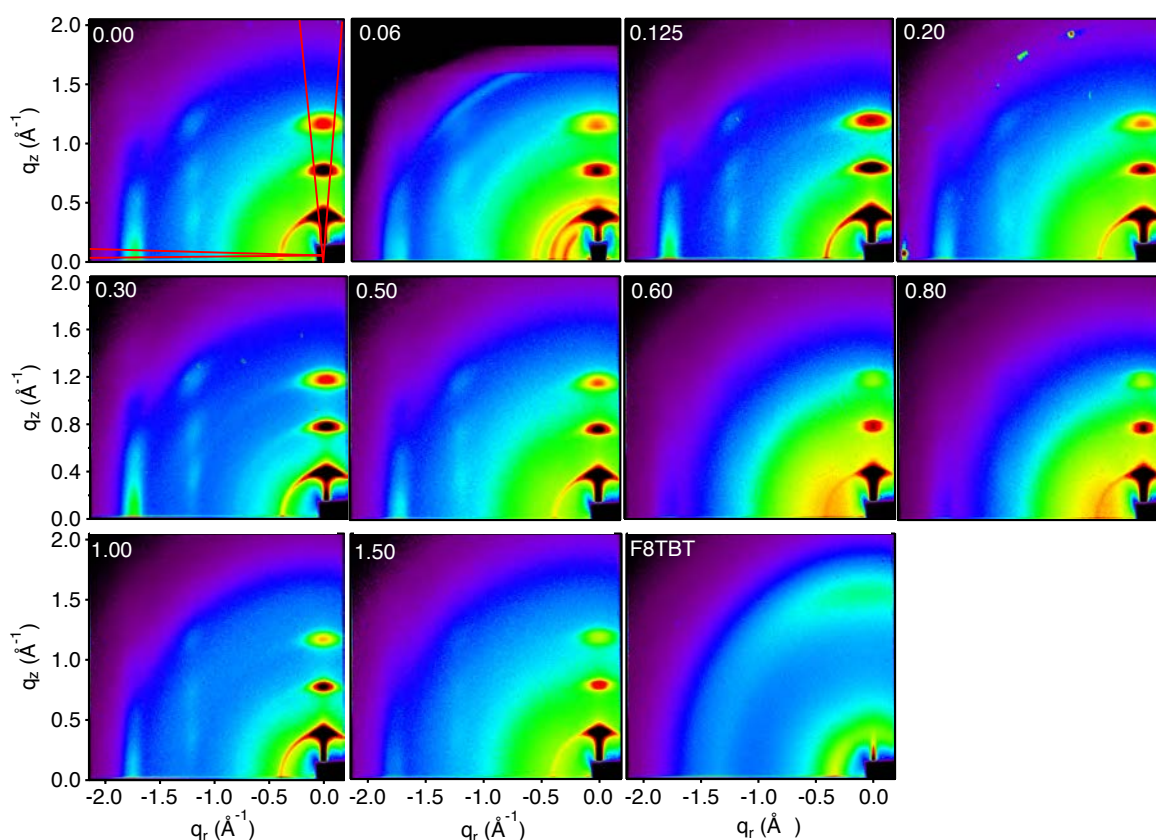


Figure 6.6 a) GIWAXS patterns show the characteristic P3HT scattering signal. The vertical alignment of the (h00)-reflections indicates an edge-on orientation of P3HT. F8TBT shows a face-on orientation of π - π stacking at $q_z \approx 1.55 \text{ \AA}^{-1}$. The lines in the top-left image indicate the sectors used for the radial integration of the scattering peaks.

most important observation is the decrease in density occurs at the film/substrate interface, which corresponds to the surface segregation of F8TBT with thickness of $\sim 20 \text{ nm}$.

Due to the similar SLDs of P3HT and the P3HT/F8TBT mixture, the expected P3HT surface layer is not resolved by XR. However, surface enrichment of P3HT was seen in AFM images (Figure 6.3d). A $1\sim 2 \text{ nm}$ thick P3HT layer at the top surface of the blend was revealed by XPS depth profiling in the literature.¹⁴⁸ The vertical structure for the 100 nm thick P3HT/F8TBT film therefore consists of a P3HT enrichment layer at top surface followed by constant composition in the film, and a 20 nm F8TBT layer at the bottom surface. The 20 nm thick F8TBT corresponds to $\sim 40\%$ of the initially added F8TBT content, which results in the blend ratio in the bulk of $f \approx 0.6$, much less than the initial value of $f = 1$.

In this section, we confirm the P3HT crystallization-directed structure formation in P3HT/F8TBT blends. The morphology in P3HT/F8TBT blends is determined by the crys-

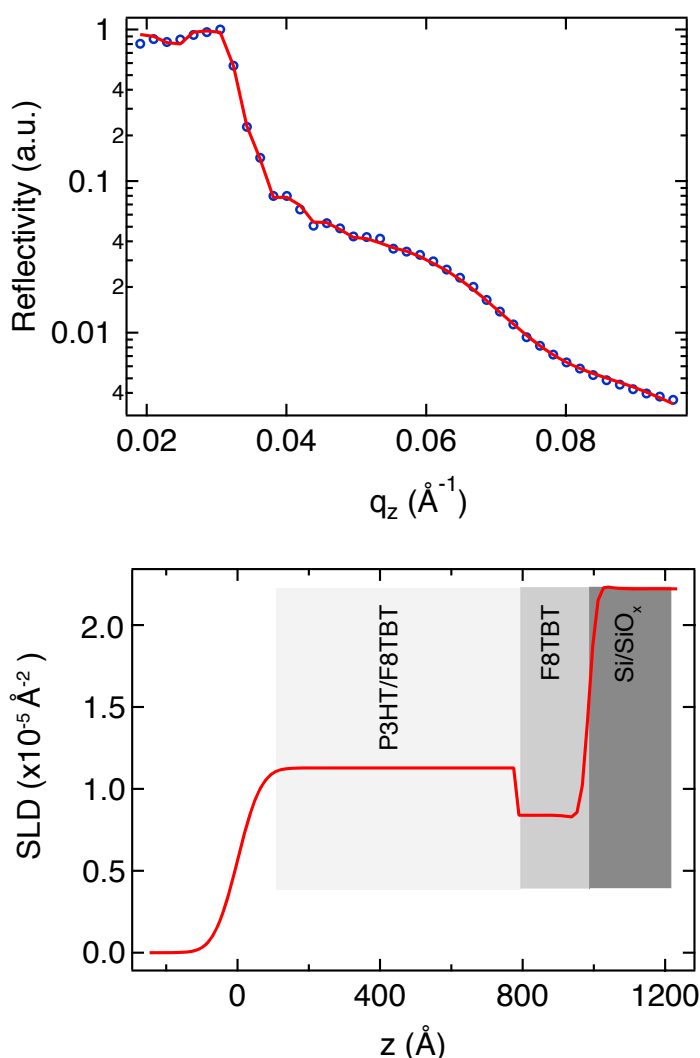


Figure 6.7 a) Measured XR and b) SLD profile of the P3HT/F8TBT film with $f = 1$.

tallization of P3HT and the exclusion of F8TBT out of interlamellar regions above the miscibility limit. Upon cooling from the initial isotropic melt, crystallization of P3HT precedes thermodynamic phase separation, which expels F8TBT into the amorphous regions and to the substrate/film interface. The fact that F8TBT can be located at multiple locations within the film could points to the coexistence of different types of morphologies.

The spherulitic P3HT constructs a framework on the 10 nm length scale with a structural size determined by lamellar crystals. We also speculate that the amorphous mixture of P3HT and F8TBT outside the interlamellar regions is in a supersaturated state. Furthermore, it should be noted that the structure found in this study can not be directly applied to P3HT/F8TBT active layers in photovoltaic devices, which are prepared through an off-

equilibrium protocol. However these results are important to gain an understanding of blend demixing during film processing or device ageing.

6.3.4 Spherulitic Crystallization of P3HT/F8TBT

In order to verify the findings from the above structural studies, we fabricated photovoltaic devices with P3HT/F8TBT active layers that were equilibrated using solvent vapor annealing (SVA). SVA method was used to control the nucleation density and growth rate of P3HT in P3HT/PCBM as described in Chapter 5. Here we applied the same method to P3HT/F8TBT. The film with composition of $f = 1$ was investigated as it corresponds to the composition of optimized photovoltaic devices. Carbon disulfide (CS_2) is a good solvent for both P3HT and F8TBT, enabling sufficient mobility for the blend to reorganize its morphology towards thermodynamic equilibrium. The P3HT/F8TBT film is relatively stable upon swelling at high solvent vapor pressures (P_{vap}) and dewetting is less problematic compared to P3HT/PCBM films, which have a much lower viscosity upon solvent uptake. Thus we can control the nucleation density to grow spherulites with different sizes in blend films.

The as spun film was first swollen in CS_2 vapor to dissolve most of the initial crystal nuclei. By using *in situ* UV-Vis spectroscopy, we found that at a vapor pressure of 95% all P3HT aggregates were dissolved. At this stage the film was a swollen mixture of amorphous P3HT and F8TBT. The growth of P3HT spherulites was performed at a constant recrystallization vapor pressure ($P_{\text{vap}}^{\text{cryst}}$) for 30 min after swelling at for 10 min.

Figure 6.8 presents typical POM images of P3HT/F8TBT films by varying $P_{\text{vap}}^{\text{cryst}}$ from 80% to 60%. Similar to the isothermal crystallization from polymer melts, the overall crystallization rate is faster due to the larger number of nuclei generated at higher undercooling (i.e. lower $P_{\text{vap}}^{\text{cryst}}$), which produces smaller spherulites.

The as-spun P3HT/F8TBT film shows no birefringence (Figure 6.8a), but after the SVA process, films show distinct Maltese cross patterns (Figure 6.8b, c and d). The films exhibit a clear spherulitic morphology with sizes in the order of 10 μm . A weak anisotropic texture is only observed in films prepared with $P_{\text{vap}}^{\text{cryst}} = 60\%$, which indicates a high nucleation density. In all cases, the films were macroscopically homogeneous and showed no phase separation as seen by AFM. This strongly indicates the structure formation in the blend is

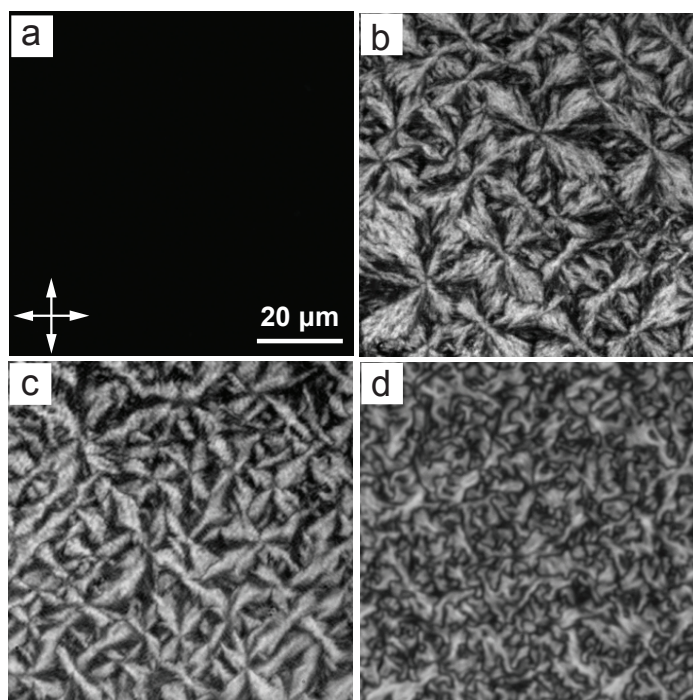


Figure 6.8 POM images of P3HT/F8TBT films crystallized by SVA at different $P_{\text{vap}}^{\text{cryst}}$ for 30 min after initial swelling at 95% for 10 min. a) As spun, b) 80% (SVA1), c) 70% (SVA2), and d) 60% (SVA3).

dominated by P3HT crystallization rather than phase separation of the two polymers.

The results above show that the crystallization of P3HT is not strongly affected and its spherulitic growth in blends is possible. The swelling of amorphous inter-lamellar region is evident from GISAXS measurements, implying an inter-lamellar segregation. The abundant F8TBT, which cannot be accommodated within the inter-lamellar amorphous P3HT regions does not create an observable lateral phase separation. We attempted to resolve the film morphology by TEM, but it is difficult to distinguish between the donor and acceptor phases due to the limited contrast between P3HT and F8TBT. Additionally, we found a very different nanomorphology in the SVA film in comparison to the thermal annealed (TA) film (Figure 6.9). The darker regions in Figure 6.9a and b may be due to thickness variations in films. A nanostructure resembling lamellar stacking is observed in the SVA film (Figure 6.9b), while the TA film does not show any structural features. This implies that the spherulitic films prepared via SVA can have a long-range molecular order, which may be beneficial for charge transport in P3HT.

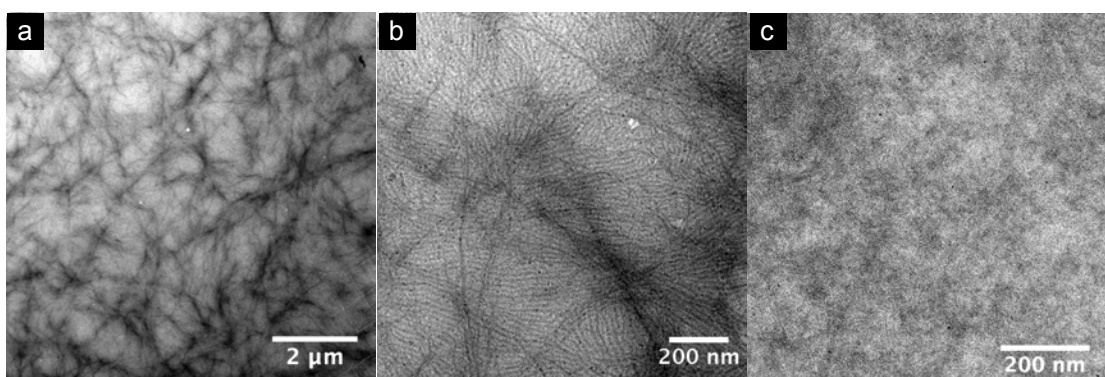


Figure 6.9 TEM images of P3HT/F8TBT films prepared via a, b) SVA crystallization at $P_{\text{vap}}^{\text{cryst}} = 60\%$, and c) TA.

6.3.5 Effects of Mesoscale Structure on Device Performance

We first recorded the UV-Vis and PL spectra of P3HT/F8TBT films prepared with different annealing conditions. Figure 6.10a presents the UV-Vis spectra of as spun, TA and SVA films. Figure 6.10 shows one representative SVA sample crystallized at $P_{\text{vap}}^{\text{cryst}} = 60\%$ as the SVA films with different spherulitic sizes have similar UV-Vis traces. While amorphous P3HT shows only a broad absorbance at 500 nm, crystalline and well-ordered P3HT exhibit distinct vibronic features above 610 nm. Both TA and SVA films exhibit enhanced absorbance with red-shifts of the main peaks, indicating better P3HT order.

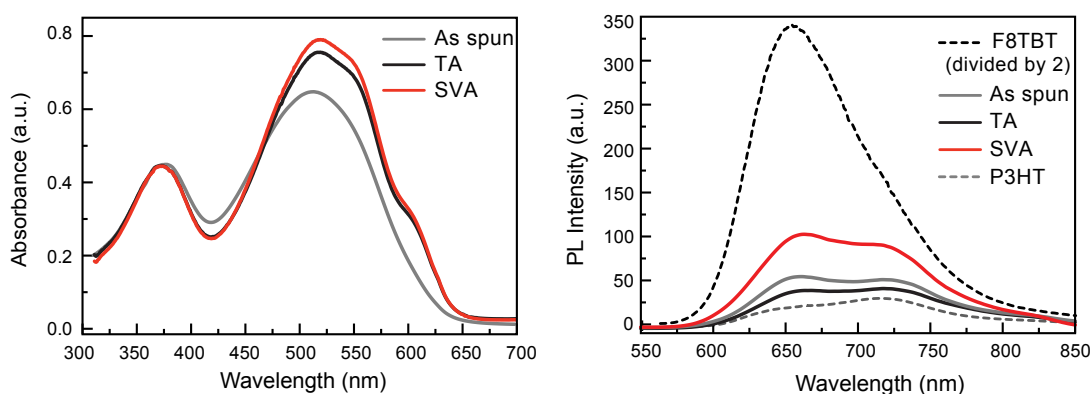


Figure 6.10 a) UV-Vis and b) PL spectra of P3HT/F8TBT ($f = 1$) films prepared with different annealing protocols.

PL spectra were used to study the efficiency of exciton dissociation in P3HT/F8TBT blends. The PL spectra of homopolymers and their blends are shown in Figure 6.10b. F8TBT shows strong luminescence with a peak centered at 650 nm, and P3HT has much lower emission with vibronic features at 650 nm and 720 nm. The PL intensities of blend films show

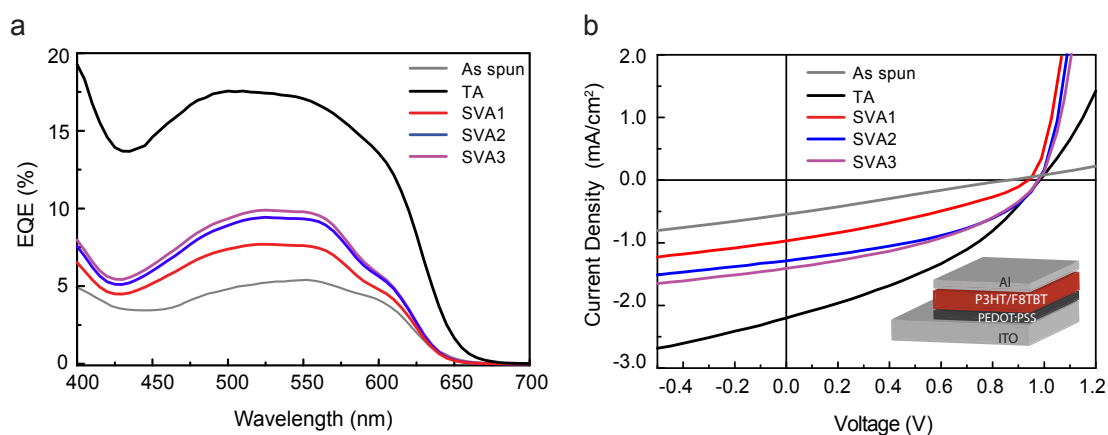


Figure 6.11 Device characteristics of P3HT/F8TBT solar cells. a) EQE spectra. b) J - V curves measured under a solar simulator. Inset showing a schematic drawing of device structure.

a significant decrease in comparison to pure F8TBT, indicating enhanced exciton quenching at the donor acceptor interface. Created excitons are efficiently quenched during their live time, i.e. they find a donor-acceptor interface within the range of the exciton diffusion length. The peaks at 650 nm and 720 nm in the PL spectra of the blends match the peaks for F8TBT and P3HT, respectively.

The decrease in PL intensity of the TA film as compared to as spun state is due to the low emissive characteristics of crystalline P3HT phase.¹⁴⁹ This indicates that thermal annealing improves the crystallinity of P3HT without significant phase coarsening. In comparison, SVA films show less quenching of F8TBT emission. This can be caused by a higher degree of phase separation between P3HT and F8TBT or improved phase purity, with fewer excitons reaching the interface and thus recombining radiatively. The PL intensity of SVA films remains far below that of F8TBT, suggesting P3HT and F8TBT are largely intermixed within the exciton diffusion range.

Figure 6.11 presents the device characteristics of P3HT/F8TBT prepared using different protocols. All devices were fabricated with PEDOT:PSS-coated ITO substrates and Al top electrodes. P3HT/F8TBT films with different spherulite sizes (Figure 6.8) were investigated. These devices were further annealed at 140 °C after Al deposition to ensure a good contact between the active layer and the electrode. The only thermally annealed device was included as reference. Figure 6.11a shows a significant improvement in the measured EQE upon annealing, with the maximum EQE increased from 5% to 18% of the TA device. SVA

devices have a maximum EQE in the range of 8%~10%, which decreases with increasing spherulite size.

Table 6.1 Device parameters of P3HT/F8TBT solar cells presented in Figure 6.11.

	J_{sc} (mA cm ⁻²)	V_{oc} (V)	FF	PCE (%)
As spun	0.5	0.85	21.7	0.10
SVA1	0.9	0.91	37.7	0.32
SVA2	1.3	0.98	42.9	0.54
SVA3	1.4	0.98	40.4	0.56
TA	2.2	0.98	33.8	0.87

The J - V characteristics of P3HT/F8TBT solar cells demonstrate a large improvement in device performance with annealing, as shown in Figure 6.11b. The performance parameters are summarized in Table 6.1. The device performance shows a five-fold increase in PCE from 0.10% for as spun to 0.56% for SVA3 device due to the change in both short-circuit current (J_{sc}) and fill factor (FF). J_{sc} directly correlates with the trend in EQE, with the highest value of 2.2 mA cm⁻² obtained in the TA device. For the SVA devices, J_{sc} increases from 0.9 to 1.4 mA cm⁻² with decreasing spherulite size. The low photocurrent is related to the smaller interfacial area compared to the TA film, as confirmed by the PL spectra. In addition, surface segregation of F8TBT at the PEDOT:PSS interface could act as a hole blocking layer that impairs charge collection.

Despite the lower J_{sc} of the SVA devices as compared to that of the TA device, spherulitic P3HT/F8TBT shows slightly improved fill factors, which reflects a reduction in recombination losses at the bulk heterojunction interface. This is attributed to a higher hole mobility from crystalline P3HT phase that results in more balanced hole and electron mobilities. The performances of spherulitic solar cells suggest that a bulk heterojunction morphology is formed in P3HT/F8TBT blends with a structure that is determined by the lamellar crystallization of P3HT, whereas an optimal morphology for device operation requires an off-equilibrium protocol to avoid coarsening of P3HT and F8TBT phases as well as the excess surface segregation of F8TBT.

6.4 Conclusion

In summary, we have demonstrated the crystallization-directed structure formation in P3HT/F8TBT system. In difference to P3HT/PCBM system, the amorphous P3HT/F8TBT blends exhibit a lower miscibility limit of $f = 0.1$, and lateral phase separation was observed over a wide composition range. X-ray scattering study reveals that, in semicrystalline P3HT/F8TBT blends, F8TBT is expelled to the interlamellar regions of P3HT, which leads to an increase in the long period. P3HT can form spherulitic crystals in blends, indicating that F8TBT does not perturb the ordering of P3HT crystalline lamellae. The limited miscibility of F8TBT with P3HT results in the segregation of F8TBT at the film/substrate interface.

The structure study of P3HT/F8TBT blends is correlated with the device performance of films with spherulitic morphology. In comparison to optimized thermal annealing, spherulitic P3HT/F8TBT solar cells show improved fill factors in spite of lower efficiencies due to a decreased photocurrent. These results imply that a bulk heterojunction structure is formed in P3HT/F8TBT with phase sizes determined by the lamellar crystallization of P3HT.

Chapter 7 Polymer Field-Effect Transistors

Based on P3HT/PEO Blends

This chapter investigates the phase separation behavior in crystalline/crystalline polymer blends consisting of P3HT and PEO. The spin coated thin films of P3HT/PEO blends show macro-scale lateral phase separation, whereas the self-assembly of P3HT nanowires in solution changes the morphology to vertical phase separation with enrichment of P3HT at the substrate interface. This enabled us to fabricate field-effect transistors that show charge carrier mobilities of $4 \times 10^{-3} \text{ cm}^2\text{V}^{-1}\text{s}^{-1}$ at an insulating PEO content as high as 90 wt%.

7.1 Introduction

Multicomponent systems have been used in organic polymer devices such as field effect transistors (FET) and photovoltaic cells because of the reduced cost, enhanced mechanical properties and environmental stability.^{150–153} Semiconducting and insulating polymer blend systems have potentials for the optoelectronic applications, but the presence of an insulating matrix tends to degrade the electronic performance by hindering charge transport.^{154–156}

FETs comprising of polythiophene/insulating polymer blends have demonstrated to approach the electronic performance of pure polythiophene, attributed to the segregation of the semiconducting polymer at the gate interface.^{157–159} It is known that the charge transport occurs in the first few molecular layers at the gate dielectric interface; therefore controlling the vertical phase separation in FETs is an effective approach to maintain the electronic performance of semiconducting polymer in the presence of an insulating matrix. However, the phase separation process is complicated in that it is not only governed by the thermody-

namics of the polymer blends, but also by the film formation kinetics. The final morphology in the film is sensitive to most processing factors including the solvent evaporation rate, solubility parameters, surface tension of the components, and the film thickness.^{108,160} Lateral phase separation is often found in polymer blend thin films, which cause the degradation of device performance because the charge transport only occurs in the semiconducting component. To this end, approaches to induce vertical phase separation in multicomponent semiconducting polymer systems is of great interest for device applications.

Previous studies by Goffri *et al.* using poly (3-hexylthiophene) (P3HT) with a semicrystalline polymer achieved good charge transport in FETs at P3HT content as low as 5 wt%.¹⁶¹ In such dilute blends, P3HT is excluded from the crystalline domains of the insulating matrix to produce vertically stratified structures. This was attained by a careful design of the solidification sequence by which P3HT and the matrix crystallize. Thin films were drop cast at temperature of ~ 120 °C, which is well above the glass transition temperature of the matrix polymers such as polyethylene and isotactic polystyrene, while P3HT can still crystallize. Indeed, when the solidification of the matrix polymer occurred first, P3HT would not be able to crystallize, which in turn resulted in poor electronic performance. As an alternative, FETs fabricated with P3HT nanowires embedded in the amorphous matrix have shown good electronic properties attributed to a highly crystalline network of P3HT.^{162,163} Methods for producing P3HT nanowires in solution have been developed mainly via cooling of saturated solution¹⁶⁴ or adding a poor solvent.^{165,166} It has been demonstrated that the ordering of P3HT in solution significantly improves the crystallinity of spin coated thin films and provides good pathways for charge transport due to their directional extension of inter- and intra-molecular π conjugation.¹⁶⁷

In the present work, we have studied the phase separation in blends of P3HT and semicrystalline polyethylene oxide (PEO). Self-assembled P3HT nanowires were produced in solution which ensures good crystallinity of the semiconducting component even in the presence of the PEO matrix. The PEO matrix crystallizes during the one-step spin coating process, while P3HT nanowires are driven to aggregate at both the air and the substrate interfaces. The crystallization-induced phase segregation of crystalline-crystalline blends provides a method to construct layered structures. FETs fabricated with the system demon-

strate good electronic performance comparable to pure P3HT devices.

7.2 Experimental Methods

7.2.1 Thin Film Preparation

P3HT (Sepiolid P200) nanowires were prepared according to Kim's method.¹⁶⁶ A P3HT solution was first prepared by dissolving regioregular P3HT in a chlorobenzene (CB)/acetonitrile (ACN) (volume ratio: 10/1) cosolvent system at a total concentration of 10 mg/ml. The obtained solution was treated with ultrasonication at room temperature for 3 min, and kept under ambient conditions for 3 hrs to allow P3HT assembly in the solution. The P3HT in CB/ACN solution displayed an obvious color change from orange in its fully dissolved state to dark red after cooling to room temperature and aging for 3 hrs.

A PEO solution was prepared in the same CB/ACN cosolvent at a concentration of 10 mg/mL. P3HT and PEO were blended by mixing the respective stock solutions at different P3HT contents (20 wt%, 33 wt%, 50 wt%, and 75 wt%). P3HT/PEO films were prepared by spin coating of these solutions at 2000 rpm. The samples for XRD measurements were spin coated onto bare Si substrates. The morphology of thin films was studied by AFM. Films for SEM were plasma etched for 30 s and rinsed with ethanol to selectively remove PEO. A Veeco (Bruker) Dimension 3100 system was used in the tapping mode for AFM imaging. A P Diff2 Gen 3 X-ray diffractometer was used for XRD. UV-visible absorption spectroscopy was performed using a Hewlett Packard 8453 UV-vis spectrophotometer. SEM was performed on a LEO 1530 system operating at 5 kV acceleration voltage.

7.2.2 Transistor Fabrication

We use thin film FETs to investigate the electrical characteristics of P3HT/PEO blend systems. A typical FET consists of source and drain electrodes, a semiconductor layer, a dielectric layer and a gate electrode. In the present work, field-effect transistors with the bottom-gate-bottom-contact configuration (Figure 7.1) were fabricated using heavily doped n-type Si wafers with 300 nm thick silicon dioxide as the gate electrodes. The capacitance of 300 nm-thick SiO₂ is $1.15 \times 10^{-8} \text{ Fcm}^{-2}$. The gold source and drain electrodes (100 nm on 2 nm

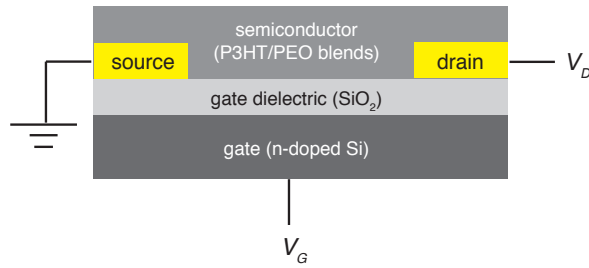


Figure 7.1 Schematic illustration of a bottom-gate bottom-contact FET

adhesion layer of Cr) were evaporated through a shadow mask. The channel length (L) and width (W) were fixed to 20 μm and 1000 μm , respectively. Prior to film deposition, the substrates were cleaned by 10 min oxygen plasma etching and exposed to a hexamethyldisilazane (HMDS) vapor for 3 hrs. Polymer films were then spin coated at 2000 rpm onto the substrates, and left in vacuum for 5 hrs to remove the residual solvent. All device fabrication and device measurements were performed in a glovebox.

7.2.3 Measuring Device Characteristics

The FETs described in the present work are based on the p-type semiconducting polymer P3HT, thus positively charged holes are the majority charge carriers. Applying a negative gate voltage (V_G) will result in the accumulation of charge carriers at the semiconducting-dielectric interface to form a conducting channel. The amount of the accumulated charge in the channel is proportional to V_G . When there are enough free carriers accumulated at the interface, the transistor turns on. During operation, the source electrode is usually grounded while the drain electrode has an applied bias (V_D). The electric field between source and drain electrodes induces the flow of charge carriers in the channel.

Typical output characteristics of the source-drain current (I_D) is plotted as a function of V_D at different V_G (Figure 7.2a). The transfer characteristics shows I_D as a function of V_G at constant V_D (Figure 7.2b). When V_G exceeds the threshold voltage V_{Th} , a channel of mobile charge carriers accumulates and the conductivity in the channel rises. Charge carriers are free to flow in the channel at V_D , and their local concentration is determined by the electric field imposed by both V_G and V_D . The current-voltage characteristics can be derived through application of the gradual channel approximation. A more detailed description can be found in the book "Physics of semiconductor devices".⁴

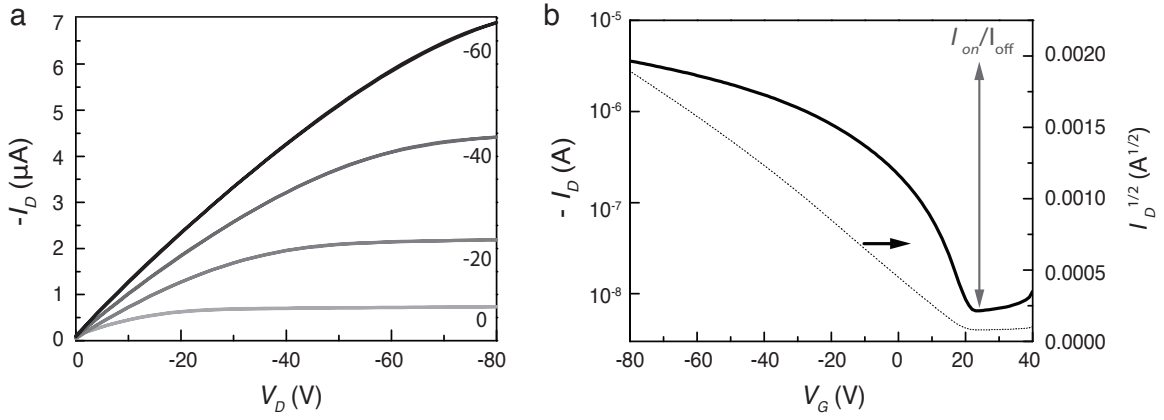


Figure 7.2 Example transistor characteristics of a P3HT device a) Output characteristics at $V_G = -60$ V, -40 V, -20 V, and 0 V. b) Transfer characteristics in the saturation regime ($V_D = -60$ V). The on-off ratio is the ratio of I_D in the on and off states of the transistor.

When $V_D \ll V_G$, the transistor operates in the linear regime because of the linear relationship between I_D and V_D , which can be expressed as

$$I_D = \frac{WC_i}{L} \mu (V_G - V_{Th}) V_D, \quad (7.1)$$

where C_i is the capacitance of the dielectric, W is the channel width, L is the channel length, and μ is the charge carrier mobility.

When $V_D \geq (V_G - V_{Th})$, the channel gets pinched off. A depletion zone may be created near the drain electrode if the local potential is below V_{Th} . The depletion zone becomes larger with increasing V_D . Since the pinch-off point remains at V_{Th} , I_D becomes independent of V_D , causing the current to saturate. A space-charge limited current flows from the pinch-off point to the drain electrode. This is the saturation regime, in which I_D is expressed as

$$I_D = \frac{WC_i}{2L} \mu (V_G - V_{Th})^2. \quad (7.2)$$

V_{Th} can be estimated from the intercept of the linear fit of a transfer curve in saturation when plotted as $\sqrt{I_D}$ vs. V_G , as shown in Figure 7.2b. The field-effect μ in the saturation regime can be determined from the first derivative of $\sqrt{I_D}$ vs. V_G

$$\mu = \frac{2L}{WC_i} \left(\frac{\partial \sqrt{I_D}}{\partial V_G} \right)^2. \quad (7.3)$$

The on-off ratio is given by the ratio of the currents when the transistor is turned on and off, which can be estimated from a transfer curve in the saturation regime on a log-scale (black line in Figure 7.2b). I_{on} is defined as the value where the curve reaches a plateau and I_{off} is the lowest current measured.

FETs were measured using Keithley 4200 and 236 source/measure units and Labview software at room temperature in a glovebox.

7.3 Results and Discussion

7.3.1 Self-assembly of P3HT in Solution

We first investigated the effect of the addition of a dipolar solvent on the self-assembly of P3HT. The self-assembly of P3HT is driven by the π - π interactions between thiophene backbones, forming an ordered supermolecular stack. By changing the solvent solubility or polarity, homogeneous P3HT nanowire suspensions were obtained. Results show that the addition of ACN effectively promoted the aggregation of P3HT to form nanowire structures.

The variation of P3HT molecular order as a function of ACN concentration in CB was studied by UV-Vis absorption spectroscopy (Figure 7.3a). The spectrum of the pristine P3HT/CB solution only shows a single peak at $\lambda = 455$ nm, attributed to the intrachain π - π^* transition of P3HT, which indicates that the polymer chains are molecularly dissolved in solution. Upon addition of ACN, a new absorption peak at 610 nm emerges and its intensity increases with an increasing ACN concentration. The new absorbance peak is usually attributed to the increase in the effective conjugation length of P3HT chains, which confirms the formation of highly ordered P3HT aggregates in solution. Films deposited from such solutions show interconnected networks of P3HT nanowires with width of 10-20 nm and length of several microns, as shown in the AFM topography and phase images (Figure 7.3b). Also, the self-assembled P3HT nanowires are highly crystalline as evidenced by the (100), (200), and (300) diffraction peaks in the XRD spectrum (Figure 7.3c). The observed (100) peak suggests that P3HT molecules adopt an edge-on orientation with respect to the substrate, which is beneficial for FET devices.

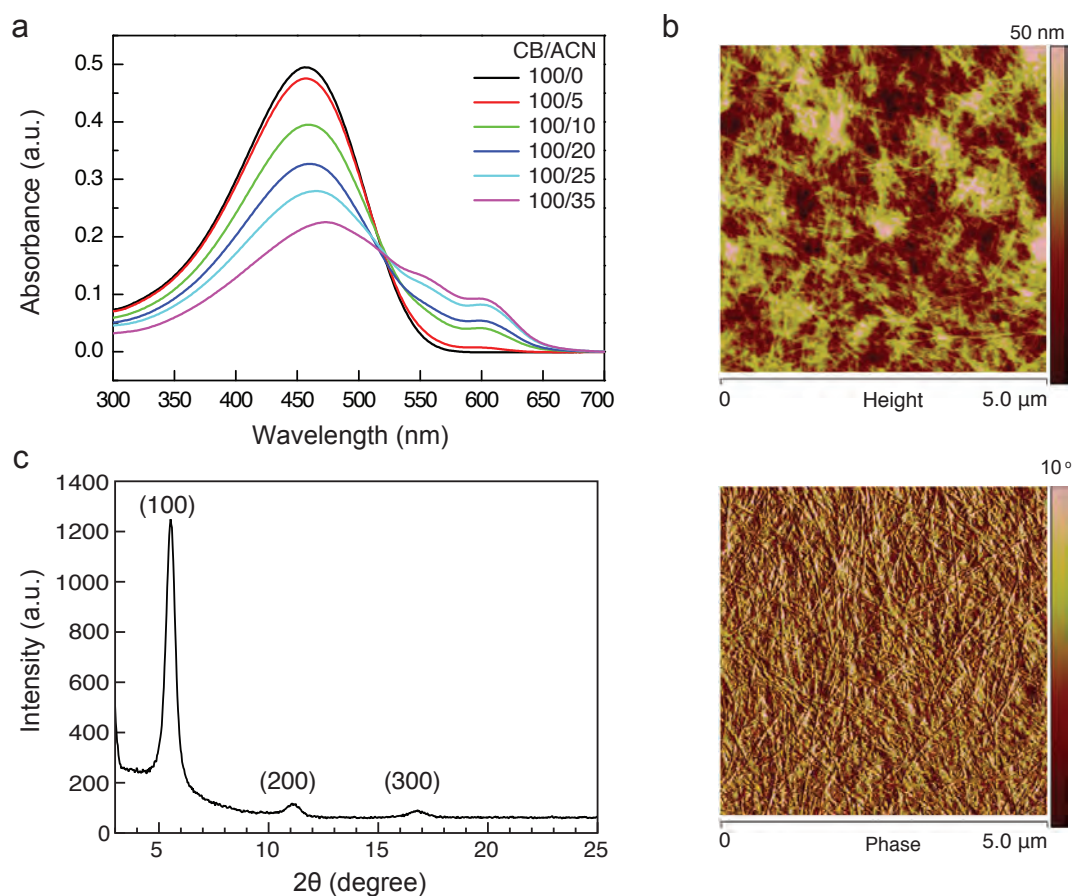


Figure 7.3 a) UV-vis spectra of P3HT in CB solutions (2 mg/mL) at various ACN concentrations. b) AFM images of P3HT nanowires obtained from CB/ACN solutions. c) XRD profile confirming the high crystallinity of P3HT in the thin film.

7.3.2 Morphology of P3HT/PEO Blends

The prepared P3HT nanowire solutions were blended with PEO at different weight ratios and the morphology of resulting blend films was investigated by AFM, as shown in Figure 7.4. A typical spherulitic morphology with sizes of about 100 μm was observed when P3HT was added to PEO at 10 wt% (Figure 7.4a), which confirms the crystallization of the PEO matrix. We consistently observed a continuous network of P3HT nanowires at the top surface of films for a variety of P3HT contents. It is possible that P3HT nanowires have been pushed out of the PEO crystalline domains followed by segregation at the grain boundaries or interfaces.

In contrast, lateral phase-separated structures were observed in blend films prepared from a good solvent (CB solution without P3HT aggregation), as shown in Figure 7.5. At either

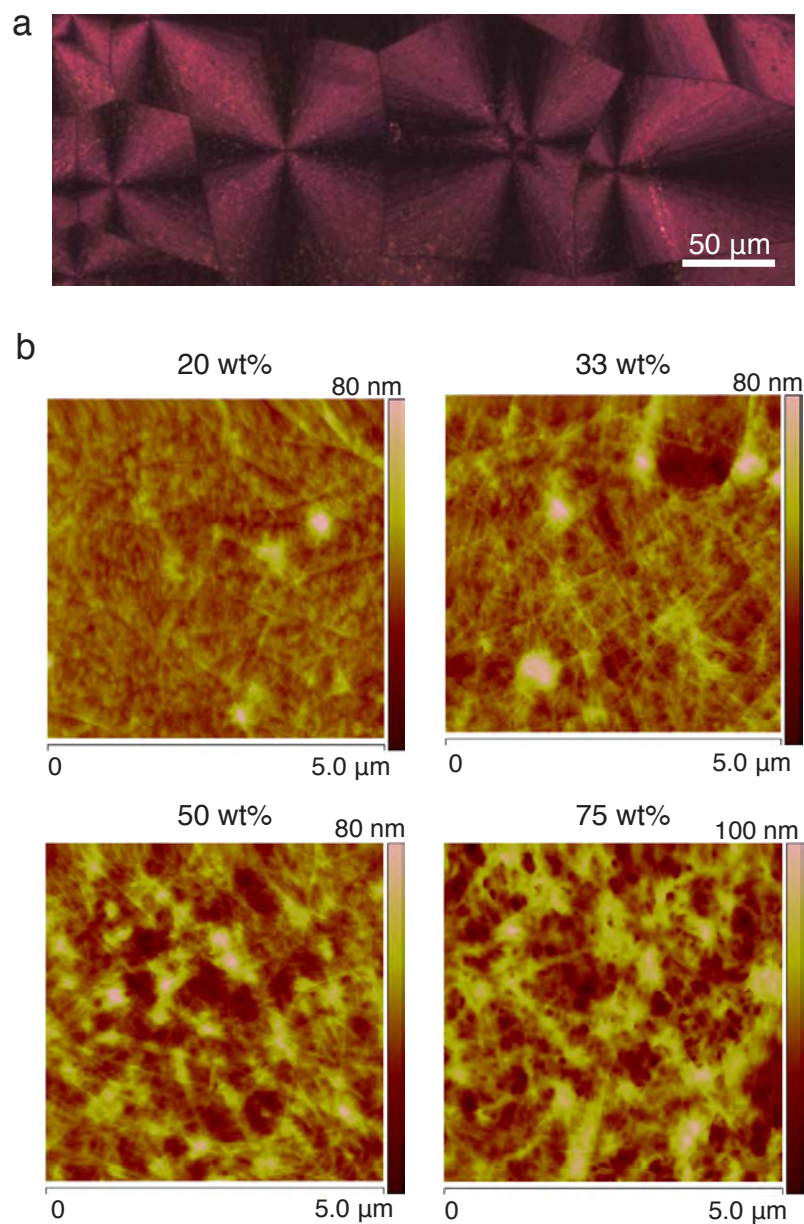


Figure 7.4 Morphology of P3HT/PEO blend films prepared from CB/ACN solutions. a) POM image of a blend film with 10 wt% P3HT. b) AFM images of blend film with P3HT content of 20 wt% , 33 wt%, 50 wt%, and 75 wt%.

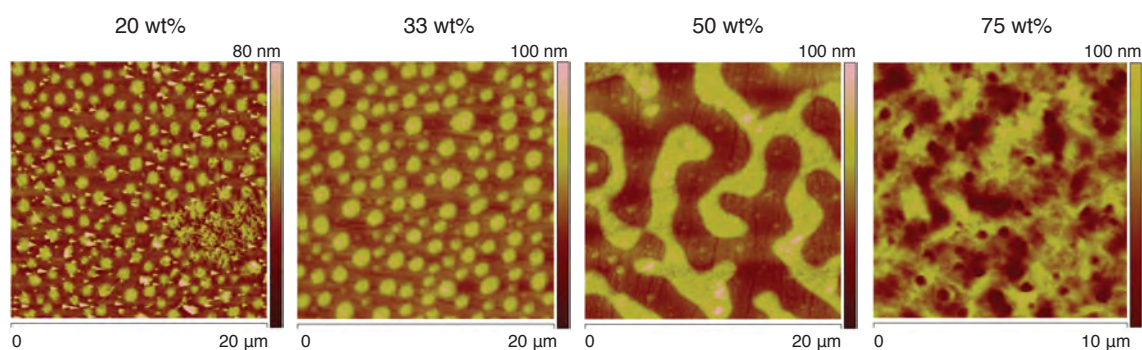


Figure 7.5 AFM images of P3HT/PEO blend films prepared from CB solutions with P3HT content of 20 wt%, 33 wt%, 50 wt%, and 75 wt%.

low or high P3HT content, the blend films typically formed a morphology with minor component domains dispersed within the major component phase. For instance, with 20 wt% and 33 wt% P3HT, isolated droplet-like P3HT domains were dispersed in the PEO matrix. Large scale phase separation between P3HT and PEO due to spinodal decomposition was observed at the comparable blending ratio of 50 wt% P3HT. The lateral phase separation indicates the strong incompatibility between the two components.

The use of polymer blends in field-effect transistor applications relies critically on the morphology of the active layer/gate dielectric interface, as charge transport happens in this interfacial layer. AFM surface morphology studies of the P3HT/PEO films with self-assembled nanowires suggest a vertically segregated microstructure in the system. Here, we have further investigated the morphology at the interface in contact with the gate dielectric. The films were plasma etched down to thicknesses of about 20 nm to expose the bottom layer. Confirmation of segregation of the P3HT nanowires at the bottom was obtained using SEM, as shown in Figure 7.6. The density of the P3HT nanowire distribution increases with increasing P3HT content, which is consistent with that on the top surface. This implies that P3HT nanowires have first solidified from solution during spin coating, while PEO remains dissolved due to its greater solubility in both solvents.

It is clear that the vertical segregation occurred in blend films with P3HT on both the top and the bottom. The multiple phase separation processes in these crystalline-crystalline blends of P3HT and PEO involve the following steps (Figure 7.7): 1) P3HT self-assembles to crystalline aggregates in solution, which ensures the priority of P3HT crystallization during film formation; 2) P3HT solidifies to form nanowires while PEO remains highly solvated in

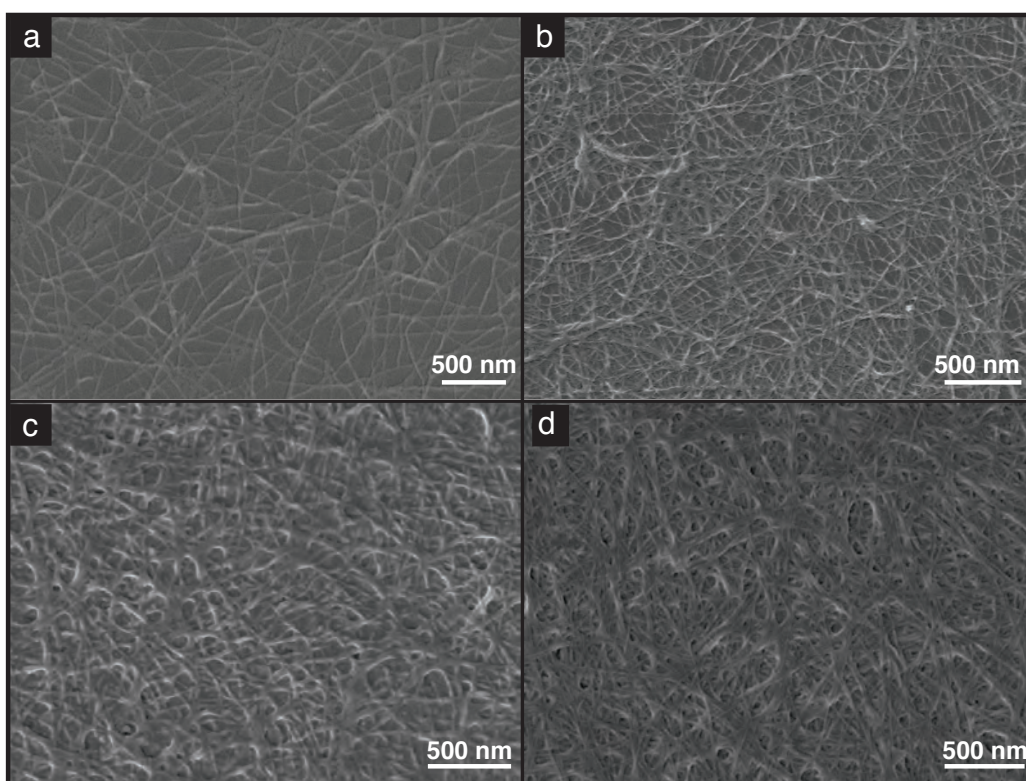


Figure 7.6 SEM images of bottom surface after selectively removing PEO from P3HT/PEO blend films prepared from CB/ACN solutions with P3HT content of a) 20 wt% , b) 33 wt%, c) 50 wt%, and d) 75 wt%.

solution; 3) The PEO matrix starts to crystallize, which segregates P3HT nanowires from the PEO crystalline domains to grain boundaries and interfaces. The complex crystallization and phase separation processes result in the formation of the layered microstructures with continuous P3HT nanowire networks at the interfaces.



Figure 7.7 Schematic illustration of the film formation process of P3HT and PEO blends.

7.3.3 Field-Effect Transistor Performance

We have investigated the electronic performance of FET devices made from P3HT/PEO blends in the bottom-contact bottom gate FET configuration with gold as source and drain electrodes. Such FET devices are known to be capable of injecting and transporting holes through P3HT networks. As shown in Figure 7.8a, the saturation I_D of P3HT/PEO (10/90)

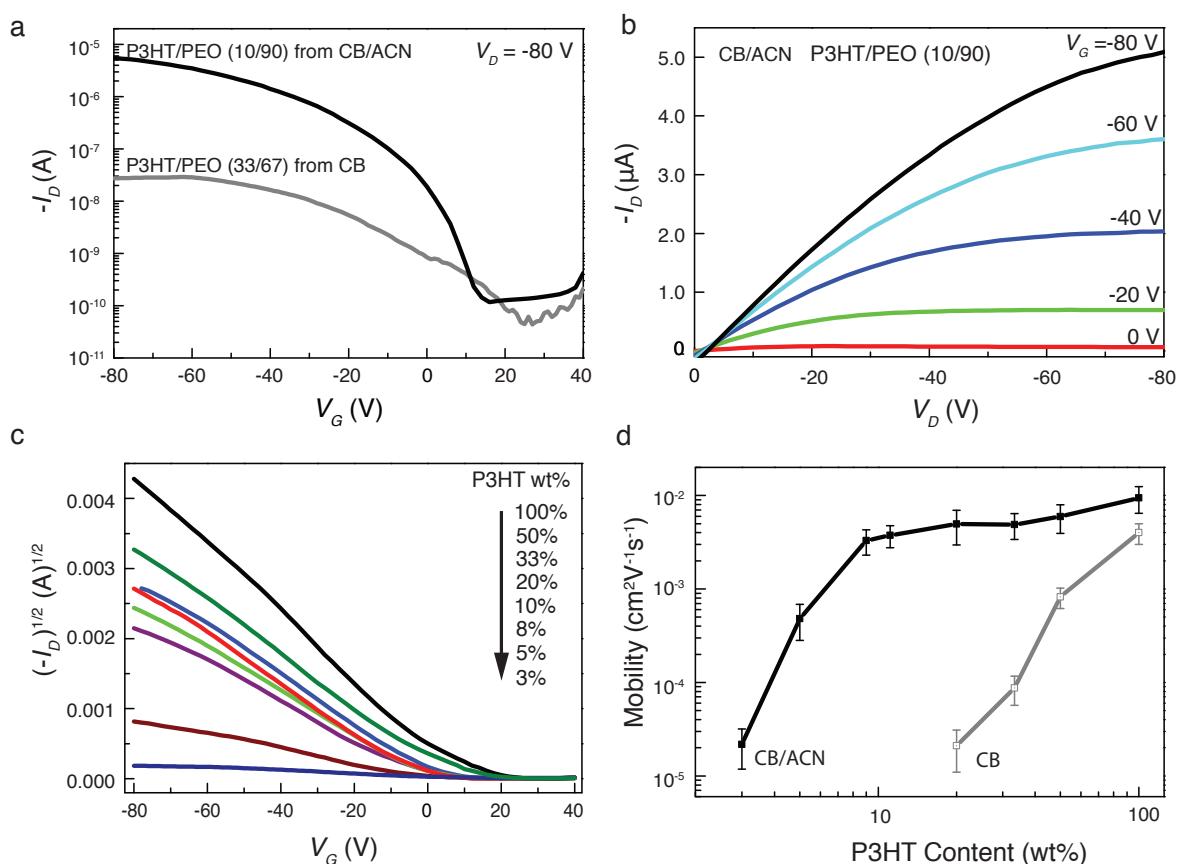


Figure 7.8 Field-effect transistor performance of P3HT/PEO blends obtained from CB/ACN and CB solutions. a) Typical transfer characteristics of devices fabricated with P3HT/PEO(10/90) from a CB/ACN solution, and P3HT/PEO (33/67) from a CB solution. b) Output characteristics of a device based on a P3HT/PEO (10/90) blend from CB/ACN solution. c) Plot of $\sqrt{I_D} \sim V_G$ for P3HT/PEO blends with a decreasing P3HT content from CB/ACN solutions. d) Average field effect mobility measured in the saturation regime as a function of P3HT content in the blend.

from CB/ACN solution was about 10^3 times higher than that of P3HT/PEO (33/67) from CB solution even though its P3HT content was much lower. Typical I_D vs. V_D curves at various V_G values for FETs prepared from CB/ACN solutions of P3HT/PEO (10/90) are shown in Figure 7.8b. The P3HT/PEO (10/90) device displayed a high field-effect mobility of $9 \times 10^{-3} \text{ cm}^2\text{V}^{-1}\text{s}^{-1}$, ON-OFF ratios of 10^4 , and good charge injection behavior at a low V_D despite a high content of insulating PEO matrix. This is in strong contrast to the devices prepared from the CB solutions.

The average field-effect mobility of each transistor was calculated in the saturation regime ($V_D = -80$ V) by plotting $\sqrt{I_D}$ vs. V_G (Figure 7.8c) and fitting Equation 7.3 to the data. The dependence of the field-effect mobility on P3HT content of the films prepared from CB/ACN was compared with that from CB solutions (Figure 7.8d). The mobility of

neat P3HT devices prepared from CB/ACN and CB solutions are $9 \times 10^{-3} \text{ cm}^2\text{V}^{-1}\text{s}^{-1}$ and $4 \times 10^{-3} \text{ cm}^2\text{V}^{-1}\text{s}^{-1}$, respectively. For the reference samples (prepared from CB solutions), we observed a monotonous decrease in field-effect mobility with increasing PEO content from $4 \times 10^{-3} \text{ cm}^2\text{V}^{-1}\text{s}^{-1}$ for a film with 100 wt% P3HT to $2 \times 10^{-3} \text{ cm}^2\text{V}^{-1}\text{s}^{-1}$ for blends with 20 wt% P3HT, which is in agreement with the tendency found in P3HT/PS blends in the literature.¹⁶² In contrast, the P3HT/PEO blends exhibited a nearly unchanged performance with P3HT content as low as 10 wt% ($\mu = 4 \times 10^{-3} \text{ cm}^2\text{V}^{-1}\text{s}^{-1}$) when prepared from CB/ACN solutions.

It is reasonable to relate the difference in the electronic performance of these blends to their striking distinctiveness in film morphology. The good mobility of P3HT/PEO films obtained from CB/ACN solutions is derived from the formation of a layered structure with networks of P3HT nanowires at the substrate interface. On the other hand, micro-scale lateral phase separation in films obtained from CB solution significantly deteriorates the transistor performance.

7.4 Conclusion

We have demonstrated the use of P3HT nanowires in double-crystalline P3HT/PEO blend systems in FETs. The film morphology can be controlled by first inducing the self assembly of P3HT followed by the vitrification of the PEO matrix, inducing a layered structure instead of spinodal decomposition for non-assembled P3HT with PEO. The prepared P3HT nanowires showed good molecular order, which is beneficial for charge transport. Charge carrier mobility of the P3HT/PEO films is maintained down to 10 wt% P3HT due to a good connectivity of the semiconductor component, while the lateral phase separated system showed deteriorated electrical performance.

Chapter 8 Biomimetic Hierarchical Structures to Mimic Gecko Adhesion

Superior yet reversible adhesion found in nature on pads of biological adhesives such as geckos toe-pads enables them to conform to any surface profile at several length scales, while maintaining structural integrity and wear-resistance. The intricate structural hierarchy developed on gecko pads is responsible for their incredible adhesive capability. Although considerable progress has been made with mimic fibrillar adhesives, most of the benchmark properties of natural fibrillar adhesives are still unsurpassed. The fabrication of intricate structures, closer in design and performance to those in nature, is a complex task. In this study, we demonstrated the feasibility of hierarchical nanostructures based on vertically aligned carbon nanotubes implanted onto polymer pillars in the design of efficient synthetic adhesives closely mimicking gecko-feet abilities.

8.1 Introduction

Geckos are well known for their extraordinary adhesive locomotion system that allows them to walk freely on vertical and inverted substrates. Little was understood about gecko toe-pads until the late nineteenth century when microscopic hairs on the pads were first noted.¹⁶⁸ Two fundamental characteristics of the gecko locomotion system, the hierarchically arrayed fibrils responsible for generating adhesive forces and the digital hyperextension that makes possible the rapid attachment and detachment, have been studied in detail over the last years. These studies have created opportunities for the fabrication of biomimetic adhesives, but there are still many challenges to be resolved before structures with gecko

functionality can be made with artificial materials.

8.1.1 Structural Features of a Gecko Foot

Gecko toes consist of arrays of millions of angled, branched, hair-like setae formed of stiff, hydrophobic β -keratin as shown in Figure 8.1a. The macroscale lamellae, soft ridges ~ 1 - 2 mm in length, are capable of compressing against and making contact with rough bumpy surfaces (Figure 8.1b). Microscale setae form arrays on the lamellae. These setae are typically 30 - 130 μm in length and 5 - 10 μm in diameter (Figure 8.1c, d), and each seta branches into spatulae with diameters of 100 - 200 nm (Figure 8.1e). The flat tips of these spatulae are approximately 200 - 300 nm in width, 500 nm in length and 10 nm in thickness.^{169,170} This hierarchical system on gecko toes is made of β -keratin, a rigid protein with a bulk Young's modulus of ~ 1.6 GPa,¹⁷¹ but setae arrays are predicted to have an effective elastic modulus in the range of 100 kPa, thus they behave with great compliance and flexibility.¹⁷²

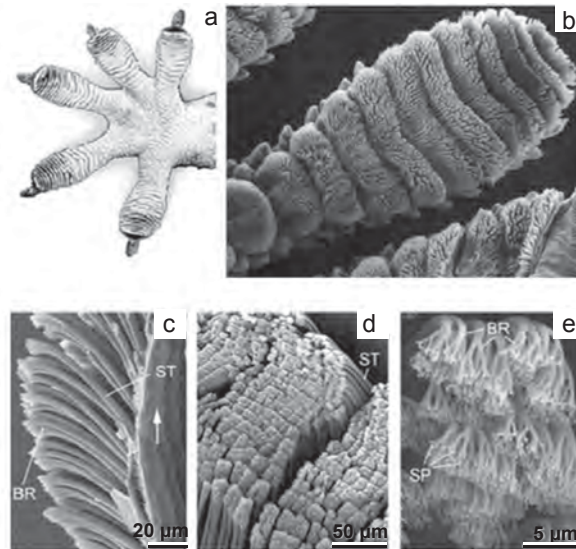


Figure 8.1 The hierarchical structures of a gecko foot. a) a Tokay gecko foot; b) a gecko toe; c), d) the setae; e) the spatulae; ST setae, SP spatula, BR branch¹⁷³

Gecko's hairy adhesive pads can easily adapt to the topography of rough surfaces and achieve intimate contact due to the bending and stretching of the setae and the flexibility of the very thin setae end spatulae. The hierarchically structured gecko setae can achieve greater contact than a flat pad with a rough surface, with lamellae adapting to macroscale undulations and setae conforming to microscale roughness.

8.1.2 Properties of Gecko Adhesion

Mechanisms of Gecko Adhesion

While the hierarchical setae structures of geckos have been well studied, the underlying mechanism for such exceptional adhesion properties is still under debate. Numerous conjectures on the mechanism have arisen including glue, suction, electrostatics, interlocking, and intermolecular forces. Two hypotheses, van der Waals interactions and capillary effects, have been most investigated.

The intermolecular van der Waals forces are considered to be the main contribution to the adhesion mechanism for gecko toe-pads. Autumn *et al.* first reported the direct measurements of the single setal adhesive force which supports the van der Waals hypothesis.¹⁷⁴ The van der Waals mechanism implies that the adhesion of gecko setae depends on the nanostructure rather than the surface chemistry of the setae. Measurements with live geckoes on different semiconductor surfaces showed similar adhesion forces regardless of hydrophobicity, which confirms that the van der Waals mechanism, rather than capillary effects, is the main contribution to gecko adhesion. This implies that gecko adhesion is material independent and therefore can be achieved by the fabrication of biomimetic structures with different materials.¹⁷⁵

Although most experimental results suggest that van der Waals forces are the dominant mechanism, recent research indicates that capillary forces can also contribute to gecko adhesion. The effects of capillarity on gecko adhesion were investigated with modeling by considering the Laplace force and surface tension force as well as the adhesion force for stiff solids.¹⁷⁶ The adhesion forces decrease with an increase in relative humidity, which is consistent with the single spatula experiment on substrates with varying hydrophilicity and as a function of air humidity.¹⁷⁷ The humidity effect was explained as a result of the change of the short-range interaction due to absorbed water between spatula and substrate. However, the moisture induced stiffness reduction of β -keratin was not taken into account as the change in material properties can also result in a higher pull-off force.¹⁷⁸ Therefore, the van der Waals forces remain the only empirically supported mechanism of adhesion in geckos.

Frictional Adhesion

Conventional frictional adhesion is governed by the Amontons' first law. The shear force (friction, F_{\parallel}) between two surfaces is proportional to the normal load (F_{\perp}) and the ratio is the coefficient of friction (μ) determined by: $F_{\parallel} = \mu F_{\perp}$. The dependence of gecko adhesion on the shear direction is shown in Figure 8.2.¹⁷⁹ When pressed against the natural curvature (non adhesive direction), the seta arrays do not adhere and instead exhibit a typical friction coefficient, $\mu = 0.3$. When dragged along their natural curvature (adhesive direction), adhesion develops but the force response violates Amontons' law. The relationship between the adhesive and the shear force is described by the 'frictional adhesion' model: $F_{\parallel} \geq F_{\perp}/\tan \alpha^*$ (α^* is the critical angle of detachment, approximately 30°) or approximately $F_{\parallel} \geq 2F_{\perp}$. This model defines the minimum shear load that can withstand a given adhesive force. The ratio of F_{\parallel} to F_{\perp} during actual gecko climbing was found to be ≈ 5 , suggesting that much greater shear forces are required to maintain adhesion.

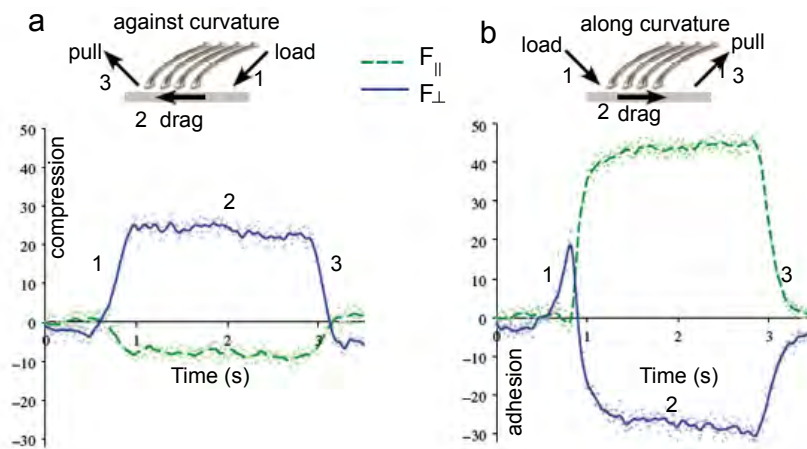


Figure 8.2 Shear and normal forces of gecko setal arrays on a glass surface during a load-drag-pull movement. The shear rate was controlled at $50 \mu\text{m/s}$. a) Setal arrays during shear against the curvature of the setal shafts exhibits Coulomb friction. The compression force F_{\perp} was higher by a factor of approx. 3 than the shear force F_{\parallel} . b) Setal arrays during shear along the curvature. The setal array was pulled into tension as the setal tips adhered. Adhesion was sustained during the $100 \mu\text{m}$ drag step.¹⁷⁹

The attachment and detachment of gecko setae are controlled mechanically by gripping and peeling of the toes. Depending on the angle between the spatulae pad and surface, both the friction force and normal adhesion of a single seta can be changed by more than three orders of magnitude. This behavior is related to the asymmetrical seta geometry which is beneficial for rapid switching between attachment and detachment.¹⁸⁰ Moreover, gecko

setae do not exhibit the adhesion or friction decrease characteristic of a transition from static to kinetic contact mechanics. Instead, friction and adhesion forces increase logarithmically, contradictory to macroscopic solids where these forces usually decrease at the onset of sliding.¹⁸¹ Thus, the frictional adhesion property of gecko toe-pads enables precise control over adhesion *via* friction, allowing strong attachment and easy removal.

Self-cleaning Property

Gecko setae have the self-cleaning property that they become cleaner with repeated use. Geckos with contaminated feet can recover their adhesion ability after a few steps on clean substrates. It is known that the lotus effect of nano-structured surfaces results in hydrophobicity and self-cleaning in the presence of water, whereas gecko can self-clean when dry. A contact mechanical model was used to calculate the force between a spherical dust particle and the wall and it is energetically favorable for particles to adhere to the surface rather than spatulae. Self-cleaning in gecko setae can occur when they meet three criteria: (1) they have smaller surface area than that of dirt particles, (2) they are made of non-tacky material, (3) they have low surface energy (equal or less than that of the wall). The model suggest that structures made of stiff materials with low surface energy are favorable to achieve gecko-like self-cleaning property.¹⁸²

8.1.3 Physical Principles for Adhesion of Fibrillar Structures

Gecko setae produce remarkable adhesive properties through their hierarchical fibrillar elements. Fibrillar structures can produce higher adhesion as a result of several mechanisms. 1) Extrinsic contribution from fracture mechanics: Due to energy dissipation in fibrils upon detachment, the crack propagation has to be re-initiated fibril by fibril. The spatial path for energy transfer upon unloading has been blocked by the fibrillar structure.^{183,184} 2) Adaptability to rough surfaces: fibers with high aspect ratio on gecko toes can easily deform without storing a large elastic energy.¹⁸⁵ 3) Uniform stress distribution: adhesion contacts below a critical size have been shown to develop a uniform stress distribution before pull-off.¹⁸⁶

The complexity of adhesion arises when the two surfaces are no longer flat and the elastic deformation factor becomes important. The Johnson, Kendall and Roberts (JKR) model com-

combines the effect of elasticity of spheres with work of adhesion in the case where the interaction distance is small and the attractive forces are large.¹⁸⁷ The force required to form a circular contact of radius a is given by

$$F_{\text{JKR}} = \frac{4E^*a^3}{3R} - \sqrt{8\pi E^*a^3\gamma}, \quad (8.1)$$

where E^* is the reduced elastic modulus

$$\frac{1}{E^*} = \frac{1 - \nu_1^2}{E_1} + \frac{1 - \nu_2^2}{E_2}, \quad (8.2)$$

with E_i the Young's modulus and ν_i the Poisson's ratio. The reduced radius R is defined as

$$\frac{1}{R} = \frac{1}{R_1} + \frac{1}{R_2}, \quad (8.3)$$

where R_i are the radii of the two spherical surfaces in contact. The theoretical pull-off force or adhesion F_c is given by

$$F_c = \frac{3\pi R\gamma}{2}, \quad (8.4)$$

where γ is the work of adhesion. The concept of "contact splitting" proposed by Arzt *et al.* applies the JKR model to living systems.¹⁸⁸ Assuming one spherical contact of radius R_0 is divided into N smaller contacts ($R = R_0/\sqrt{N}$) with identical apparent contact area, the pull-off force for simultaneous detachment of these N spheres will then rise by a factor of $N^{1/2}$

$$F_c = \frac{3\pi\sqrt{N}R_0\gamma}{2}. \quad (8.5)$$

Using this concept, the reduction in seta diameter is directly related to the increased overall adhesive force, which explains the observation that heavier animals exhibit finer adhesion structures.

8.1.4 Bioinspired Adhesive Structures

Based on the understanding of principles in gecko adhesion, biomimetic structures to achieve gecko-like adhesion should meet several structural requirements. The basic geometric parameters are summarized as: aspect ratios of 10-30 and 20-50 for fibril diameters

of 3~10 μm and 50~500 nm, respectively; a directional angle of the nanostructure is crucial for anisotropic adhesion properties. A material with a Young's modulus of 1~15 GPa, hydrophobic and high tensile strength to maximize micro/nano-hair density and to prevent matting.^{189,190} The spatulae shape also significantly influences the adhesion and the use of mushroom-type tips enhances adhesion by increasing the contact area as compared to that of a spherical or a simple flat heads.¹⁹¹⁻¹⁹³ Fabrication of multiscale structures can better mimic gecko's hierarchical setae arrays with enhanced compliance and adaptability to rough surfaces.

Recent advances in nanofabrication have created a great opportunity for generating gecko-inspired biomimetic fibrillar structures. Lithographic technologies have been utilized to make nanostructures with different geometries with high precision.¹⁹⁴ In the published literature, angled polymeric structures with high aspect ratios have been successfully fabricated as shown in Figure 8.3. Combining lithography and micromolding techniques enable the fabrication of hierarchical polymeric structures that mimic setae array (Figure 8.3f-h).

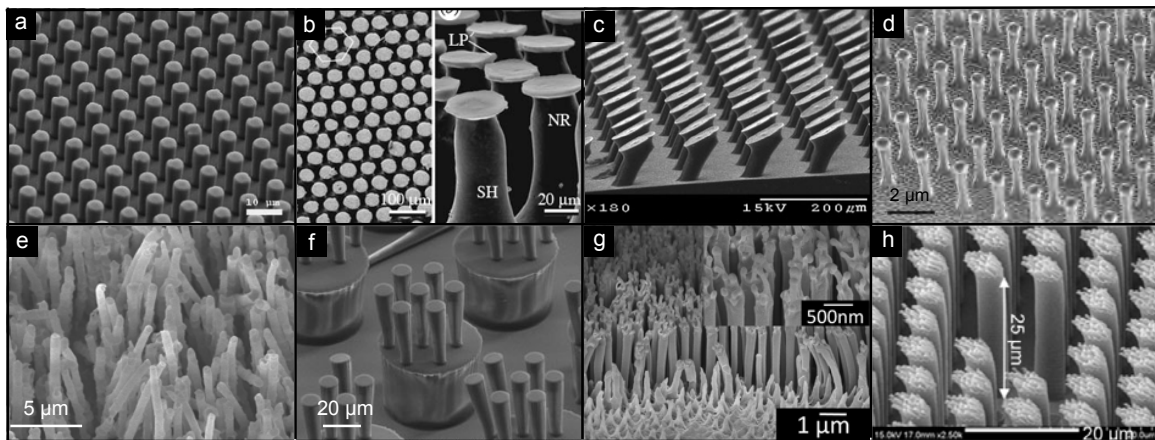


Figure 8.3 SEM images of bioinspired adhesives fabricated by different methods. a) SU-8 microstructures obtained by photolithography.¹⁹² b) Polysiloxane fibers by molding.¹⁹⁵ c) Angled fibers with mushroom tips obtained by dip coating SU-8 fibers with liquid polymer and pressing with a constant load during curing.¹⁹⁶ d) Polyimide fibers prepared by e-beam lithography.¹⁹⁷ e) polypropylene fibers obtained by molding from commercial polycarbonate membrane.¹⁹⁸ f) Hierarchical structures fabricated by layer-by-layer photolithography with SU-8.¹⁹⁴ g) Hierarchical polycarbonate hairs by molding using porous anodic alumina.¹⁹⁹ h) Hierarchical hairs by molding and UV-assisted capillary force lithography.²⁰⁰

Nanostructures with smaller features can produce higher adhesion forces according to contact splitting theory. Carbon nanotubes (CNTs) are one of the most suitable materials for making gecko adhesives as CNTs have outstanding structural properties, such as extremely

small radius, high mechanical modulus, and high aspect ratio.^{201,202} The highest shear adhesion for biomimetic gecko adhesives were achieved using vertically aligned multi walled carbon nanotubes (VA-MWNT) arrays with shear force of $\approx 100 \text{ N/cm}^2$ which is about 10 times of that of geckos (Figure 8.4a, b). These VA-MWNT arrays have a straight body segment with curly entangled ends. The strong shear adhesion comes from the shear-induced alignment of the entanglements of the nanotubes (Figure 8.4c).²⁰³ To replicate the multiscale structures of setae and spatulae, micropatterned VA-MWNT were fabricated and four times higher shear adhesion (36 N/cm^2) than that of the gecko foot was obtained under optimized pattern geometry. Even though CNT-based gecko adhesives have significantly higher adhesion strength than polymer-based adhesives, these materials require high preload, up to $\approx 100 \text{ N/cm}^2$. Under strong loading, CNTs have shown a permanent deformation either in random directions for normal loading or along the direction of shear loading which deteriorates the repeatability.^{201,202,204,205}

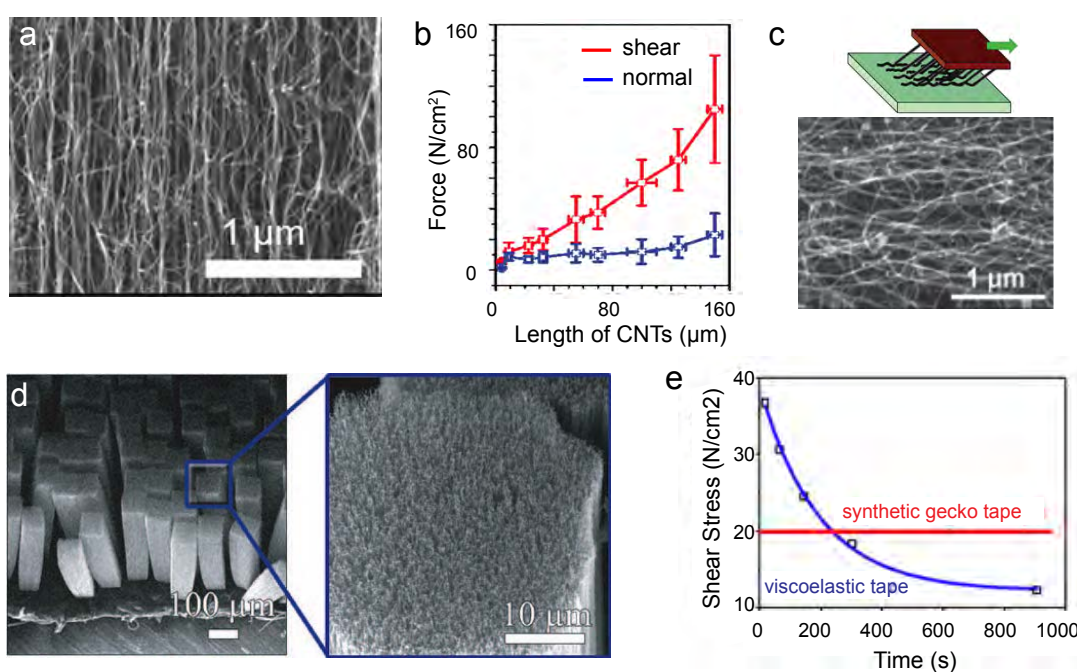


Figure 8.4 Examples of carbon nanotube-based synthetic gecko adhesives. a) SEM images of vertically aligned multi walled carbon nanotubes (VA-MWNT). b) Nanotube length-dependent adhesion forces of VA-MWNT attached to glass slides with a preloading of 2 kg. The sample size is $4 \times 4 \text{ mm}^2$. c) top view of VA-MWNT after shear adhesion measurements which shows the shear force stretching nanotubes.²⁰³ d), e) SEM images of micropatterned VA-MWNT arrays and the time-dependent shear stress. The synthetic gecko tape supports 20 N/cm^2 shear stress over a period of 8~12 hrs. In contrast, the force for a viscoelastic Scotch tape shows time-dependence decrease.²⁰⁶

In summary, biomimetic fabrication of fibrillar structures has excited much interest over the last years, however, no artificial structure has been reported that would match the gecko surface in reversible adhesion performance, robustness and durability. Achieving optimal high adhesive performance in bio-inspired artificial analogues requires designed hierarchical morphologies with an accurate balance of the relevant structural factors, including aspect ratio, dimensions, contact angle and shape of fibrillar structures. Furthermore, mechanical properties of the materials used for fabricating the biomimetic structures have a considerable impact on the fibrillar packing density, structure robustness and consequently the adhesive performance.

Synthetic polymeric multilevel structures have weak mechanical stability which limits the potentially obtainable aspect ratio. CNTs on the other hand, provide a particularly promising material to fibrillar adhesives due to their exceptional high aspect ratio and unique properties. The self-organized growth of such nanotubes and their high aspect ratio has not yet been combined with other structure formation process towards a multi-level hierarchical design. Here we provide a method to fabricate hierarchical nanostructures based on CNTs on top of polymer pillar arrays that closely mimic gecko toe pads. With the structural similarity to natural gecko foot hairs, the hierarchical pillar arrays (HPAs) show good adhesion properties with shear stresses up to 7.8 N/cm^2 . Notably, we obtain increased adhesive forces from the multi-scale nanostructures against rough surfaces, caused by the ability of the hierarchy to compensate roughness at several length scales. Moreover, an asymmetric geometry of nanohairs was introduced during the force measurement, providing a structure further resembling gecko's angled spatular tips.

8.2 Experimental Methods

SU-8 Pillar arrays (PAs) by Photolithography

Si wafers were cleaned in piranha solution (3:1 $\text{H}_2\text{SO}_4/\text{H}_2\text{O}_2$) and rinsed with deionized water. The resulting wafers were transferred into a cleanroom, and blown dry by a snow jet before lithographic processing. SU-8 microstructures were photo-lithographically patterned onto Si wafers using an MJB4 mask aligner. A Hoya UV34 filter was used to cut off

wavelengths below 340 nm during the irradiation step. SU-8 2000.5 was first spin coated onto the dried wafer at 3000 rpm for 1 min, followed by a soft bake of 1 min at 65 °C and 1 min at 95 °C. The SU-8 films were then flood exposed for 1 s, and hard baked for 1 min at 65 °C and 1 min at 95 °C. This thin layer of cross-linked SU-8 film improved the adhesion of high aspect ratio SU-8 pillars on substrates in the following photolithography step. Photoresist SU-8 2025 was then spin coated at 1500 rpm onto the prepared substrates. The specific processing parameters for the following lithography step were: 1) soft bake: 3 min at 65 °C and 10 min at 95 °C; 2) exposure 10 s; 3) hard bake 1 min at 65 °C and 6 min at 95 °C; 4) develop 6 min with propylene glycol monomethyl ether acetate (PGMEA, SU-8 developer).

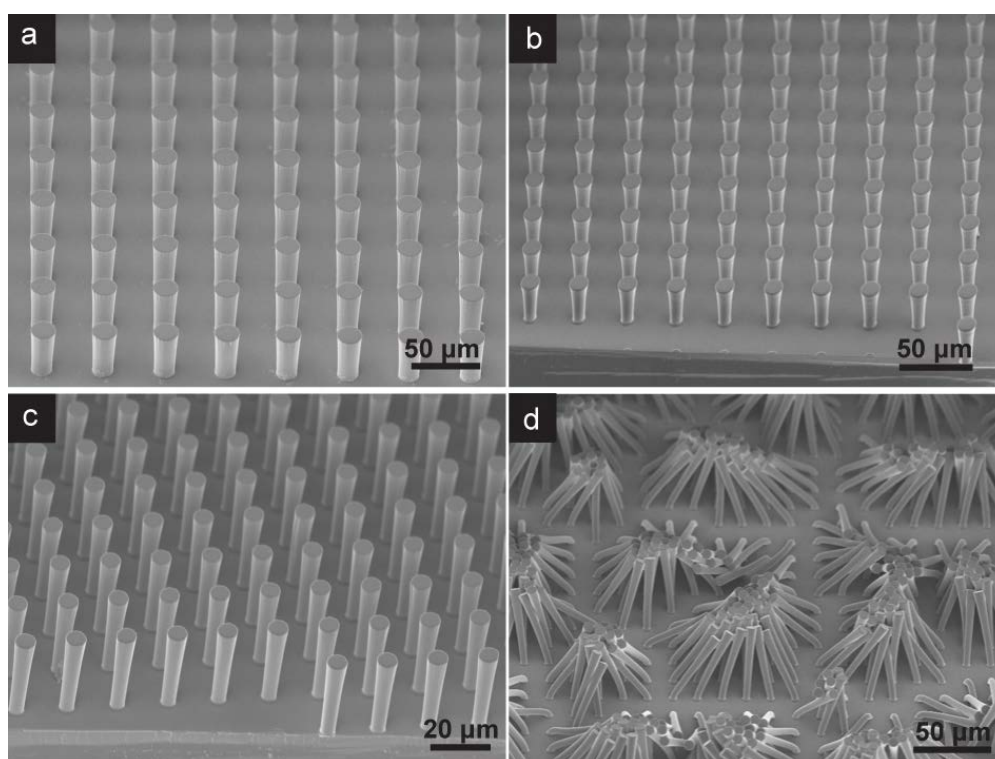


Figure 8.5 SEM images of SU-8 pillar arrays (PAs) with different aspect ratios of a) $f = 2.5$, b) $f = 5$, c) $f = 10$, d) $f = 15$.

The area covered by the SU-8 pillar arrays (PAs) was $1 \times 1 \text{ cm}^2$. SU-8 PAs were arranged on a square lattice with lattice constant of $a = 20 \mu\text{m}$, $40 \mu\text{m}$, $45 \mu\text{m}$ and diameters of $d = 5 \mu\text{m}$, $10 \mu\text{m}$, $20 \mu\text{m}$ and a height of $h = 50 \mu\text{m}$, yielding aspect ratios (f) of 2.5, 5, and 10, respectively. Pillars with higher aspect ratios ($f = 15$) could be fabricated but collapsed due to self-matting after air drying (Figure 8.5).

Fabrication of Carbon Nanotube Forests

Vertically aligned multi-walled carbon nanotube forests (CNTFs) were grown by thermal chemical vapor deposition at 650 °C in 200:500:10 sccm Ar:H₂:C₂H₂ at atmospheric pressure, from sputtered Al₂O₃ (10 nm)/Fe (1 nm) films supported on Si wafer substrates. The samples were transferred in air between the catalyst layer depositions before being loaded into the 2 inch diameter quartz tubing of the CVD furnace (Carbolite). Subsequently, the samples were heated up to 650 °C under a 1000 sccm flow of Ar, annealed for 3 min in 200:500 sccm Ar/H₂, and then 10 sccm of C₂H₂ were added to start CNT growth. The CNT length (20 μm) was controlled by the growth time of 3 min. The samples were cooled to room temperature in Ar atmosphere. CNTFs were fabricated by Bingan Chen from the Department of Engineering, University of Cambridge.

Transferring CNTs onto SU-8 PAs

A thin layer of polyvinyl acetate (PVAc) film was spin coated on top of the SU-8 PAs. CNTs were transferred to the SU-8 pillars by an imprinting process. The overall assembly comprised of the SU-8 pillars and the flipped over Si substrate covered with CNTFs was annealed at 100 °C and 5 MPa pressure for 15 min. Following this, the set-up was quenched to ambient temperatures and the imposed substrate was lifted-off, resulting in the solidification of the PVAc layer and the successful transfer of the CNTFs.

Adhesion Measurements

Adhesive forces were measured using force transducer with a 2D bending beam system. The motor movements and force recording were synchronized by a Lab-VIEW program that includes a normal force feedback mechanism. The force sensors were calibrated for different lever arm lengths by applying milligram weights and defined displacements. The force sensor had a stiffness of 41 N/m and resolution of less than 0.1 mN. Shear adhesion forces were measured using sliding experiments.

The samples were brought into contact with the spherical probe in the normal direction for 10 s with a predefined normal force of 0.5 mN, followed by the tangential displacement of the probe and final retraction from the measured surface. Sliding movements were per-

formed for 40 s with a velocity of 100 $\mu\text{m/s}$ covering 4 mm distance while the normal force was kept constant via the force feedback loop. After sliding, the probe was put on hold for 10 s followed by retraction at a speed of 100 $\mu\text{m/s}$ for 10 s. A glass sphere with diameter of 1 mm was glued to the free end of the bending beam and used as the smooth probe. The glass sphere was treated by hexamethyldisilazane (HMDS) vapor phase silanization at 100 $^{\circ}\text{C}$ for 16 hrs. The water contact angle on flat glass coated with HMDS was $\theta = 110^{\circ}$. A stainless steel sphere with diameter of 1.5 mm was etched in H_2SO_4 for 3 hrs to create submicron roughness and then used as a rough probe (Figure 8.6). The surface roughness was $R_a = 200$ nm and $RMS = 250$ nm as measured by AFM. Oscillation force measurements were performed with repeated shearing at a speed of 100 $\mu\text{m/s}$ for 25 cycles using the smooth glass probe. Normal adhesion forces were measured using the indentation procedure without the shearing/sliding step. Typically, the probe indented the sample with a predefined normal force of 0.5 mN for 40 s and was then retracted until no force could be measured.

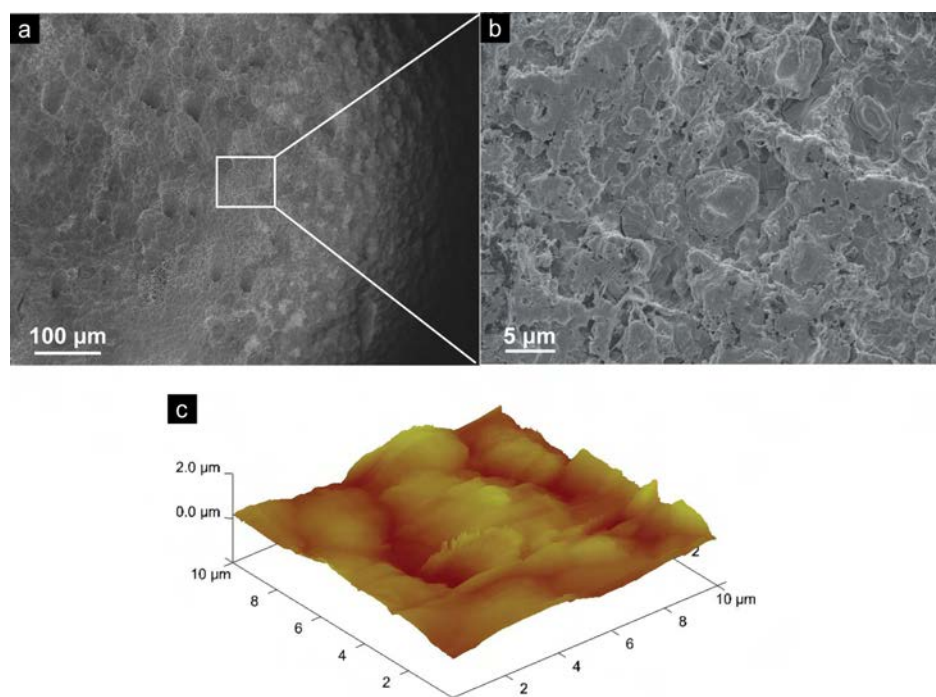


Figure 8.6 a), b) SEM and c) AFM images of the stainless steel probe roughened by acid etching.

8.3 Fabrication of Hierarchical CNTs-based Pillar Arrays

Biomimetic adhesives typically seek to replicate the toe-pads of geckos, consisting of millions of dry adhesive setae on mesoscale arrays of columnar scanners (Figure 8.7a). Hierarchical gecko-inspired structures have been fabricated via incorporation of the CNTs onto the micro-patterned hard epoxy (SU-8) substrates as shown in Figure 8.7b. SU-8 ($E = 4$ GPa) was chosen to construct the pillar arrays because of its mechanical properties that are similar to β -keratin. A careful optimization of the compression pressure during the imprinting process was crucial because of the delicate balance of incomplete CNTs transfer and the deformation of the SU-8 PAs. Quenching the assembly to ambient temperatures and lifting off the substrate yielded SU-8 pillars tipped with CNTs. The high magnification image of an individual column ($f = 10$) reveals a hairy carpet comprised of CNTs of 20 nm in width (Figure 8.7d) which are permanently grafted onto the pillar top-surface.

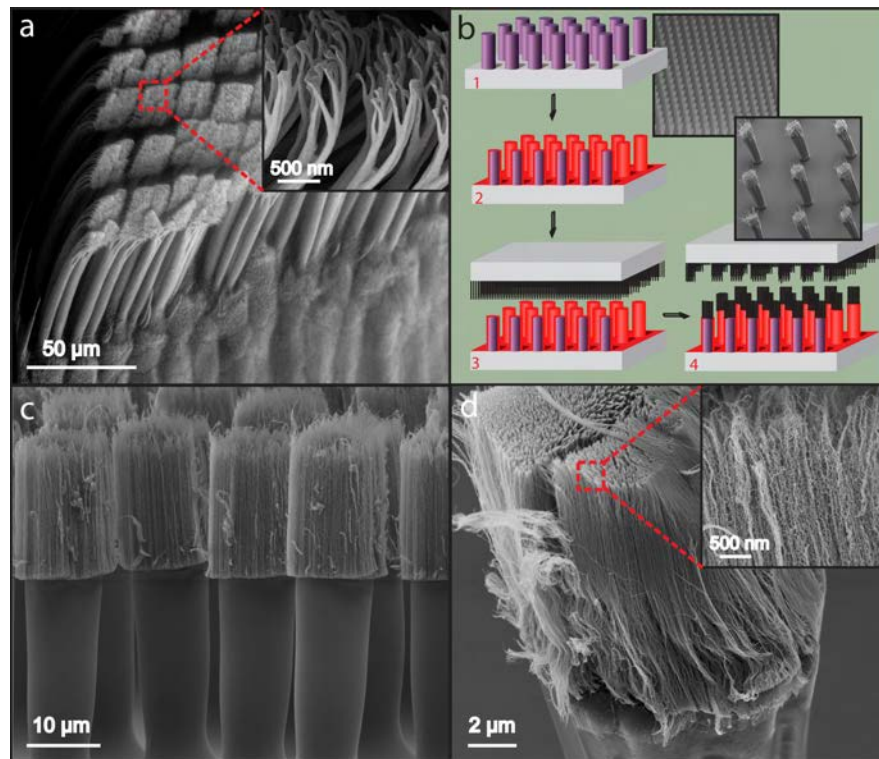


Figure 8.7 a) SEM image of a gecko toe pad showing hierarchically organized setae that terminate in thousands of nanoscale spatulas (inset).¹⁶⁸ b) Schematic illustration of the fabrication process: 1: the photolithographic fabrication of SU-8 pillar arrays, 2: the resulting pillar array is coated with an adhesive, 3: followed by imprinting a CNTF on the SU-8 pillars which after lift-off transfers the CNTs onto the SU-8 pillars. c) Side-on SEM view of polymer pillars tipped with CNTs. d) High magnification of an individual pillar reveals the close similarity to a).

HPAs with diameters (d) of 5 μm , 10 μm , and 20 μm and center-to-center spacing (a) of 45 μm , 40 μm , and 20 μm , resulting in a packing density (φ) of 15.5%, 4.9%, and 4.9%, respectively, were fabricated on large surface areas (1 cm \times 1 cm) (Figure 8.8).

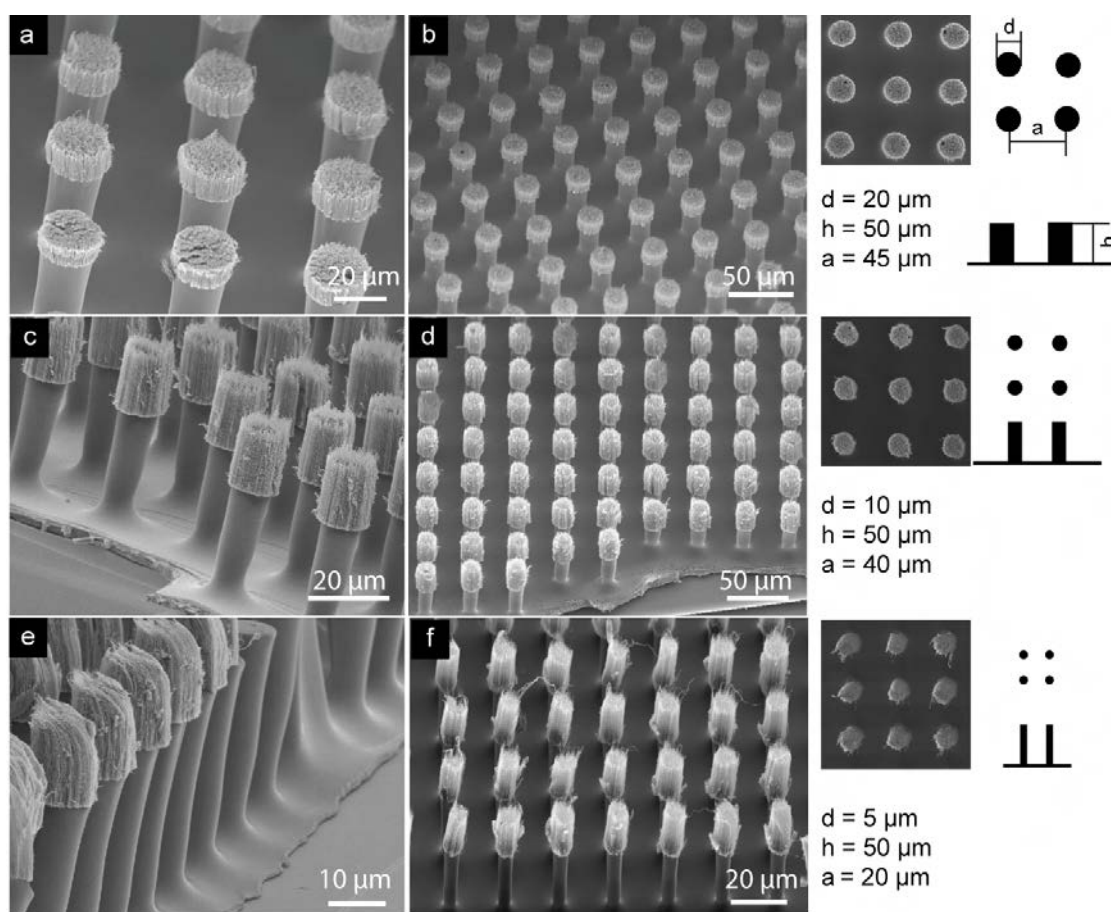


Figure 8.8 SEM images of HPAs with different feature dimensions. a), b) HPA-I ($f = 2.5$, $\varphi = 15.5\%$); c), d) HPA-II ($f = 5$, $\varphi = 4.9\%$); e), f) HPA-III ($f = 10$, $\varphi = 4.9\%$).

8.4 Adhesion Characterization

8.4.1 Force Measurements on Smooth Surfaces

To demonstrate the adhesion performance of the HPA surfaces, we used a force measurement setup with precise control of a normal pre-load that records shear forces using a multi-axis force sensor (Figure 8.9a).²⁰⁷ Although typically used for studying adhesion of insects, this setup has only rarely been employed for measuring the adhesive properties of biomimetic structures. Due to the lack of standardized test methodologies for the adhesion, a

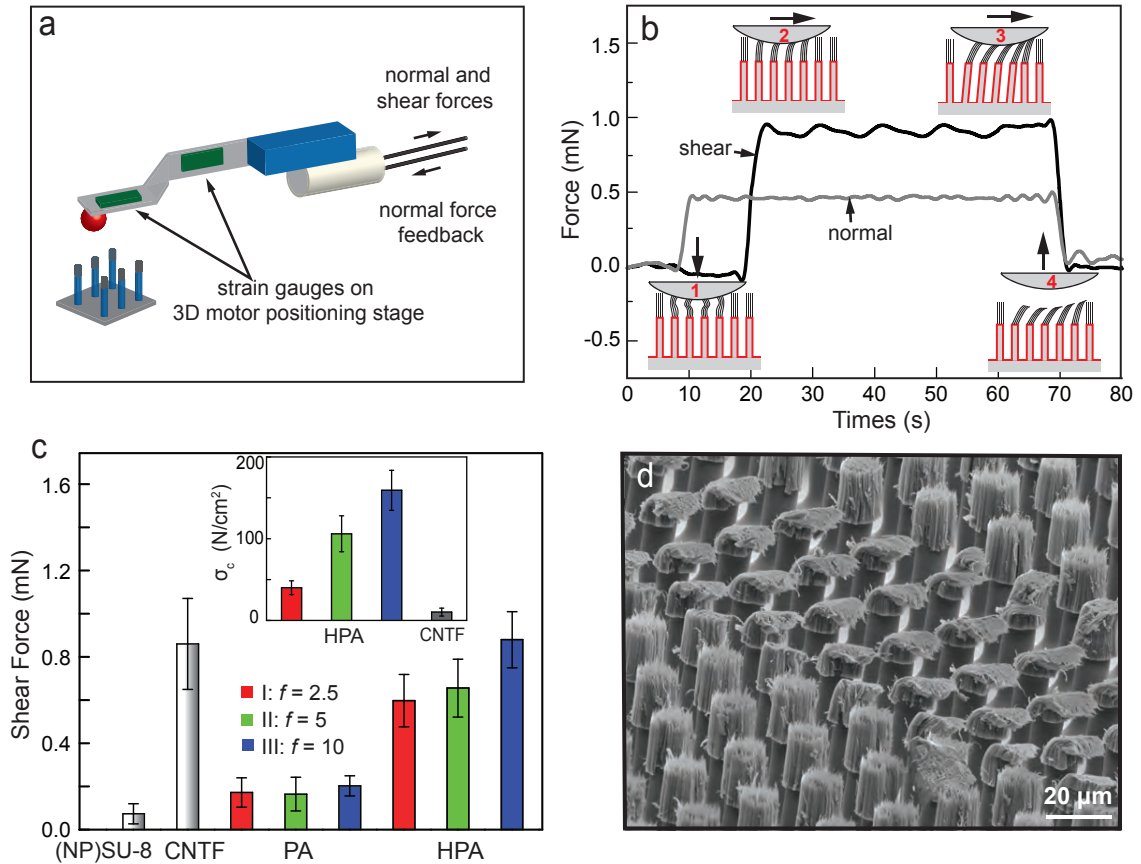


Figure 8.9 Adhesion performance of hierarchical pillar arrays (HPAs). a) Schematic illustration of the experimental setup used to measure shear and normal forces of HPAs.²⁰⁷ b) Representative curve of shear (black) and normal (grey) forces versus time for an HPA with $f = 10$ with a probe speed of $100 \mu\text{m/s}$. The insets depict the four typical steps during the force measurement process. c) Shear force of PAs and HPAs of three different aspect ratios in comparison to the reference substrates of non-patterned SU-8 and CNTF sheared against a smooth probe. The insets show the normalized shear strength σ_c of HPAs compared to CNTF. d) SEM images of the morphological change in the HPA structure caused by the shear adhesion measurements, showing the imprint of the probe surface.

range of methodologies has been used.^{183,196,205,208–210} Most of these make use of a customized apparatus with a uniaxial force sensor, which complicates the recording and analysis of the adhesion versus preload data. The setup of Figure 8.9a enables a greater degree of control during the shear force measurement, where a preload-slide-retract movement is performed using a spherical probe and a more accurate shear force is detected while the probe is sliding on the sample surface using a normal force feedback loop.

A representative force versus time curve for an HPA surface with $f = 10$ is shown in Figure 8.9b, depicting a typical measurement load-displacement cycle consisting of the initial preload (1), sliding/shearing (2 and 3), and retraction (4) steps (Figure 8.9b, insets). In Step 1, the 20 μm high CNTs on top of the PAs are able to withstand the compressive load by bending. Sliding the probe triggers an alignment of CNTs in the shear direction (Step 2) causing a marked increase in the shear force (Figure 8.9b). Two stages of HPA deformation can occur: (i) shear deformation of the CNTs (Step 2) followed by (ii) bending of the SU-8 columns once nanotube deformation has reached its maximum (Step 3). Unloading the probe resets normal and shear forces (Step 4). The preload force (0.5 mN) was optimized to give reproducible force curves and used for all sample measurement in this study. Too high preload causes the structure failure of SU-8 pillars, while too low preload brings high noise to signal ratio.

Shear adhesion of HPAs with $f = 2.5, 5$ and 10 , and lateral densities of $\varphi = 15.5\%$, 4.9% and 4.9% , respectively, were measured against a smooth surface. Figure 8.9c shows the measured shear force F for the non-patterned SU-8 film, CNTF, PAs and HPAs of three different aspect ratios. The decoration of the PAs with CNTs resulted in an increase in the shear force by more than a factor of three. The shear force supported by the HPAs of identical packing density $\varphi = 4.9\%$ is higher for HPA-III with $f = 10$ compared to the lower aspect ratio HPA-II with $f = 5$. This implies that SU-8 pillars undergo elastic deformation, thereby contributing to the increase in adhesion shear strength. Moreover, pillars of $f = 2.5$ with triple the packing density ($\varphi = 15.5\%$) compared to $f = 5$ with $\varphi = 4.9\%$ exhibit a similar shear strength within the experimental error. A high packing density is likely required to compensate the adhesion reduction of the low aspect ratio SU-8 pillars (less elastic deformation).

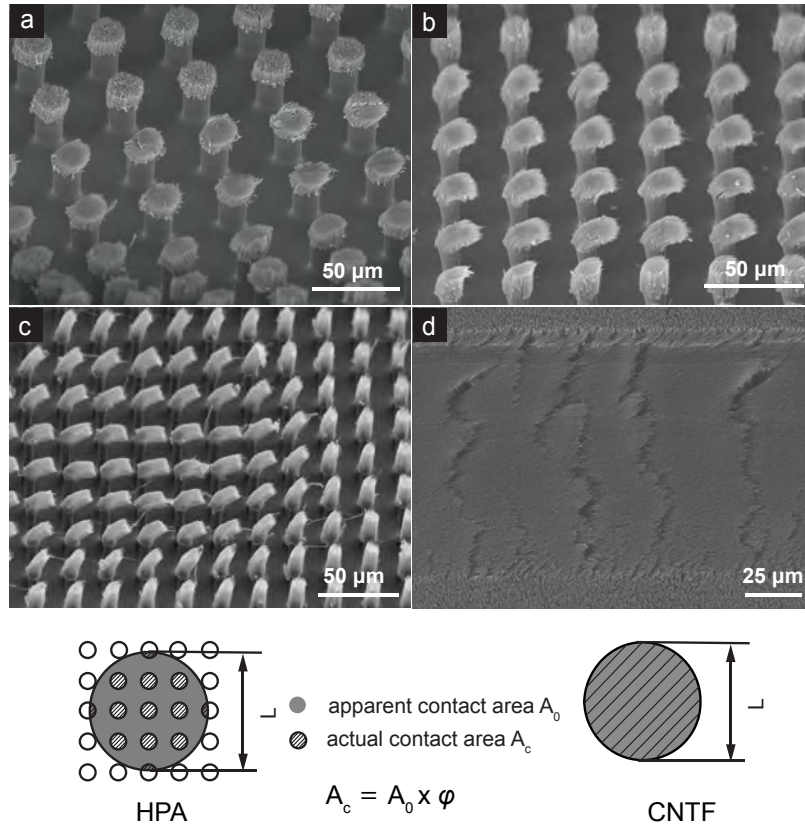


Figure 8.10 SEM images of HPAs after shear adhesion measurements with spherical probe showing the contact area during measurements a) HPA-I; b) HPA-II; and c) HPA-III. The apparent contact area is calculated by $A_0 = \pi \times (\frac{L}{2})^2$ according to the contact area where CNTs show a plastic deformation.

The maximum shear force of 0.88 ± 0.13 mN was obtained on the HPA with the highest aspect ratio $f = 10$. The apparent contact area A_0 between the probe and the HPA-covered surface was obtained from the SEM micrographs after shear adhesion measurements (Figure 8.10), assuming a spherical indentation with plastic deformation of CNTs in contact during shear. The apparent contact area is given by $A_0 = \pi \times (\frac{L}{2})^2$. For calculation of contact area A_0 , the following parameters were used: $L = 110$ μm for HPA-I, $L = 120$ μm for HPA-II, $L = 120$ μm for HPA-III and $L = 100$ μm for CNTF. The actual contact area is given by: $A_c = A_0 \times \varphi$, and the normalized shear strength is given by: $\sigma_c = F/A_c$.

This yields a shear strength of 7.8 ± 1.2 N/cm² for the $f = 10$ HPA. While the maximum shear force of the $f = 10$ HPA is comparable to that of CNTFs, it has a nanotube area coverage of less than 5%. σ_c plotted in the inset of Figure 8.9c therefore emphasizes the benefit of the hierarchically structured surface. It is worth noting that since we inverted the carbon

nanotubes after the imprinting transfer, the adhesion of CNTF top and bottom was both measured, showing statistically similar adhesion (not shown).

Similar shear forces were observed when measuring HPAs with hydrophobic (Figure 8.11) and hydrophilic surfaces. This supports the assumption that the van der Waals forces dominate the adhesion between the carbon nanotubes and the shear-probe surface.¹⁷⁵ Note that the normal force on detachment was found to be too small to be determined from the force curve, i.e. when measuring in a 'load-retract' cycle, as it was screened by the setup noise. The small normal force is explained by the small coverage of CNTs on HPAs and the relatively low packing density of CNTs used in this study, while reported normal forces varied from 5 to 29 N/cm² arising from an uncontrolled high preload.^{201,203,206}

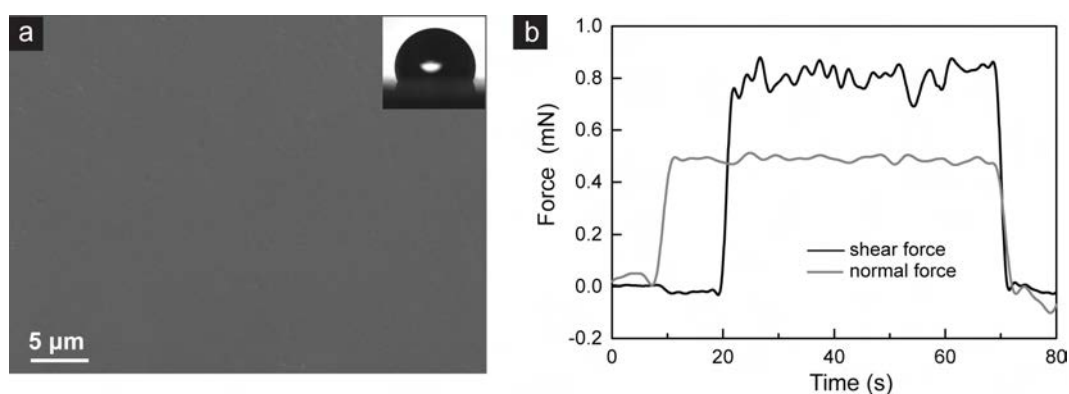


Figure 8.11 a) SEM image of the probe surface morphology. (b) Shear adhesion measurement of the HPA-III using HMDS-treated glass probe.

The morphological difference between the sheared and non-sheared HPA-covered areas, as shown in Figure 8.9d and Figure 8.10, shows that while the polymer pillars restore to their original pre-measurement configuration, CNTs are plastically deformed along the shear direction. This indicates that the shear induced nanotube side contact enhance adhesion, in similarity to the gecko toe pads. The plastically deformed CNTs, with structure asymmetry, closely resemble spatulae hairs. This post-measurement configuration reveals an increased effective contact area from the CNT sidewalls, which appears to be advantageous for further attachment-detachment cycles as discussed below.

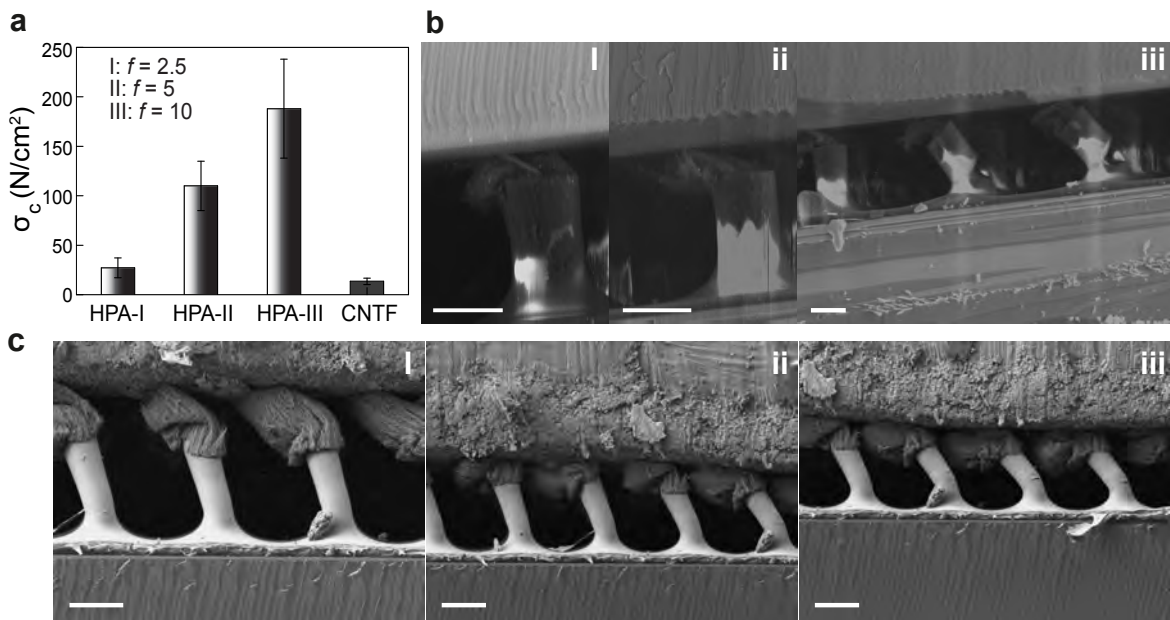


Figure 8.12 a) Normalized shear stress σ_c of HPAs of three different aspect ratios compared to CNTF measured against a rough surface with an average surface roughness of $R_a = 200$ nm. Shear forces were measured under a normal force of 0.5 mN and a probe speed of 100 $\mu\text{m/s}$. *In-situ* SEM images of HPAs under a constant normal load at different shear stages against a smooth (b) and a rough (c) surface. Scale bars stand for 20 μm in b) and 10 μm in c), respectively.

8.4.2 Force Measurements on Rough Surfaces

Distributed adhesion surfaces also excel in contact with rough surfaces. To test this, shear forces of HPAs in contact with sub-micron rough surfaces were measured. While most natural surfaces contain multi-scale topological profiles, not much attention has been paid to the effect of roughness on the adhesion properties of biological and biomimetic adhesives. Recent studies have demonstrated that roughness can significantly affect the performance of gecko^{211,212} and synthetic bio-mimetic adhesives.^{213,214}

Rough surfaces were prepared by chemical etching of sphere probes, yielding an average surface roughness of $R_a = 200$ nm (Figure 8.6), which was used as the rough probe in force measurements. HPA surfaces with $f = 10$ show a shear strength of $\sigma_c = 185 \pm 50$ N/cm² (Figure 8.12a) normalized to the actual contact area, which is higher by nearly one order of magnitude compared to CNTFs. The hierarchy of HPAs thus compensates for the decrease of the CNT coverage.

In order to resolve the structural deformation under shearing, *in-situ* SEM was performed by integrating a tension stage into the SEM. The morphological adaptation of HPAs during

shear was investigated using both smooth (Figure 8.12b) and rough (Figure 8.12c) surfaces. When shearing against a smooth substrate, HPAs initially form contacts with their tips to the target surface and then tilt in the shear direction to adhere predominantly via their side walls (Figure 8.12b i-ii). Further shear fractures the SU-8 pillars close to their base (Figure 8.12b iii). This confirms the strong connection of CNTs to the SU-8 pillars. This result also implies that low aspect ratio SU-8 pillars do not play a substantial role in improving adhesion.

When shearing a HPA against rough surfaces, sequential SEM images reveal similar initial adhesion morphologies of the HPAs with initial tip contacts and CNTs bending in the shear direction. Strong shear however resulted in additional elastic bending of the SU-8 micro-pillars (Figure 8.12c iii) and no fracture of the SU-8 pillars was observed at comparable stage to Figure 8.12b iii. This indicates that the hierarchical structure of HPAs is beneficial for adhesion to the rough surfaces. This is also corroborated with higher shear stress for high aspect ratio structures ($f = 10$) in contact with a rough surface (Figure 8.12a) as compared to a smooth surface (Figure 8.9c). Note that while the SU-8 was chosen for its high stiffness, it is more brittle than β -keratin. The simultaneous optimization of pillar material in terms of its stiffness and fracture toughness and packing densities is therefore likely to further improve the shear-adhesion performance of HPAs.

8.4.3 Oscillatory Shear Measurements

The structural integrity and adhesion durability of HPA surfaces were investigated by oscillatory shear adhesion measurement over 25 cycles, as shown in Figure 8.13a. Following the bending deformation of the CNTs after the first shear movement, a shear movement in the reciprocal direction was performed (Figure 8.13a, left inset). This measurement is performed to reveal the structural integrity, with each hierarchical pillar subjected to attachment and detachment as the probe slides along. Interestingly, a symmetric shear force curve is observed for each cycle (Figure 8.13a, right inset). The deformed hierarchical structures producing a comparable shear force to those in the initial upright state. The plastic deformation of the CNTs on top of SU-8 pillars results in a shear force that was decreased by a factor of two after the initial shear cycle and then remained constant for the following 23 cycles, in contrast to a decrease in shear strength by a factor of four of the CNTF after two

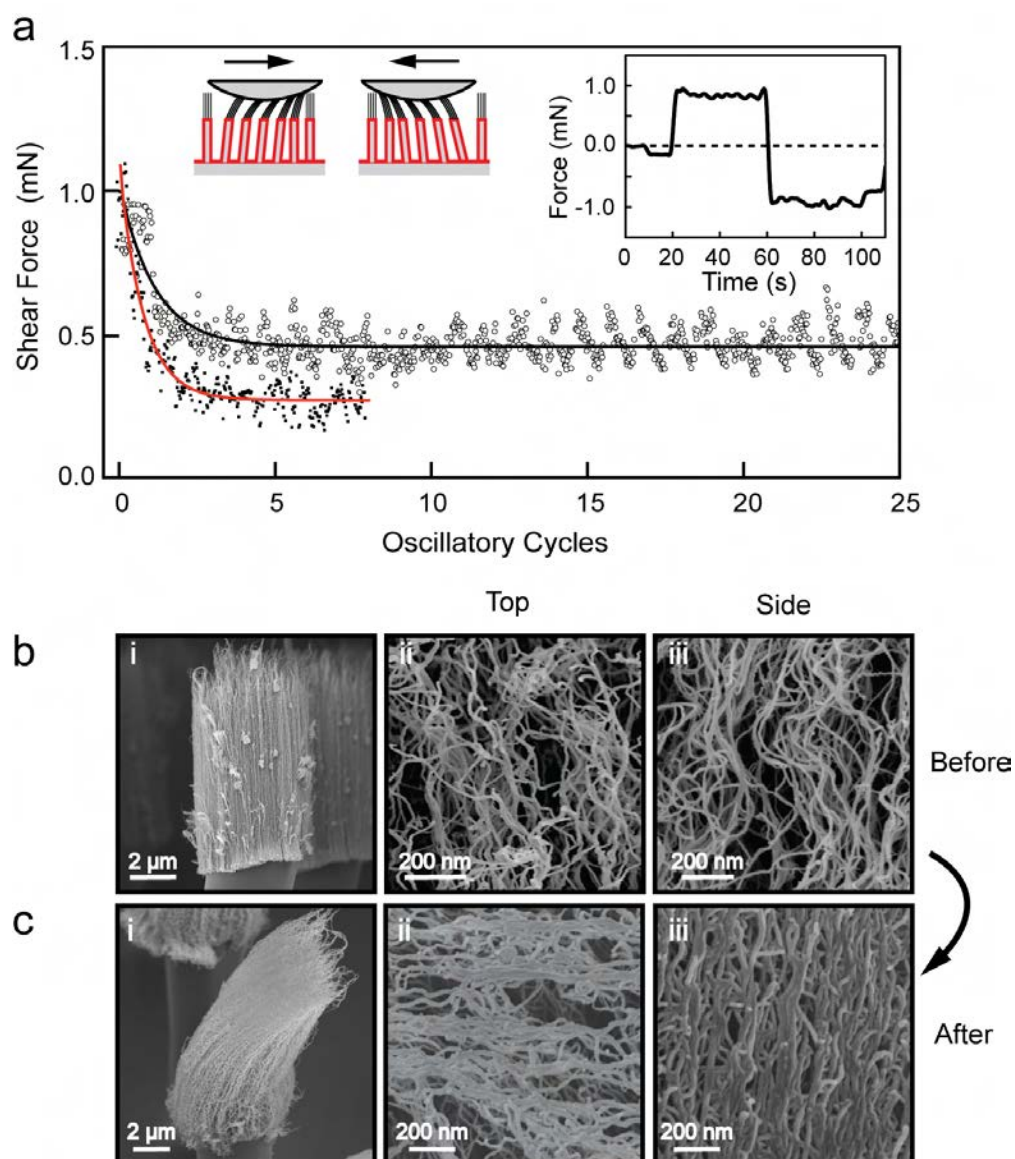


Figure 8.13 a) Shear force measurements of a HPA with $f=10$ (open circles) over 25 oscillatory cycles compared with a CNTF (filled circles) over 8 cycles (trend line is a guide to the eye). The inset on the left-hand side depicts the structural change in HPAs during the oscillatory measurements. A symmetric shear force curve observed for each cycle is shown in the right-hand side inset. SEM images of the morphological changes (i-iii) of the CNTs grafted on top of polymer pillars b) prior to and following c) the shear adhesion measurements.

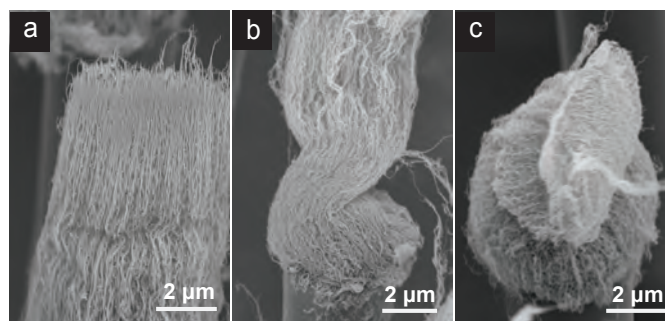


Figure 8.14 CNTs show plastic deformation after oscillation shear experiments. SEM images of CNTs on HPAs after oscillatory measurements showing different deformation a) bended, b) twisted, c) buckled morphology.

cycles (Figure 8.13a). As the shear adhesion in CNTFs arises mainly from the tip contact, in contrast to both top and side contact contributions in HPAs, the repeated stretching of tip entanglements lead to a faster degradation of adhesion in CNTFs.

To further understand the origin of contacts on attachment, we examined the morphologies of CNTs before and after the initial shear cycle. The CNTs on polymer pillars consisted of loosely packed bundles (Figure 8.13b iii) with randomly entangled tips (Figure 8.13b ii). The applied shear force causes the vertical nanotube bundles to tilt in the shear direction (Figure 8.13c i). This stretches the entangled CNT-web in the lateral (Figure 8.13c ii) and vertical (Figure 8.13c iii) direction, allowing CNT side-wall adhesion and thus improving their shear adhesion. Buckling of CNTs was observed after 25 shear-cycles caused by the bending and torsional load, with full CNT collapse in some contact areas (Figure 8.14). These post-measurement morphologies of HPA surfaces reveal that repeated shearing causes the irreversible plastic deformation of nanotubes giving rise to a deteriorated shear adhesion.

8.5 Conclusion

In summary, we have established a novel approach for fabrication of hierarchical structures with micrometer polymer pillars (setae) and nanometre CNTs (spatulas), enabling close bio-mimicking of the gecko-adhesive behavior and properties. We have also systematically tested the effect of the hierarchical arrangement of CNTs in the final adhesion performance, employing a highly suitable experimental set-up for such a system. The adhesion shear strength of HPA surfaces contacted with rough surfaces was nine times larger compared

8.5 Conclusion

to CNTFs. This is a direct outcome of the structural hierarchy of HPAs, which enables an enhanced conformal attachment of the adhesive elements to the rough surface topography. While the absolute shear strength of the HPA structures described here is comparable to the gecko toe-pad, our study is mainly a proof-of-principle that clearly shows that the concept of hierarchically-engineered structures based on polymer and CNTs is a viable approach for the design of synthetic biomimetic adhesives.

Chapter 9 Summary

This thesis mainly studies the structure formation in several polymer blend systems and the correlation between the morphology and their optoelectronic performance. In addition, a side project on the fabrication of hierarchical structures mimicking geckos' toe-pads is also presented. This chapter summarizes the main findings of the studies and discusses their possible future research directions.

P3HT/PCBM blends

Chapter 4 discusses the structure evolution of P3HT/PCBM blends and how the crystallization of P3HT leads to a beneficial BHJ nanostructure is presented. Using optical microscopy, we observed the PCBM aggregation behavior when mixed with regiorandom (amorphous) or regioregular (semicrystalline) P3HT at various ratios. The comparison of the onset points when PCBM starts to aggregate indicates its strong dependency on the crystallinity of P3HT. X-ray scattering experiments using a well-defined monodisperse P3HT investigate the effect of the addition of PCBM on the crystalline structure of P3HT. The long period signal in SAXS and GISAX spectra gives the total thickness of the crystalline lamellae and the amorphous interlayer. The dissolution of PCBM into the amorphous interlayer is evident by a 2-3 nm increase in the long period, while the P3HT crystallinity remains unaltered. Importantly, PCBM dissolution in the amorphous interlamellar regions leads to a vanishing scattering contrast. Surpassing the solubility limit, PCBM segregates out of the amorphous region and crystallizes. The P3HT/PCBM system exhibits several features that can be summarized as follows: (1) the miscibility of the two components; (2) P3HT showing strong tendency to crystallize; (3) the secondary aggregation and crystallization of PCBM; (4) the edge-on ori-

entation of P3HT crystals together with the preferred orientation of lamellae for photovoltaic devices.

Chapter 5 demonstrates the spherulitic crystallization of P3HT that directs the structure formation in the P3HT/PCBM blend. Using solvent vapour annealing (SVA) with CS₂ as solvent, the nucleation density of P3HT is significantly reduced so that large spherulites can be obtained from pure P3HT films and P3HT/PCBM blend films. The fact that the recrystallization of P3HT occurs for a larger undercooling during SVA indicates a good miscibility between P3HT and PCBM. The spherulitic crystallization of P3HT in the blend film brings about a red-shifted spectrum in UV-Vis due to the increased conjugation length of P3HT. The morphology of P3HT/PCBM films is shown to preserve the lamellar stacking of spherulites, in contrast to the lack of long range order in the TA film. The photovoltaic devices made from spherulitic P3HT/PCBM exhibited good PCEs of 3.0% and 2.4% in the standard and inverted device geometries, respectively. The device results support that structure formation in P3HT/PCBM blends is driven by the crystallization of P3HT into lamellae which produce a morphology beneficial for BHJ photovoltaic operation.

P3HT/F8TBT blends

In Chapter 6, the structure formation in a polymer/polymer blend consisting of P3HT and F8TBT is discussed. The miscibility between P3HT and F8TBT is investigated using the same approach for the P3HT/PCBM system. Thin films of amorphous P3HT mixed with F8TBT show macroscopic lateral phase separation at weight ratios from $f = 0.15$ to $f = 2$, while semicrystalline P3HT with F8TBT films appear to be homogeneous due to the predominant P3HT crystallization over their phase separation process. X-ray scattering experiments reveal the mixing of F8TBT in the amorphous P3HT interlamellar regions by detecting the change of the long period. The long period of P3HT increases from 14 nm to 16 nm for a F8TBT weight ratio of $f = 1$. Since the crystallinity of P3HT is not affected by the addition of F8TBT, the increase in long period indicates the swelling of amorphous P3HT interlayers by F8TBT. In addition, a vertical phase separation with P3HT wetting at the top surface and F8TBT segregated at the bottom interface is observed. The structure formation in P3HT/F8TBT is therefore similar to P3HT/PCBM in that the crystallization of P3HT gives

rise to a bulk heterojunction interface on 10 nm length scale in spite of a much lower miscibility between the two components.

Furthermore, the spherulitic crystallization of P3HT is achieved in P3HT/F8TBT blends, which also indicates that the crystallization of P3HT is the dominant driving force rather than demixing. Using the same SVA method, the supercooling of solvent vapour during the dissolution-recrystallization process can be adjusted, and therefore the size of P3HT spherulites is varied by one order of magnitude. Photovoltaic devices were fabricated based on spherulitic films and compared to the standard optimized devices. The spherulitic devices show improved fill factors but lower PCEs were obtained due to a decrease in photocurrent. The results support that P3HT crystallization determines the nanostructure that is required for exciton dissociation, while the segregation of F8TBT at the interface is detrimental for device operation.

In summary, the findings in P3HT/PCBM and P3HT/F8TBT systems provide implications for the generation of active layers in organic photovoltaics (OPVs). The origin of the morphology in P3HT/PCBM and P3HT/F8TBT systems is described as a crystallization-induced phase separation followed by the aggregation/crystallization of the second component. We have systematically investigated the crystallization of P3HT in blends, but the present experimental techniques could not provide information on the spatial distribution of PCBM or F8TBT. Future experiments using angle resolved X-ray photoelectron spectroscopy together with X-ray reflectivity could provide more information on the in-depth composition profiling. Moreover, characterization of polymer blends using scanning transmission X-ray microscopy can resolve the nanomorphology, providing quantitative chemical mapping.

The morphology studies in the thesis are based on samples that are carefully equilibrated by either melt annealing or solve vapour annealing. The morphology could be different from that of the films used as active layers in OPVs, which are prepared by spin coating followed by mild annealing. Thus, it is important to investigate the morphology evolution in non-equilibrated films, which can directly relate to the OPV device fabrication.

It should also be noted that the structural studies are based on semicrystalline P3HT, while there are many successful polymer/fullerene systems using polymers that are amorph-

ous or much less crystalline than P3HT, such as PCDTBT and PTB7. The findings from our study may not apply to these systems. Several studies have shown that the aggregation/crystallization of fullerene play a critical role in amorphous blend systems. This indicates the miscibility between materials is an important parameter for the determination of donor and acceptor composition. Fundamental thermodynamic miscibility study could help the optimization of device performance for newly developed photovoltaic polymer blends.

P3HT/PEO blends

Chapter 7 investigates the phase separation in a crystalline/crystalline polymer blend of P3HT/PEO and its effect on the organic FET performance. The spin coated films of P3HT/PEO from a good solvent shows typical lateral phase separation of polymer blends, which indicates the strong immiscibility between the two components. In contrast, introducing crystallization of P3HT in solutions gives rise to a vertically separated structure where networks of P3HT nanowires are present at the substrate and the top interface. The application of P3HT/PEO blends in thin film FETs has been demonstrated. The presence of P3HT nanowire networks at the substrate interface provides an efficient charge transport pathway inside the insulating PEO matrix, which ensures the good charge carrier mobility at P3HT content as low as 10 wt%. This procedure offers a way to produce vertical stratified structures of polymer semiconductors that may be also interest for a variety of electronic applications.

Biomimetic hierarchical structures to mimic gecko adhesion

Chapter 8 presents the fabrication of hierarchical structures to mimic the gecko's adhesive toe-pads. The hierarchical pillar arrays consist of micrometer-sized SU-8 pillars covered by vertically aligned CNTs that mimicking the spatulae. This hierarchical structure was prepared by a imprinting transfer of CNTFs to photolithographic patterned SU-8 pillar arrays, which provides a way to combine CNTs with other structured materials. We tested the adhesion performance of the hierarchical structures of CNTs on arrays of SU8 pillars of different aspect ratios and area coverage. Comparable shear forces were achieved on HPAs with an aspect ratio of 10 to that of CNTFs although the area coverage was less than 5%.

The shear stress of HPAs normalized to actual contact area was found to be significantly higher than that of CNTFs, which shows the benefit from their structural hierarchy enabling a conformal attachment of the CNTs to the surface topography. Thus, the gecko-inspired hierarchical CNTs/polymer-based structures offer good reusable, low-cost and large-area synthetic bio-adhesive substitutes. Further optimization of structural parameters and the polymer material used is likely to improve the strong and repeatable adhesion of HPAs.

List of Abbreviations

Abbreviation	Full term
ACN	acetonitrile
AFM	atomic force microscopy
BHJ	bulk heterojunction
CB	chlorobenzene
CS ₂	carbon disulfide
CNT	carbon nanotube
CNTF	carbon nanotube forest
EQE	external quantum efficiency
FF	fill factor
FET	field-effect transistor
F8TBT	poly[(9,9-dioctylfluorene)-2,7-diyl-alt-(4,7-bis(3-hexylthien-5-yl)-2,1,3-benzothiadiazole)-2', 2''-diyl]
GIXS	grazing-incident X-ray scattering
GISAXS	grazing-incident small angle X-ray scattering
GIWAXS	grazing-incident wide angle X-ray scattering
HPA	hierarchical pillar array
HOMO	highest occupied molecular orbital
LUMO	lowest unoccupied molecular orbital
OPV	organic photovoltaic
P3HT	poly(3-hexylthiophene)
PCBM	phenyl-C61-butyric-acid methyl ester
PS	polystyrene
PEO	polyethylene oxide
PCE	power conversion efficiency
PL	photoluminescence
POM	polarized optical microscopy
PA	pillar array
SVA	solvent vapor annealing
SAXS	small angle X-ray scattering
TA	thermal annealing
XR	X-ray reflectivity
XRD	X-ray diffraction
SEM	scanning electron microscopy
TEM	transmission electron microscopy
UV-Vis	ultraviolet-visible

Bibliography

- [1] Gunes, S.; Neugebauer, H.; Sariciftci, N. Conjugated polymer-based organic solar cells. *Chem. Rev.* **2007**, *107*, 1324–1338.
- [2] Li, G.; Zhu, R.; Yang, Y. Polymer solar cells. *Nature Photon.* **2012**, *6*, 153–161.
- [3] http://www.nrel.gov/ncpv/images/efficiency_chart.jpg.
- [4] Sze, S. M.; Ng, K. K. *Physics of semiconductor devices*; John Wiley & Sons, 2007.
- [5] Gregg, B. Excitonic solar cells. *J. Phys. Chem. B* **2003**, *107*, 4688–4698.
- [6] Tang, C. Two-layer organic photovoltaic cell. *Appl. Phys. Lett.* **1986**, *48*, 183.
- [7] Spanggaard, H.; Krebs, F. A brief history of the development of organic and polymeric photovoltaics. *Sol. Energ. Mat. Sol. Cells* **2004**, *83*, 125–146.
- [8] Burroughes, J.; Bradley, D.; Brown, A.; Marks, R.; Mackay, K.; Friend, R.; Burns, P.; Holmes, A. Light-emitting diodes based on conjugated polymers. *Nature* **1990**, *347*, 539–541.
- [9] Coakley, K.; McGehee, M. Conjugated polymer photovoltaic cells. *Chem. Mater.* **2004**, *16*, 4533–4542.
- [10] Cheng, Y.; Yang, S.; Hsu, C. Synthesis of conjugated polymers for organic solar cell applications. *Chem. Rev.* **2009**, *109*, 5868–5923.
- [11] Bundgaard, E.; Krebs, F. Low band gap polymers for organic photovoltaics. *Solar Energy Materials and Solar Cells* **2007**, *91*, 954–985.
- [12] Winder, C.; Sariciftci, N. Low bandgap polymers for photon harvesting in bulk heterojunction solar cells. *J. Mater. Chem.* **2004**, *14*, 1077–1086.
- [13] Bruice, P. Y. *Organic Chemistry*; Pearson Education, Prentice Hall, 2004.
- [14] Moliton, A.; Hiorns, R. Review of electronic and optical properties of semiconducting π -conjugated polymers: applications in optoelectronics. *Polym. Int.* **2004**, *53*, 1397–1412.

Bibliography

- [15] Strobl, G. *The Physics of Polymers*; Springer, 2006.
- [16] Barford, W. *Electronic and optical properties of conjugated polymers*; Oxford Clarendon Press, 2005.
- [17] Turro, N. J.; Ramamurthy, V.; Scaiano, J. C. *Principles of Molecular Photochemistry: An Introduction*; University Science Books, 2009.
- [18] Pope, M.; Swenberg, C. E. *Electronic processes in organical crystals and polymers*; Oxford University Press, 1999.
- [19] Coropceanu, V.; Cornil, J.; da Silva Filho, D.; Olivier, Y.; Silbey, R.; Brédas, J.-L. Charge transport in organic semiconductors. *Chem. Rev.* **2007**, *107*, 926–952.
- [20] Kallmann, H.; Pope, M. Photovoltaic effect in organic crystals. *J. Chem. Phys.* **1959**, *30*, 585–586.
- [21] Yu, G.; Gao, J.; Hummelen, J.; Wudl, F.; Heeger, A. Polymer photovoltaic cells: enhanced efficiencies via a network of internal donor-acceptor heterojunctions. *Science* **1995**, 1789–1790.
- [22] Halls, J.; Walsh, C.; Greenham, N.; Marseglia, E.; Friend, R.; Moratti, S.; Holmes, A. Efficient photodiodes from interpenetrating polymer networks. *Nature* **1995**, *376*, 498–500.
- [23] Clarke, T.; Durrant, J. Charge photogeneration in organic solar cells. *Chem. Rev.* **2010**, *110*, 6736–6767.
- [24] Qi, B.; Wang, J. Open-circuit voltage in organic solar cells. *J. Mater. Chem.* **2012**, *22*, 24315–24325.
- [25] Pearson, A.; Wang, T.; Lidzey, D. The role of dynamic measurements in correlating structure with optoelectronic properties in polymer: fullerene bulk-heterojunction solar cells. *Rep. Prog. Phys.* **2013**, *76*, 022501.
- [26] Troshin, P. A.; Hoppe, H.; Renz, J.; Egginger, M.; Mayorova, J. Y.; Goryachev, A. E.; Peregudov, A. S.; Lyubovskaya, R. N.; Gobsch, G.; Sariciftci, N. S.; Razumov, V. F. Material solubility-photovoltaic performance relationship in the design of novel fullerene derivatives for bulk heterojunction solar cells. *Adv. Funct. Mater.* **2009**, *19*, 779–788.
- [27] Liang, Y.; Yu, L. A new class of semiconducting polymers for bulk heterojunction solar cells with exceptionally high performance. *Accounts of chemical research* **2010**, *43*, 1227–1236.
- [28] Ma, W.; Yang, C.; Gong, X.; Lee, K.; Heeger, A. J. Thermally stable, efficient polymer solar cells with nanoscale control of the interpenetrating network morphology. *Adv. Funct. Mater.* **2005**, *15*, 1617–1622.
- [29] Li, G.; Shrotriya, V.; Huang, J.; Yao, Y.; Moriarty, T.; Emery, K.; Yang, Y. High-efficiency solution processable polymer photovoltaic cells by self-organization of polymer blends. *Nature Mater.* **2005**, *4*, 864–868.
- [30] Park, S.; Roy, A.; Beaupré, S.; Cho, S.; Coates, N.; Moon, J. S.; Moses, D.; Leclerc, M.; Lee, K.; Heeger, A. J. Bulk heterojunction solar cells with internal quantum efficiency approaching 100%. *Nature Photon.* **2009**, *3*, 297–303.

Bibliography

- [31] Chu, T.; Alem, S.; Tsang, S.; Tse, S.; Wakim, S.; Lu, J.; Dennler, G.; Waller, D.; Gaudiana, R.; Tao, Y. Morphology control in polycarbazole based bulk heterojunction solar cells and its impact on device performance. *Appl. Phys. Lett.* **2011**, *98*, 253301.
- [32] He, Z.; Zhong, C.; Su, S.; Xu, M.; Wu, H.; Cao, Y. Enhanced power-conversion efficiency in polymer solar cells using an inverted device structure. *Nature Photon.* **2012**, *6*, 593–597.
- [33] Thompson, B. C.; Frechet, J. M. J. Polymer-fullerene composite solar cells. *Angewandte Chemie International Edition* **2008**, *47*, 58–77.
- [34] Dennler, G.; Scharber, M. C.; Brabec, C. J. Polymer-fullerene bulk-heterojunction solar cells. *Adv. Mater.* **2009**, *21*, 1323–1338.
- [35] Liu, F.; Gu, Y.; Jung, J. W.; Jo, W. H.; Russell, T. P. On the morphology of polymer-based photovoltaics. *J. Polym. Sci. Part B Polym. Phys* **2012**, *50*, 1018–1044.
- [36] Hoppe, H.; Niggemann, M.; Winder, C.; Kraut, J.; Hiesgen, R.; Hinsch, A.; Meissner, D.; Sariciftci, N. Nanoscale morphology of conjugated polymer/fullerene based bulk-heterojunction solar cells. *Adv. Funct. Mater.* **2004**, *14*, 1005–1011.
- [37] Shaheen, S.; Brabec, C.; Sariciftci, N.; Padinger, F.; Fromherz, T.; Hummelen, J. 2.5% efficient organic plastic solar cells. *Appl. Phys. Lett.* **2001**, *78*, 841.
- [38] Bavel, S.; Sourty, E.; With, G.; Loos, J. Three-dimensional nanoscale organization of bulk heterojunction polymer solar cells. *Nano Lett.* **2009**, *9*, 507–513.
- [39] Chen, D.; Liu, F.; Wang, C.; Nakahara, A.; Russell, T. P. Bulk heterojunction photovoltaic active layers via bilayer interdiffusion. *Nano Lett.* **2011**, *11*, 2071–2078.
- [40] Staniec, P.; Parnell, A.; Dunbar, A.; Yi, H.; Pearson, A.; Wang, T.; Hopkinson, P.; Kinane, C.; Dalgliesh, R.; Donald, A. The nanoscale morphology of a PCDTBT: PCBM photovoltaic blend. *Adv. Energy Mater.* **2011**, *1*, 499–504.
- [41] Lu, X.; Hlaing, H.; Germack, D. S.; Peet, J.; Jo, W. H.; Andrienko, D.; Kremer, K.; Ocko, B. M. Bilayer order in a polycarbazole-conjugated polymer. *Nat. Commun.* **2012**,
- [42] Collins, B. A.; Li, Z.; Tumbleston, J. R.; Gann, E.; McNeill, C. R.; Ade, H. Absolute measurement of domain composition and nanoscale size distribution explains performance in PTB7:PC 71BM solar cells. *Adv. Energy Mater.* **2012**, *3*, 65–74.
- [43] Hammond, M.; Kline, R.; Herzing, A.; Richter, L.; Germack, D.; Ro, H. W.; Soles, C.; Fischer, D.; Xu, T.; Yu, L. Molecular order in high-efficiency polymer/fullerene bulk heterojunction solar cells. *ACS Nano* **2011**, *5*, 8248–8257.

Bibliography

- [44] Moon, J.; Jo, J.; Heeger, A. Nanomorphology of PCDTBT: PC70BM bulk heterojunction solar cells. *Adv. Energy Mater.* **2012**, *2*, 304–308.
- [45] Jamieson, F. C.; Domingo, E. B.; Mccarthy-Ward, T.; Heeney, M.; Stingelin, N.; Durrant, J. R. Fullerene crystallisation as a key driver of charge separation in polymer/fullerene bulk heterojunction solar cells. *Chem. Sci.* **2012**, *3*, 485–492.
- [46] Chiesa, M.; Bürgi, L.; Kim, J.-S.; Shikler, R.; Friend, R.; Sirringhaus, H. Correlation between surface photovoltage and blend morphology in polyfluorene-based photodiodes. *Nano Lett.* **2005**, *5*, 559–563.
- [47] Snaith, H.; Arias, A.; Morteani, A.; Silva, C.; Friend, R. Charge generation kinetics and transport mechanisms in blended polyfluorene photovoltaic devices. *Nano Lett.* **2002**, *2*, 1353–1357.
- [48] Cowie, J. M. G. *Polymers: Chemistry & Physics of Modern Materials*; Blackie Academic & Professional, 1997.
- [49] Rubenstein, M.; Colby, R. *Polymer physics*; Oxford University Press, 2006.
- [50] Jones, R. A. L.; Richards, R. W. *Polymers at Surfaces and Interfaces*; Cambridge University Press, 1999.
- [51] Jones, R.; Kramer, E. Kinetics of formation of a surface enriched layer in an isotopic polymer blend. *Philos. Mag. B* **1990**, *62*, 129–137.
- [52] Jones, R.; Norton, L.; Kramer, E.; Bates, F.; Wiltzius, P. Surface-directed spinodal decomposition. *Phys. Rev. Lett.* **1991**, *66*, 1326–1329.
- [53] Geoghegan, M.; Krausch, G. Wetting at polymer surfaces and interfaces. *Prog. Polym. Sci.* **2003**, *28*, 261–302.
- [54] Bruder, F.; Brenn, R. Spinodal decomposition in thin films of a polymer blend. *Phys. Rev. Lett.* **1992**, *69*, 624–627.
- [55] Geoghegan, M.; Jones, R.; Clough, A. Surface directed spinodal decomposition in a partially miscible polymer blend. *J. Chem. Phys.* **1995**, *103*, 2719.
- [56] Kim, E.; Krausch, G.; Kramer, E.; Osby, J. Surface-directed spinodal decomposition in the blend of polystyrene and tetramethyl-bisphenol-A polycarbonate. *Macromolecules* **1994**, *27*, 5927–5929.
- [57] Hu, W. *Polymer Physics: A Molecular Approach*; Springer, 2012.
- [58] <http://www.doitpoms.ac.uk/tlplib/polymers/spherulites.php>.
- [59] Wu, Z.; Petzold, A.; Henze, T.; Thurn-Albrecht, T.; Lohwasser, R.; Sommer, M.; Thelakkat, M. Temperature and molecular weight dependent hierarchical equilibrium structures in semiconducting poly(3-hexylthiophene). *Macromolecules* **2010**, *43*, 4646–4653.
- [60] Thurn-Albrecht, T.; Thomann, R.; Heinzl, T.; Hugger, S. Semicrystalline morphology in thin films of poly(3-hexylthiophene). *Colloid & Polymer Science* **2004**, *282*, 932–938.

Bibliography

- [61] Brinkmann, M.; Rannou, P. Effect of molecular weight on the structure and morphology of oriented thin films of regioregular poly(3-hexylthiophene) grown by directional epitaxial solidification. *Adv. Funct. Mater.* **2007**, *17*, 101–108.
- [62] Brinkmann, M.; Rannou, P. Molecular weight dependence of chain packing and semicrystalline structure in oriented films of regioregular poly(3-hexylthiophene) revealed by high-resolution transmission electron microscopy. *Macromolecules* **2009**, *42*, 1125–1130.
- [63] Yang, H.; Shin, T. J.; Yang, L.; Cho, K.; Ryu, C. Y.; Bao, Z. Effect of mesoscale crystalline structure on the field-effect mobility of regioregular poly(3-hexyl thiophene) in thin-film transistors. *Adv. Funct. Mater.* **2005**, *15*, 671–676.
- [64] Sirringhaus, H.; Brown, P.; Friend, R.; Nielsen, M.; Bechgaard, K.; Langeveld-Voss, B.; Spiering, A.; Janssen, R.; Meijer, E.; Herwig, P. Two-dimensional charge transport in self-organized, high-mobility conjugated polymers. *Nature* **1999**, *401*, 685–688.
- [65] Yang, H.; Lefevre, S. W.; Ryu, C. Y.; Bao, Z. Solubility-driven thin film structures of regioregular poly(3-hexyl thiophene) using volatile solvents. *Appl. Phys. Lett.* **2007**, *90*, 172116.
- [66] Zen, A.; Pflaum, J.; Hirschmann, S.; Zhuang, W.; Jaiser, F.; Asawapirom, U.; Rabe, J. P.; Scherf, U.; Neher, D. Effect of molecular weight and annealing of poly(3-hexylthiophene)s on the performance of organic field-effect transistors. *Adv. Funct. Mater.* **2004**, *14*, 757–764.
- [67] Kline, R.; McGehee, M.; Kadnikova, E.; Liu, J.; Fréchet, J. Controlling the field-effect mobility of regioregular polythiophene by changing the molecular weight. *Adv. Mater.* **2003**, *15*, 1519–1522.
- [68] Kline, R.; McGehee, M.; Kadnikova, E.; Liu, J.; Frechet, J.; Toney, M. Dependence of regioregular poly(3-hexylthiophene) film morphology and field-effect mobility on molecular weight. *Macromolecules* **2005**, *38*, 3312–3319.
- [69] Brinkmann, M.; Chandezon, F.; Pansu, R.; Julien-Rabant, C. Epitaxial growth of highly oriented fibers of semiconducting polymers with a shish-kebab-like superstructure. *Adv. Funct. Mater.* **2009**, *19*, 2759–2766.
- [70] Müller, C.; Aghamohammadi . . . , M. One-step macroscopic alignment of conjugated polymer systems by epitaxial crystallization during spin-coating. *Adv. Funct. Mater.* **2013**,
- [71] Zhu, R.; Kumar, A.; Yang, Y. Polarizing organic photovoltaics. *Adv. Mater.* **2011**, *23*, 4193–4198.
- [72] These chemicals were synthesized by Dr. Michael Sommer, Department of Chemistry, University of Cambridge.
- [73] Lawrence, C. J. The mechanics of spin coating of polymer films. *Phys. of Fluids* **1988**, *31*, 2786–2795.

Bibliography

- [74] Jaczewska, J.; Raptis, I.; Budkowski, A.; Goustouridis, D.; Raczkowska, J.; Sanopoulou, A.; Pamula, E.; Bernasik, A.; Rysz, J. Swelling of poly(3-alkylthiophene) films exposed to solvent vapors and humidity: evaluation of solubility parameters. *Synt. Met.* **2007**, *157*, 726–732.
- [75] Hüttner, S.; Sommer, M.; Chiche, A.; Krausch, G.; Steiner, U.; Thelakkat, M. Controlled solvent vapour annealing for polymer electronics. *Soft Matter* **2009**, *5*, 4206–4211.
- [76] Bai, S.; Wu, Z.; Xu, X.; Jin, Y.; Sun, B.; Guo, X.; He, S.; Wang, X.; Ye, Z.; Wei, H.; Han, X.; Ma, W. Inverted organic solar cells based on aqueous processed ZnO interlayers at low temperature. *Appl. Phys. Lett.* **2012**, 203906.
- [77] Roe, R. J. *Methods of X-ray & neutron scattering in polymer science*; Oxford University Press, 2000.
- [78] <http://www.gisaxs.de/theory.html>.
- [79] Müller-Buschbaum, P. Grazing incidence small-angle X-ray scattering: an advanced scattering technique for the investigation of nanostructured polymer films. *Analytical and bioanalytical chemistry* **2003**, *376*, 3–10.
- [80] Lee, B.; Park, I.; Yoon, J.; Park, S.; Kim, J.; Kim, K.; Chang, T.; Ree, M. Structural analysis of block copolymer thin films with grazing incidence small-angle X-ray scattering. *Macromolecules* **2005**, *38*, 4311–4323.
- [81] Park, I.; Lee, B.; Ryu, J.; Im, K.; Yoon, J.; Ree, M.; Chang, T. Epitaxial phase transition of polystyrene-*b*-polyisoprene from hexagonally perforated layer to gyroid phase in thin film. *Macromolecules* **2005**, *38*, 10532–10536.
- [82] Asada, M.; Jiang, N.; Sendogdular, L.; Gin, P.; Wang, Y.; Endoh, M.; Koga, T.; Fukuto, M.; Schultz, D.; Lee, M. Heterogeneous lamellar structures near the polymer/substrate interface. *Macromolecules* **2012**, *45*, 7098–7106.
- [83] Daillant, J.; Gibaud, A. *X-ray and Neutron Reflectivity: Principles and Applications*; Springer, 2009.
- [84] Hoppe, H.; Sariciftci, N. Organic solar cells: An overview. *J. Mater. Res.* **2004**, *19*, 1924–1945.
- [85] Collins, B. A.; Gann, E.; Guignard, L.; He, X.; McNeill, C. R.; Ade, H. Molecular miscibility of polymer-fullerene blends. *J. Phys. Chem. Lett.* **2010**, *1*, 3160–3166.
- [86] Verploegen, E.; Mondal, R.; Bettinger, C. J.; Sok, S.; Toney, M. F.; Bao, Z. Effects of thermal annealing upon the morphology of polymer-fullerene blends. *Adv. Funct. Mater.* **2010**, *20*, 3519–3529.
- [87] Chiu, M.-Y.; Jeng, U.-S.; Su, M.-S.; Wei, K.-H. Morphologies of self-organizing regioregular conjugated polymer/fullerene aggregates in thin film solar cells. *Macromolecules* **2010**, *43*, 428–432.
- [88] Kiel, J.; Eberle, A.; Mackay, M. Nanoparticle agglomeration in polymer-based solar cells. *Phys. Rev. Lett.* **2010**, *105*, 168701.

Bibliography

- [89] Ruderer, M.; Meier, R.; Porcar, L.; Cubitt, R.; Müller-Buschbaum, P. Phase separation and molecular intermixing in polymer-fullerene bulk heterojunction thin films. *J. Phys. Chem. Lett.* **2012**, *3*, 683–688.
- [90] Chen, H.; Hegde, R.; Browning, J.; Dadmun, M. D. The miscibility and depth profile of PCBM in P3HT: thermodynamic information to improve organic photovoltaics. *Phys. Chem. Chem. Phys.* **2012**,
- [91] Chen, D.; Nakahara, A.; Wei, D.; Nordlund, D.; Russell, T. P. P3HT/PCBM bulk heterojunction organic photovoltaics: correlating efficiency and morphology. *Nano Lett.* **2011**, *11*, 561–567.
- [92] Vaynzof, Y.; Kabra, D.; Zhao, L.; Chua, L. L.; Steiner, U.; Friend, R. H. Surface-directed spinodal decomposition in poly[3-hexylthiophene] and C-61-butyric acid methyl ester blends. *ACS Nano* **2011**, *5*, 329–336.
- [93] Yang, X.; Loos, J.; Veenstra, S.; Verhees, W.; Wienk, M.; Kroon, J.; Michels, M.; Janssen, R. Nanoscale morphology of high-performance polymer solar cells. *Nano Lett.* **2005**, *5*, 579–583.
- [94] Treat, N. D.; Brady, M. A.; Smith, G.; Toney, M. F.; Kramer, E. J.; Hawker, C. J.; Chabynyc, M. L. Interdiffusion of PCBM and P3HT reveals miscibility in a photovoltaically active blend. *Adv. Energy Mater.* **2011**, *1*, 145–145.
- [95] Ro, H.; Akgun, B.; O'Connor, B.; Hammond, M.; Kline, R. J.; Snyder, C. R.; Satija, S. K.; Ayzner, A. L.; Toney, M. F.; Soles, C. L.; DeLongchamp, D. M. Poly (3-hexylthiophene) and [6, 6]-phenyl-C61-butyric acid methyl ester mixing in organic solar cells. *Macromolecules* **2012**, *45*, 6587–6599.
- [96] He, X.; Collins, B.; Watts, B.; Ade, H.; McNeill, C. Studying polymer/fullerene intermixing and miscibility in laterally patterned films with X-ray spectromicroscopy. *Small* **2012**, *8*, 1920–1927.
- [97] Nagarjuna, G.; Venkataraman, D. Strategies for controlling the active layer morphologies in OPVs. *J. Polym. Sci. B Polym. Phys.* **2012**, *50*, 1045–1056.
- [98] Ruderer, M. A.; Guo, S.; Meier, R.; Chiang, H. Y.; Körstgens, V.; Wiedersich, J.; Perlich, J.; Roth, S. V.; Müller-Buschbaum, P. Solvent-induced morphology in polymer-based systems for organic photovoltaics. *Adv. Funct. Mater.* **2011**, *21*, 3382–3391.
- [99] Shin, M.; Kim, H.; Park, J.; Nam, S.; Heo, K.; Ree, M.; Ha, C.-S.; Kim, Y. Abrupt morphology change upon thermal annealing in poly(3-Hexylthiophene)/soluble fullerene blend films for polymer solar cells. *Adv. Funct. Mater.* **2010**, *20*, 748–754.
- [100] Miller, S.; Fanchini, G.; Lin, Y.-Y.; Li, C.; Chen, C.-W.; Su, W.-F.; Chhowalla, M. Investigation of nanoscale morphological changes in organic photovoltaics during solvent vapor annealing. *J. Mater. Chem.* **2008**, *18*, 306–312.
- [101] Kiel, J. W.; Kirby, B. J.; Majkrzak, C. F.; Maranvillec, B. B.; Mackay, M. E. Nanoparticle concentration profile in polymer-based solar cells. *Soft Matter* **2010**, *6*, 641–646.

Bibliography

- [102] Geens, W.; Martens, T.; Poortmans, J.; Aernouts, T.; Manca, J.; Lutsen, L.; Heremans, P.; Borghs, S.; Mertens, R.; Vanderzande, D. Modelling the short-circuit current of polymer bulk heterojunction solar cells. *Thin Solid Films* **2004**, *451*, 498–502.
- [103] Pascui, O.; Lohwasser, R.; Sommer, M.; Thelakkat, M.; Thurn-Albrecht, T.; Saalwächter, K. High crystallinity and nature of crystal-crystal phase transformations in regioregular poly (3-hexylthiophene). *Macromolecules* **2010**, *43*, 9401–9410.
- [104] Brady, M. A.; Su, G. M.; Chabynyc, M. L. Recent progress in the morphology of bulk heterojunction photovoltaics. *Soft Matter* **2011**, *7*, 11065.
- [105] Ballantyne, A. M. et al. Understanding the influence of morphology on poly 3-hexylselenothiophene): PCBM solar cells. *Macromolecules* **2010**, *43*, 1169–1174.
- [106] Brabec, C. J.; Gowrisanker, S.; Halls, J. J. M.; Laird, D.; Jia, S.; Williams, S. P. Polymer-fullerene bulk-heterojunction solar cells. *Adv. Mater.* **2010**, *22*, 3839–3856.
- [107] Mokarian-Tabari, P.; Geoghegan, M.; Howse, J. R.; Heriot, S. Y.; Thompson, R. L.; Jones, R. A. L. Quantitative evaluation of evaporation rate during spin-coating of polymer blend films: Control of film structure through defined-atmosphere solvent-casting. *Eur. Phys. J. E: Soft Matter Biol. Phys.* **2010**, *33*, 283–289.
- [108] Jaczewska, J.; Budkowski, A.; Bernasik, A.; Moons, E.; Rysz, J. Polymer vs solvent diagram of film structures formed in spin-cast poly (3-alkylthiophene) blends. *Macromolecules* **2008**, *41*, 4802–4810.
- [109] Liu, J.; Shao, S.; Wang, H.; Zhao, K.; Xue, L.; Gao, X.; Xie, Z.; Han, Y. The mechanisms for introduction of n-dodecylthiol to modify the P3HT/PCBM morphology. *Org. Electron.* **2010**, *11*, 775–783.
- [110] Salim, T.; Wong, L.; Bräuer, B.; Kukreja, R.; Foo, Y.; Bao, Z.; Lam, Y. Solvent additives and their effects on blend morphologies of bulk heterojunctions. *J. Mater. Chem.* **2010**, *21*, 242–250.
- [111] Tsai, J. H.; Lai, Y. C.; Higashihara, T.; Lin, C. J.; Ueda, M.; Chen, W. C. Enhancement of P3HT/PCBM photovoltaic efficiency using the surfactant of triblock copolymer containing poly(3-hexylthiophene) and poly(4-vinyltriphenylamine) segments. *Macromolecules* **2010**, *43*, 6085–6091.
- [112] Tai, Q.; Li, J.; Liu, Z.; Sun, Z.; Zhao, X.; Yan, F. Enhanced photovoltaic performance of polymer solar cells by adding fullerene end-capped polyethylene glycol. *J. Mater. Chem.* **2011**, *21*, 6848–6853.
- [113] Moon, J. S.; Takacs, C. J.; Cho, S.; Coffin, R. C.; Kim, H.; Bazan, G. C.; Heeger, A. J. Effect of processing additive on the nanomorphology of a bulk heterojunction material. *Nano Lett.* **2010**, *10*, 4005–4008.
- [114] Moulé, A. J.; Meerholz, K. Controlling morphology in polymer-fullerene mixtures. *Adv. Mater.* **2008**, *20*, 240–245.
- [115] Jo, J.; Kim, S.-S.; Na, S.-I.; Yu, B.-K.; Kim, D.-Y. Time-dependent morphology evolution by annealing processes on polymer:fullerene blend solar cells. *Adv. Funct. Mater.* **2009**, *19*, 866–874.

Bibliography

- [116] Bavel, S. S. V.; Bärenklau, M.; With, G. D.; Hoppe, H.; Loos, J. P3HT/PCBM bulk heterojunction solar cells: impact of blend composition and 3D morphology on device performance. *Adv. Funct. Mater.* **2010**, *20*, 1458–1463.
- [117] Zhao, Y.; Xie, Z.; Qu, Y.; Geng, Y.; Wang, L. Solvent-vapor treatment induced performance enhancement of poly(3-hexylthiophene):methanofullerene bulk-heterojunction photovoltaic cells. *Appl. Phys. Lett.* **2007**, *90*, 043504.
- [118] Brabec, C. J.; Heeney, M.; McCulloch, I.; Nelson, J. Influence of blend microstructure on bulk heterojunction organic photovoltaic performance. *Chem. Soc. Rev.* **2011**, *40*, 1185–1199.
- [119] Jimison, L. H.; Toney, M. F.; McCulloch, I.; Heeney, M.; Salleo, A. Charge-transport anisotropy due to grain boundaries in directionally crystallized thin films of regioregular poly(3-hexylthiophene). *Adv. Mater.* **2009**, *21*, 1568–1572.
- [120] Lan, Y.; Huang, C. Charge mobility and transport behavior in the ordered and disordered states of the regioregular poly(3-hexylthiophene). *J. Phys. Chem. B* **2009**, *113*, 14555–14564.
- [121] Kim, J.-H.; Park, J. H.; Lee, J. H.; Kim, J. S.; Sim, M.; Shim, C.; Cho, K. Bulk heterojunction solar cells based on preformed polythiophene nanowires via solubility-induced crystallization. *J. Mater. Chem.* **2010**, *20*, 7398–7405.
- [122] Brinkmann, M.; Contal, C.; Kayunkid, N.; Djuric, T.; Resel, R. Highly oriented and nanotextured films of regioregular poly(3-hexylthiophene) grown by epitaxy on the nanostructured surface of an aromatic substrate. *Macromolecules* **2010**, *43*, 7604–7610.
- [123] O’connor, B.; Kline, R. J.; Conrad, B. R.; Richter, L. J.; Gundlach, D.; Toney, M. F.; Delongchamp, D. M. Anisotropic structure and charge transport in highly strain-aligned regioregular poly(3-hexylthiophene). *Adv. Funct. Mater.* **2011**, *21*, 3697–3705.
- [124] Vohra, V.; Arrighetti, G.; Barba, L.; Higashimine, K.; Porzio, W.; Murata, H. Enhanced vertical concentration gradient in rubbed P3HT:PCBM graded bilayer solar cells. *J. Phys. Chem. Lett.* **2012**, *3*, 1820–1823.
- [125] Crossland, E. J. W.; Tremel, K.; Fischer, F.; Rahimi, K.; Reiter, G.; Steiner, U.; Ludwigs, S. Anisotropic charge transport in spherulitic poly(3-hexylthiophene) films. *Adv. Mater.* **2012**, *24*, 839–844.
- [126] Crossland, E. J. W.; Rahimi, K.; Reiter, G.; Steiner, U.; Ludwigs, S. Systematic control of nucleation density in poly(3-hexylthiophene) thin films. *Adv. Funct. Mater.* **2010**, *21*, 518–524.
- [127] Kohn, P.; Huettner, S.; Steiner, U.; Sommer, M. Fractionated crystallization of defect-free poly(3-hexylthiophene). *ACS Macro Letters* **2012**, *1*, 1170–1175.
- [128] Liu, X. Solvent interaction and morphology of organic blend photovoltaics. M.Sc. thesis, University of Cambridge, 2006.

Bibliography

- [129] Junkar, I.; Cvelbar, U.; Vesel, A.; Hauptman, N.; Mozetič, M. The role of crystallinity on polymer interaction with oxygen plasma. *Plasma Process. Polym.* **2009**, *6*, 667–675.
- [130] Chen, S.; Manders, J. R.; Tsang, S. W.; So, F. Metal oxides for interface engineering in polymer solar cells. *J. Mater. Chem.* **2012**, 1–11.
- [131] Wu, W.-R.; Jeng, U.-S.; Su, C.-J.; Wei, K.-H.; Su, M.-S.; Chiu, M.-Y.; Chen, C.-Y.; Su, W.-B.; Su, C.-H.; Su, A.-C. Competition between fullerene aggregation and poly(3-hexylthiophene) crystallization upon annealing of bulk heterojunction solar cells. *ACS Nano* **2011**, *5*, 6233–6243.
- [132] McNeill, C.; Greenham, N. Conjugated-polymer blends for optoelectronics. *Adv. Mater.* **2009**, *21*, 3840–3850.
- [133] Kroon, R.; Lenes, M.; Hummelen, J. C.; Blom, P. W. M.; Boer, B. D. Small bandgap polymers for organic solar cells (polymer material development in the last 5 years). *Polymer Reviews* **2008**, *48*, 531–582.
- [134] <http://www.polyera.com/>.
- [135] Mcneill, C. R.; Watts, B.; Thomsen, L.; Belcher, W. J.; Greenham, N. C.; Dastoor, P. C.; Ade, H. Evolution of laterally phase-separated polyfluorene blend morphology studied by X-ray spectromicroscopy. *Macromolecules* **2009**, *42*, 3347–3352.
- [136] Kim, J.; Ho, P.; Murphy, C.; Friend, R. Phase separation in polyfluorene-based conjugated polymer blends: lateral and vertical analysis of blend spin-cast thin films. *Macromolecules* **2004**, *37*, 2861–2871.
- [137] Kietzke, T.; Hörhold, H.-H.; Neher, D. Efficient polymer solar cells based on M3EH-PPV. *Chem. Mater.* **2005**, *17*, 6532–6537.
- [138] Veenstra, S. C.; Loos, J.; Kroon, J. M. Nanoscale structure of solar cells based on pure conjugated polymer blends. *Prog. Photovolt: Res. Appl.* **2007**, *15*, 727–740.
- [139] Arias, A.; MacKenzie, J.; Stevenson, R.; Halls, J.; Inbasekaran, M.; Woo, E.; Richards, D.; Friend, R. Photovoltaic performance and morphology of polyfluorene blends: a combined microscopic and photovoltaic investigation. *Macromolecules* **2001**, *34*, 6005–6013.
- [140] Liu, X.; Huettner, S.; Rong, Z.; Sommer, M.; Friend, R. H. Solvent additive control of morphology and crystallization in semiconducting polymer blends. *Adv. Mater.* **2011**, *24*, 669–674.
- [141] Moore, J. R.; Albert-Seifried, S.; Rao, A.; Massip, S.; Watts, B.; Morgan, D. J.; Friend, R. H.; Mcneill, C. R.; Sirringhaus, H. Polymer blend solar cells based on a high-mobility naphthalenediimide-based polymer acceptor: device physics, photophysics and morphology. *Adv. Energy Mater.* **2011**, *1*, 230–240.
- [142] Mori, D.; Benten, H.; Kosaka, J.; Ohkita, H.; Ito, S.; Miyake, K. Polymer/polymer blend solar cells with 2.0% efficiency developed by thermal purification of nanoscale phase-separated morphology. *ACS Appl. Mater. Interfaces* **2011**, *3*, 2924–2927.

Bibliography

- [143] Kim, Y.; Cook, S.; Choulis, S.; Nelson, J.; Durrant, J.; Bradley, D. Organic photovoltaic devices based on blends of regioregular poly (3-hexylthiophene) and poly (9, 9-dioctylfluorene-co-benzothiadiazole). *Chem. Mater.* **2004**, *16*, 4812–4818.
- [144] McNeill, C.; Westenhoff, S.; Groves, C.; Friend, R.; Greenham, N. Influence of nanoscale phase separation on the charge generation dynamics and photovoltaic performance of conjugated polymer blends: Balancing charge generation and separation. *J. Phys. Chem. C* **2007**, *111*, 19153–19160.
- [145] McNeill, C.; Halls, J.; Wilson, R.; Whiting, G.; Berkebile, S.; Ramsey, M.; Friend, R.; Greenham, N. Efficient polythiophene/polyfluorene copolymer bulk heterojunction photovoltaic devices: device physics and annealing effects. *Adv. Funct. Mater.* **2008**, *18*, 2309–2321.
- [146] Yan, H.; Collins, B.; Gann, E.; Wang, C.; Ade, H.; McNeill, C. Correlating the efficiency and nanomorphology of polymer blend solar cells utilizing resonant soft X-ray scattering. *ACS Nano* **2012**, *6*, 677–688.
- [147] Data provided by Cambridge Display Technology.
- [148] Vaynzof, Y.; Brenner, T.; Kabra, D.; Sirringhaus, H.; Friend, R. Compositional and morphological studies of polythiophene/polyfluorene blends in inverted architecture hybrid solar cells. *Adv. Funct. Mater.* **2012**, *22*, 2418–2424.
- [149] Tsoi, W. C.; Spencer, S. J.; Yang, L.; Ballantyne, A. M.; Nicholson, P. G.; Turnbull, A.; Shard, A. G.; Murphy, C. E.; Bradley, D. D. C.; Nelson, J.; Kim, J. S. Effect of crystallization on the electronic energy levels and thin film morphology of P3HT:PCBM blends. *Macromolecules* **2011**, *44*, 2944–2952.
- [150] Arias, A.; Endicott, F.; Street, R. Surface-induced self-encapsulation of polymer thin-film transistors. *Adv. Mater.* **2006**, *18*, 2900–2904.
- [151] Babel, A.; Jenekhe, S. Morphology and field-effect mobility of charge carriers in binary blends of poly (3-hexylthiophene) with poly [2-methoxy-5-(2-ethylhexoxy)-1, 4-phenylenevinylene] and polystyrene. *Macromolecules* **2004**, *37*, 9835–9840.
- [152] Ferenczi, T. A. M.; Müller, C.; Bradley, D. D. C.; Smith, P.; Nelson, J.; Stingelin, N. Organic semiconductor: insulator polymer ternary blends for photovoltaics. *Adv. Mater.* **2011**, *23*, 4093–4097.
- [153] Müller, C.; Goffri, S.; and, D. B. Tough, semiconducting polyethylene-poly(3-hexylthiophene) diblock copolymers. *Adv. Funct. Mater.* **2007**, *17*, 2674–2679.
- [154] Chua, L. L.; Ho, P. K.; Sirringhaus, H.; Friend, R. H. Observation of field-effect transistor behavior at self-organized interfaces. *Adv. Mater.* **2004**, *16*, 1609–1615.
- [155] Salleo, A.; Arias, A. Solution based self-assembly of an array of polymeric thin-film transistors. *Adv. Mater.* **2007**, *19*, 3540–3543.

Bibliography

- [156] Qiu, L.; Lim, J. A.; Wang, X.; Lee, W. H.; Hwang, M.; Cho, K. Versatile use of vertical-phase-separation-induced bilayer structures in organic thin-film transistors. *Adv. Mater.* **2008**, *20*, 1141–1145.
- [157] Lu, G.; Tang, H.; Qu, Y.; Li, L.; Yang, X. Enhanced electrical conductivity of highly crystalline polythiophene/insulating-polymer composite. *Macromolecules* **2007**, *40*, 6579–6584.
- [158] Lu, G.; Tang, H.; Huan, Y.; Li, S.; Li, L.; Wang, Y.; Yang, X. Enhanced charge transportation in semiconducting polymer/insulating polymer composites: the role of an interpenetrating bulk interface. *Adv. Funct. Mater.* **2010**, *20*, 1714–1720.
- [159] Kumar, A.; Baklar, M. A.; Scott, K.; Kreouzis, T.; Stingelin-Stutzmann, N. Efficient, stable bulk charge transport in crystalline/crystalline semiconductor-insulator blends. *Adv. Mater.* **2009**, *21*, 4447–4451.
- [160] Nilsson, S.; Bernasik, A.; Budkowski, A.; Moons, E. Morphology and phase segregation of spin-casted films of polyfluorene/PCBM blends. *Macromolecules* **2007**, *40*, 8291–8301.
- [161] Goffri, S.; Müller, C.; Stingelin-Stutzmann, N.; Breiby, D. W.; Radano, C. P.; Andreasen, J. W.; Thompson, R.; Janssen, R. A. J.; Nielsen, M. M.; Smith, P.; Sirringhaus, H. Multicomponent semiconducting polymer systems with low crystallization-induced percolation threshold. *Nat. Mater.* **2006**, *5*, 950–956.
- [162] Qiu, L.; Lee, W. H.; Wang, X.; Kim, J. S.; Lim, J. A.; Kwak, D.; Lee, S.; Cho, K. Organic thin-film transistors based on polythiophene nanowires embedded in insulating polymer. *Adv. Mater.* **2009**, *21*, 1349–1353.
- [163] Qiu, L.; Wang, X.; Lee, W. H.; Lim, J. A.; Kim, J. S.; Kwak, D.; Cho, K. Organic thin-film transistors based on blends of poly(3-hexylthiophene) and polystyrene with a solubility-induced low percolation threshold. *Chem. Mater.* **2009**, *21*, 4380–4386.
- [164] Berson, S.; Bettignies, R. D.; Bailly, S.; Guillerez, S. Poly(3-hexylthiophene) fibers for photovoltaic applications. *Adv. Funct. Mater.* **2007**, *17*, 1377–1384.
- [165] Kim, J. S.; Lee, J. H.; Park, J. H.; Shim, C.; Sim, M.; Cho, K. High-efficiency organic solar cells based on preformed poly(3-hexylthiophene) nanowires. *Adv. Funct. Mater.* **2010**, *21*, 480–486.
- [166] Kim, B. G.; Kim, M. S.; Kim, J. Ultrasonic-assisted nanodimensional self-assembly of poly-3-hexylthiophene for organic photovoltaic cells. *ACS Nano* **2010**, *4*, 2160–2166.
- [167] Park, Y. D.; Lee, H. S.; Choi, Y. J.; Kwak, D.; Cho, J. H.; Lee, S.; Cho, K. Solubility-induced ordered polythiophene precursors for high-performance organic thin-film transistors. *Adv. Funct. Mater.* **2009**, *19*, 1200–1206.
- [168] Autumn, K.; Gravish, N. Gecko adhesion: evolutionary nanotechnology. *Philos. Trans. Roy. Soc. London Ser. A* **2008**, *366*, 1575–1590.
- [169] Bhushan, B.; Sayer, R. *Applied scanning probe methods VII-Biomimetics and industrial applications*; Springer, Germany, 2007.

Bibliography

- [170] Nosonovsky, M.; Bhushan, B. Multiscale effects and capillary interactions in functional biomimetic surfaces for energy conversion and green engineering. *Philos. Trans. Roy. Soc. London Ser. A* **2009**, *367*, 1511–1539.
- [171] Peattie, A.; Majidi, C.; Corder, A. Ancestrally high elastic modulus of gecko setal beta-keratin. *J. R. Soc. Interface* **2007**, *4*, 1071–1076.
- [172] Autumn, K. Effective elastic modulus of isolated gecko setal arrays. *J. Exp. Biol.* **2006**, *209*, 3558–3568.
- [173] Gao, H.; Wang, X.; Yao, H.; Gorb, S.; Arzt, E. Mechanics of hierarchical adhesion structures of geckos. *Mech. Mater.* **2005**, *37*, 275–285.
- [174] Autumn, K.; Liang, Y.; Hsieh, S.; Zesch, W.; Chan, W.; Kenny, T.; Fearing, R.; Full, R. Adhesive force of a single gecko foot-hair. *Nature* **2000**, *405*, 681–684.
- [175] Autumn, K.; Sitti, M.; Liang, Y.; Peattie, A.; Hansen, W.; Sponberg, S.; Kenny, T.; Fearing, R.; Israelachvili, J.; Full, R. Evidence for van der Waals adhesion in gecko setae. *Proc. Natl. Acad. Sci. USA* **2002**, *99*, 12252–12256.
- [176] Kim, T.; Bhushan, B. The adhesion model considering capillarity for gecko attachment system. *J. R. Soc. Interface* **2008**, *5*, 319–327.
- [177] Huber, G.; Mantz, H.; Spolenak, R.; Mecke, K.; Jacobs, K.; Gorb, S.; Arzt, E. Evidence for capillarity contributions to gecko adhesion from single spatula nanomechanical measurements. *Proc. Natl. Acad. Sci. USA* **2005**, *102*, 16293–16296.
- [178] Puthoff, J. B.; Prowse, M. S.; Wilkinson, M.; Autumn, K. Changes in materials properties explain the effects of humidity on gecko adhesion. *J. Exp. Biol.* **2010**, *213*, 3699–3704.
- [179] Autumn, K.; Dittmore, A.; Santos, D.; Spenko, M.; Cutkosky, M. Frictional adhesion: a new angle on gecko attachment. *J. Exp. Biol.* **2006**, *209*, 3569–3579.
- [180] Tian, Y.; Pesika, N.; Zeng, H.; Rosenberg, K.; Zhao, B.; McGuiggan, P.; Autumn, K.; Israelachvili, J. Adhesion and friction in gecko toe attachment and detachment. *Proc. Natl. Acad. Sci. USA* **2006**, *103*, 19320–19325.
- [181] Gravish, N.; Wilkinson, M.; Sponberg, S.; Parness, A.; Esparza, N.; Soto, D.; Yamaguchi, T.; Broide, M.; Cutkosky, M.; Creton, C. Rate-dependent frictional adhesion in natural and synthetic gecko setae. *J. R. Soc. Interface* **2010**, *7*, 259–269.
- [182] Hansen, W.; Autumn, K. Evidence for self-cleaning in gecko setae. *Proc. Natl. Acad. Sci. USA* **2005**, *102*, 385–389.
- [183] Vajpayee, S.; Long, R.; Shen, L.; Jagota, A.; Hui, C. Effect of rate on adhesion and static friction of a film-terminated fibrillar interface. *Langmuir* **2009**, *25*, 2765–2771.

Bibliography

- [184] Jagota, A.; Bennison, S. Mechanics of adhesion through a fibrillar microstructure. *Integr. Comp. Biol.* **2002**, *42*, 1140–1145.
- [185] Persson, B. N. J. On the mechanism of adhesion in biological systems. *J. Chem. Phys.* **2003**, *118*, 7614–7621.
- [186] Gao, H.; Yao, H. Shape insensitive optimal adhesion of nanoscale fibrillar structures. *Proc. Natl. Acad. Sci. USA* **2004**, *101*, 7851–7856.
- [187] Johnson, K.; Kendall, K.; Roberts, A. Surface energy and the contact of elastic solids. *Proc. R. Soc. A* **1971**, *324*, 301–313.
- [188] Arzt, E.; Gorb, S.; Spolenak, R. From micro to nano contacts in biological attachment devices. *Proc. Natl. Acad. Sci. USA* **2003**, *100*, 10603–10606.
- [189] Jeong, H.; Suh, K. Nanohairs and nanotubes: efficient structural elements for gecko-inspired artificial dry adhesives. *Nano Today* **2009**, *4*, 335–346.
- [190] Sitti, M.; Fearing, R. Synthetic gecko foot-hair micro/nano-structures as dry adhesives. *J. Adhes. Sci. Technol.* **2003**, *17*, 1055–1073.
- [191] Greiner, C.; Spolenak, R.; Arzt, E. Adhesion design maps for fibrillar adhesives: the effect of shape. *Acta Biomater.* **2009**, *5*, 597–606.
- [192] del Campo, A.; Greiner, C.; Arzt, E. Contact shape controls adhesion of bioinspired fibrillar surfaces. *Langmuir* **2007**, *23*, 10235–10243.
- [193] Murphy, M. P.; Kim, S.; Sitti, M. Enhanced adhesion by gecko-inspired hierarchical fibrillar adhesives. *ACS Appl. Mater. Interfaces* **2009**, *1*, 849–855.
- [194] Campo, A. D.; Arzt, E. Design parameters and current fabrication approaches for developing bioinspired dry adhesives. *Macromol. Biosci.* **2007**, *7*, 118–127.
- [195] Gorb, S.; Varenberg, M.; Peressadko, A.; Tuma, J. Biomimetic mushroom-shaped fibrillar adhesive microstructure. *J. R. Soc. Interface* **2007**, *4*, 271–275.
- [196] Murphy, M. P.; Aksak, B.; Sitti, M. Gecko-inspired directional and controllable adhesion. *Small* **2008**, *5*, 170–175.
- [197] Geim, A. K.; Dubonos, S. V.; Grigorieva, I. V.; Novoselov, K. S.; Zhukov, A. A.; Shapoval, S. Y. Microfabricated adhesive mimicking gecko foot-hair. *Nature Mater.* **2003**, *2*, 461–463.
- [198] Majidi, C.; Groff, R.; Maeno, Y.; Schubert, B.; Baek, S.; Bush, B.; Maboudian, R.; Gravish, N.; Wilkinson, M.; Autumn, K.; Fearing, R. High friction from a stiff polymer using microfiber arrays. *Phys. Rev. Lett.* **2006**, *97*, 076103.

Bibliography

- [199] Ho, A.; Yeo, L.; Lam, Y.; Rodríguez, I. Fabrication and analysis of gecko-inspired hierarchical polymer nanosetae. *ACS Nano* **2011**, *5*, 1897–1906.
- [200] Jeong, H.; Lee, J.; Kim, H.; Moon, S.; Suh, K. A nontransferring dry adhesive with hierarchical polymer nanohairs. *Proc. Natl. Acad. Sci. USA* **2009**, *106*, 5639–5644.
- [201] Qu, L.; Dai, L. Gecko-foot-mimetic aligned single-walled carbon nanotube dry adhesives with unique electrical and thermal properties. *Adv. Mater.* **2007**, *19*, 3844–3849.
- [202] Wirth, C.; Hofmann, S.; Robertson, J. Surface properties of vertically aligned carbon nanotube arrays. *Diamond Relat. Mater.* **2008**, *17*, 1518–1524.
- [203] Qu, L.; Dai, L.; Stone, M.; Xia, Z.; Wang, Z. Carbon nanotube arrays with strong shear binding-on and easy normal lifting-off. *Science* **2008**, *322*, 238–242.
- [204] Zhao, Y.; Tong, T.; Delzeit, L.; Kashani, A.; Meyyappan, M.; Majumdar, A. Interfacial energy and strength of multiwalled-carbon-nanotube-based dry adhesive. *J. Vac. Sci. Technol. B* **2006**, *24*, 331–335.
- [205] Sameoto, D.; Menon, C. Recent advances in the fabrication and adhesion testing of biomimetic dry adhesives. *Smart Mater. Struct.* **2010**, *19*, 103001.
- [206] Ge, L.; Sethi, S.; Ci, L.; Ajayan, P.; Dhinojwala, A. Carbon nanotube-based synthetic gecko tapes. *Proc. Natl. Acad. Sci. USA* **2007**, *104*, 10792–10795.
- [207] Dirks, J.-H.; Clemente, C. J.; Federle, W. Insect tricks: two-phasic foot pad secretion prevents slipping. *J. R. Soc. Interface* **2010**, *7*, 587–593.
- [208] Lee, J.; Majidi, C.; Schubert, B.; Fearing, R. Sliding-induced adhesion of stiff polymer microfibre arrays. I. Macroscale behaviour. *J. R. Soc. Interface* **2008**, *5*, 835–844.
- [209] Bartlett, M.; Croll, A.; King, D.; Paret, B.; Irschick, D.; Crosby, A. Looking beyond fibrillar features to scale gecko-like adhesion. *Adv. Mater.* **2012**, *24*, 1078–1083.
- [210] Greiner, C.; del Campo, A.; Arzt, E. Adhesion of bioinspired micropatterned surfaces: Effects of pillar radius, aspect ratio, and preload. *Langmuir* **2007**, *23*, 3495–3502.
- [211] Aksak, B.; Murphy, M.; Sitti, M. Gecko inspired micro-fibrillar adhesives for wall climbing robots on micro/nanoscale rough surfaces. *IEEE Int. Conf. on Robotics and Automation, Pasadena, CA, USA, May 19-23, 2008*.
- [212] Pugno, N.; Lepore, E. Observation of optimal gecko's adhesion on nanorough surfaces. *Biosystems* **2008**, *94*, 218–222.
- [213] Yu, J.; Chary, S.; Das, S.; Tamelier, J.; Turner, K.; Israelachvili, J. The friction and adhesion of gecko-inspired PDMS flaps on rough surfaces. *Langmuir* **2012**, *28*, 11527–11534.

Bibliography

- [214] Huber, G.; Gorb, S.; Hosoda, N.; Spolenak, R.; Arzt, E. Influence of surface roughness on gecko adhesion. *Acta Biomater.* **2007**, *3*, 607–610.